Aus der Klinik und Poliklinik für Radiologie
Klinikum der Ludwig-Maximilians-Universität München
Direktor: Prof. Dr. med. Jens Ricke

Incoherent-Flow-Induced Signal Decay in Diffusion-Weighted Magnetic Resonance Imaging

Dissertation
zum Erwerb des Doktorgrades der Naturwissenschaften
an der Medizinischen Fakultät
der Ludwig-Maximilians-Universität München

vorgelegt von
Moritz Jörg Schneider
aus Schaffhausen
2018

Gedruckt mit Genehmigung der Medizinischen Fakultät

der Ludwig-Maximilians-Universität München

Betreuer:

Prof. Dr. rer. nat. Olaf Dietrich

Zweitgutachter:

Prof. Dr. Gunnar Brix

Dekan:

Prof. Dr. med. dent. Reinhard Hickel

Tag der mündlichen Prüfung: 26.06.2019

Publications: Articles & Book Chapter

During the course of this thesis, the following articles and book chapter have been published:

1. **IVIM MRI in the Kidney**. Chapter in book: Intravoxel Incoherent Motion (IVIM) MRI – Principles and Applications. 2018. *Pan Stanford Publishing Pte. Ltd.* **Schneider MJ**, Notohamiprodjo N, Dietrich O.

2. **Diffusion-weighted magnetic resonance imaging to assess diffuse renal pathology: a systematic review and statement paper.** August 2018. *Nephrology Dialysis Transplantation* (IF 4.085). Caroli A, **Schneider MJ,** Friedli I, Ljimani A, De Seigneux S, Boor P, Gullapudi L, Kazmi I, Mendichovszky IA, Notohamiprodjo M, Selby NM, Thoeny HC, Grenier N, Vallée JP

3. **Quantitative Dynamic Contrast-Enhanced MRI of a 3-Dimensional Artificial Capillary Network.** April 2017. *Medical Physics* (IF 2.617). Gaass T, **Schneider MJ,** Ingrisch M, Dietrich O, Dinkel J.

4. **Prognostische Information aus präoperativen MR-Daten von Patienten mit Glioblastomen: eine Radiomics-Studie.** März 2017. *RöFo - Fortschritte auf dem Gebiet der Röntgenstrahlen und der bildgebenden Verfahren* (IF 1.554). Ingrisch M, **Schneider MJ**, Nörenberg D, Figueiredo GN, Maier-Hein K, Suchorska B, Reiser MF, Tonn JC, Ertl-Wagner B.

5. **Radiomic Analysis Reveals Prognostic Information in T1-Weighted Baseline Magnetic Resonance Imaging in Patients With Glioblastoma.** January 2017. *Investigative Radiology* (IF 6.224). Ingrisch M, **Schneider MJ**, Nörenberg D, Figueiredo GN, Maier-Hein K, Suchorska B, Schüller U, Albert N, Brückmann H, Reiser MF, Tonn JC, Ertl-Wagner B.

6. **Contrast-Enhanced Ultrasound with VEGFR2-Targeted Microbubbles for Monitoring Regorafenib Therapy Effects in Experimental Colorectal Adenocarcinomas in Rats with DCE-MRI and Immunohistochemical Validation.** January 2017. *PLoS ONE* (IF 2.766). Eschbach RS, Clevert DA, Hirner-Eppeneder H, Ingrisch M, Moser M, Schuster J, Tadros D, **Schneider MJ**, Kazmierczak PM, Reiser MF, Cyran CC.

7. **A Pilot Trial of Doxorubicin Containing Phosphatidyldiglycerol Based Thermosensitive Liposomes in Spontaneous Feline Soft Tissue Sarcoma.** September 2016. *International Journal of Hyperthermia* (IF 3.44). Zimmermann K, Hossann M, Hirschberger J, Troedson K, Peller M, **Schneider MJ**, Brühschwein A, Meyer-Lindenberg A, Wess G, Wergin M, Dörfelt R, Knösel T, Schwaiger M, Baumgartner C, Lindner LH.

8. **Dynamic Contrast-Enhanced MRI Suggests Normal Perfusion in Normal Appearing White Matter in Multiple Sclerosis.** August 2016. *Investigative Radiology* (IF 6.224). Ingrisch M, **Schneider MJ**, Hohlfeld R, Kümpfel T, Sourbron S, Herberich S, Reiser MF, Ertl-Wagner B.

9. **Intravoxel Incoherent Motion Magnetic Resonance Imaging in Partially Nephrectomized Kidneys.** May 2016. *Investigative Radiology* (IF 6.224). **Schneider MJ**, Dietrich O, Ingrisch M, Helck A, Winter KS, Reiser MF, Staehler M, Casuscelli J, Notohamiprodjo M.

10. **αvß3-Integrin-Targeted Magnetic Resonance Imaging for the Assessment of Early Antiangiogenic Therapy Effects in Orthotopic Breast Cancer Xenografts.** April 2016. *Investigative Radiology* (IF 6.224). Kazmierczak PM, **Schneider MJ**, Habereder T, Hirner-Eppeneder H, Eschbach RS, Moser M, Reiser FM, Lauber K, Nikolaou K, Cyran CC.

11. **Multiparametrischer CEUS mit VEGFR-2 spezifischen Microbubbles und DCE-MRT zum Monitoring der Effekte von Regorafenib auf Kolonkarzinom-Xenografts in Ratten mit immunhistochemischer Validierung.** March 2016. *RöFo - Fortschritte auf dem Gebiet der Röntgenstrahlen und der bildgebenden Verfahren* (IF 1.554). Eschbach RS, Clevert DA, Hirner-Eppeneder H, Kazmierczak PM, Reiser FM, Tadros D, **Schneider MJ**, Havla L, Schuster J, Moser M, Cyran CC.

12. **MRT mit αvß3-Integrin-spezifischen USPION zum Monitoring früher antiangiogenetischer Therapieeffekte im Orthotopen Mammakarzinom-Modell der Maus.** March 2016. *RöFo - Fortschritte auf dem Gebiet der Röntgenstrahlen und der bildgebenden Verfahren* (IF 1.554). Kazmierczak PM, **Schneider MJ**, Habereder T, Hirner-Eppeneder H, Eschbach RS, Moser M, Reiser FM, Cyran CC.

13. **Classification of Arterial and Venous Cerebral Vasculature Based on Wavelet Postprocessing of CT Perfusion Data.** February 2016. *Medical Physics* (IF 2.617). Havla L, **Schneider MJ**, Thierfelder KM, Beyer SE, Ertl-Wagner B, ReiserMF, Sommer WH, Dietrich O.

14. **Validation of a Method to Differentiate Arterial and Venous Vessels in CT Perfusion Data Using Linear Combinations of Quantitative Time-Density Curve Characteristics.** October 2015. *European Radiology* (IF 4.014). Havla L, **Schneider MJ**, Thierfelder KM, Beyer SE, Ertl-Wagner B, Sommer WH, Dietrich O.

15. **Pulmonary Perfusion Imaging: Qualitative Comparison of TCIR MRI and SPECT/CT in Porcine Lung.** September 2015. *European Journal of Radiology* (IF 2.843). Gaass T, Bauman G, Biederer J, Hintze C, **Schneider MJ**, Dinkel J.

16. **Correlation of Perfusion MRI and 18F-FDG PET Imaging Biomarkers for Monitoring Regorafenib Therapy in Experimental Colon Carcinomas with Immunohistochemical Validation.** Februray 2015. *PLoS ONE* (IF 2.766). Eschbach RS, Fendler WP, Kazmierczak PM, Hacker M, Rominger A, Carlsen J, Hirner-Eppeneder H, Schuster J, Moser M, Havla L, **Schneider MJ**, Ingrisch M, Spaeth L, Reiser MF, Nikolaou K, Cyran CC.

17. **Monitoring Early Response to Anti-Angiogenic Therapy: Diffusion-Weighted Magnetic Resonance Imaging and Volume Measurements in Colon Carcinoma Xenografts.** September 2014. *PLoS ONE* (IF 2.766). **Schneider MJ**, Cyran CC, Nikolaou K, Hirner-Eppeneder H., Reiser MF, Dietrich O.

Contents

1 Introduction

Magnetic resonance imaging (MRI) is a most important and versatile tool in today's medical diagnostics[1] providing tomographic images of the entire body. In contrast to X-ray computed tomography (CT) or positron emission tomography (PET), MRI does not expose the patients to ionizing radiation but utilizes the effect of nuclear magnetic resonance (NMR) instead. While MRI provides also excellent soft-tissue contrast, a major feature of MRI is imaging beyond morphology with the aim of gaining information about physiological processes and tissue function. The selection of available methods is vast and only a selected few shall be named here: a recent development, chemical exchange saturation transfer (CEST)[2], allows for the imaging of organic compounds at miniscule concentrations. Another example, dating back to the late 1980s[3], is the use of intravenous contrast agents to reveal information about the hemodynamic state of the microvasculature. Characterizing the delivery of arterial blood through the capillary bed is of great interest in many diseases, such as stroke[4], impaired function of the abdominal organs[5], and cancer[6].

The theoretical groundwork for another functional technique, known today as diffusion-weighted MRI (DW-MRI), was laid by Torrey[7] as early as 1956, and it has since found numerous applications and became widely used in clinical MRI. DW-MRI offers the unique possibility to assess the displacement of water molecules inside the tissue due to their thermal molecular (or Brownian) motion[8], which was demonstrated to be of pivotal value in the detection of ischemic regions in the brain by Moseley et al.[9] in 1990. Further main areas of application are the tracking of nerve fiber bundles in white matter[10,11], as well as the diagnosis and characterization of tumorous lesions throughout the entire body[12]. However, DW-MRI is not only sensitive to thermal molecular diffusion, but also to incoherent motion of water molecules in general, coining the term *intravoxel incoherent motion* (IVIM) MRI[13,14]. A primary source of such motion (in addition to thermal molecular diffusion) is capillary perfusion. This opens up the possibility of assessing tissue hemodynamics without the need for intravenous contrast agents, which is a highly desirable prospect for the diagnosis of many diseases. Accordingly, IVIM MRI is a topic of current research and its value has been demonstrated in the examination of abdominal organs[15–18], lesion characterization[19,20], and the monitoring of anticancer therapy[21–24], to name a few.

Virtually all studies performing IVIM MRI measurements model the particle displacement due to capillary perfusion as a pseudo-diffusion coefficient, which results in a biexponential signal decay as a function of the applied diffusion weighting. This model follows from the assumptions that the capillary bed is a network of a vast number of randomly oriented channels and that the flowing particles are traversing from one channel to the next numerous times during the measurement, describing a diffusion-like motion. While these assumptions significantly simplify the analysis of the measured data, it is often unclear if the preconditions for this model to be valid are met, which limits the physiological interpretation and accuracy of the obtained parameters. Recent studies have addressed and also capitalized on this issue, improving upon the confidence in the estimated parameters[25] and even extracting additional knowledge from the measured data[26,27]. Specifically, findings of Wetscherek et al.[26] indicated that the pseudo-diffusion limit was not reached in

common DW-MRI experiments in the liver and pancreas. They also presented a new "phase-distribution" IVIM method using numerical simulation of particle pathways to generate statistical distributions of spin phases depending on flow properties and gradient timing. This phase-distribution approach does not assume the pseudo-diffusion limit and allows one to estimate the average particle speed due to blood flow as well as the average length of a capillary segment, information previously obscured in the pseudo-diffusion coefficient. In contrast to the pseudo-diffusion model, the phase-distribution method also allows for the explicit consideration of a statistical distribution of particle speeds.

While Wetscherek et al. obtained physiologically reasonable parameter estimates, the (quantitative) validation of IVIM MRI methods is inherently difficult. Quantities such as the blood flow velocity, the perfusion fraction, and the capillary length are extremely challenging, if not impossible, to determine in vivo without the use of highly invasive methods and can hardly be regulated. However, assessing the performance of a medical measurement procedure under varying conditions is essential to provide confidence in the estimated parameters and to facilitate physiological interpretation.

The purpose of this thesis is to approach this problem by assessing and comparing conventional pseudo-diffusion IVIM MRI and phase-distribution IVIM MRI experimentally using a perfusable capillary phantom closely matching the geometry of in vivo capillary beds. A primary objective is to identify each method's domain of validity with regard to the characteristics of the underlying capillary flow. Achieving this goal entails the construction of a phantom featuring the controlled application of fluid flow at an adjustable rate to generate varying perfusion conditions. The detailed characterization of the constructed capillary network using direct measurements (i.e., optical microscopy) serves as a basis for the validation of different applied IVIM MRI methods. Building on this, the potential of phase-distribution IVIM MRI to generate accurate and intuitive parameter estimates is investigated. Furthermore, the limits to the applicability of simplified models are evaluated to elucidate the consequences of inaccurate model assumptions on the validity of the estimated parameters. As a secondary goal, detailed numerical simulations aim to consolidate the experimental findings and to advance the understanding of the effects of flow characteristics on data measured with DW-MRI.

Chapters 2 to 4 of this thesis review the theoretical background of DW-MRI and the current state of the literature regarding the analysis of perfusion effects using IVIM techniques. Chapter 5 focuses on the employed numerical methods and presents several theoretical results based on simulation studies. Chapter 6 describes the construction and characterization of the capillary phantom followed by the main experimental results and initial discussion in chapter 7. Finally, chapter 8 reviews the obtained results with regard to the literature and discusses potential consequences of the presented work.

2 Nuclear Magnetic Resonance

This chapter covers the basic principles of nuclear magnetic resonance (NMR), the physical phenomenon utilized to perform magnetic resonance imaging (MRI). A brief overview of the nuclear spin and the magnetic moment of a nucleus (section 2.1) is followed by a discussion of how the interaction between nuclei and an external magnetic field (section 2.2) leads to the formation of a macroscopic magnetization (subsection 2.2.1). Subsequently, it is shown how this macroscopic magnetization can be harnessed using a radiofrequency pulse to generate a measureable signal (section 2.3) and how the time evolution governed by the Bloch equations leads to restoration of the initial equilibrium (section 2.4). Finally, the refocusing of spin magnetization is described in section 2.5. For a more detailed discussion the reader may be referred to the work by Abragam[28].

2.1 Nuclear Spin and Magnetic Moment

An atomic nucleus possess a total angular momentum $\boldsymbol{I}$, characterized by a quantum number that may be zero, half-integer or integer depending on the fermionic configuration. It is related to the magnetic moment $\boldsymbol{\mu}$ of the nucleus via

$$\boldsymbol{\mu} = \gamma \boldsymbol{I}, \tag{2.1}$$

defining the nucleus-specific gyromagnetic ratio γ. In clinical MRI the primary nucleus is hydrogen, with $\boldsymbol{I} = 1/2$ and $\gamma = 2.675 \times 10^8$ rad $\mathrm{T}^{-1}\mathrm{s}^{-1}$.

In quantum mechanics, the operator $\hat{\boldsymbol{I}} = \left(\hat{I}_x, \hat{I}_y, \hat{I}_z\right)$ obeys the commutation relation

$$\left[\hat{I}_i, \hat{I}_j\right] = i\hbar\varepsilon_{ijk}\hat{I}_k \tag{2.2}$$

$$\left[\hat{\boldsymbol{I}}^2, \hat{I}_i\right] = 0 \tag{2.3}$$

with the commutator $\left[\hat{A}, \hat{B}\right] = \hat{A}\hat{B} - \hat{B}\hat{A}$. Quantized along the z-axis, the equations for the eigenvalues of $\hat{\boldsymbol{I}}$ are given by

$$\hat{\boldsymbol{I}}^2|I, m\rangle = \hbar^2 I(I+1)|I, m\rangle \tag{2.4}$$

$$\hat{I}_z|I, m\rangle = \hbar m|I, m\rangle, \tag{2.5}$$

with the nuclear spin quantum number I and the magnetic quantum number m. The quantum number m can take values from $-I, -I+1, \cdots, I$ and characterizes the $2I+1$ possible energy states of a nuclear spin in an external magnetic field (see section 2.2).

2.2 Influence of an External Magnetic Field

Magnetic resonance is based on the interaction of the magnetic moment $\boldsymbol{\mu}$ and an external magnetic field $\boldsymbol{B}$ described by the Hamiltonian

$$\hat{H} = -\hat{\boldsymbol{\mu}} \cdot \boldsymbol{B} = -\gamma \hat{\boldsymbol{I}} \boldsymbol{B}, \tag{2.6}$$

which simplifies to $\hat{H} = -\gamma \hat{I}_z B_0$, in the case of a stationary magnetic field of strength B_0 along the z-axis. Since the eigenfunctions of $\hat{\boldsymbol{I}}$ are simultaneous eigenfunctions of $\hat{H}$, the energy levels E_m of the time-independent Schrödinger equation $\hat{H}|I,m\rangle = E_m|I,m\rangle$ can be found using equations (2.4) and (2.5) yielding

$$E_m = -\gamma \hbar m B_0. \tag{2.7}$$

The energy difference between two neighboring energy states is $\Delta E = E_m - E_{m-1} = \gamma \hbar B_0 = \hbar \omega_0$, with the Larmor frequency $\omega_0 = \gamma B_0$ being directly proportional to the magnetic field strength B_0. An oscillating magnetic field perpendicular to the static magnetic field $\boldsymbol{B}$ with frequency $\nu_0 = \frac{\omega_0}{2\pi}$ can induce transitions between neighboring energy levels.

2.2.1 Macroscopic Magnetization

Considering N nuclear spins in thermal equilibrium, the different energy states E_m are occupied with probability p_m, determined by the Boltzmann distribution

$$p_m = \frac{e^{\frac{-E_m}{kT}}}{\sum_{m=-I}^{I} e^{\frac{-E_m}{kT}}} = \frac{e^{\frac{\hbar m \omega_0}{kT}}}{\sum_{m=-I}^{I} e^{\frac{\hbar m \omega_0}{kT}}} = \frac{N_m}{N}. \tag{2.8}$$

For hydrogen at body temperature ($T = 310$ K) and at magnetic field strength $B_0 = 3$ T, this translates to a seemingly miniscule relative difference in occupation of $\Delta N/N = 9.89 \cdot 10^{-6}$. However, the summation of the expected magnetization $\langle \hat{\boldsymbol{\mu}}_{\boldsymbol{k}} \rangle$ of a sufficiently large number of protons per volume V, as present in the human body, builds up to a measureable macroscopic magnetization $\boldsymbol{M}$

$$\boldsymbol{M} = \frac{1}{V} \sum_{k=1}^{N} \langle \hat{\boldsymbol{\mu}}_{\boldsymbol{k}} \rangle = \frac{\gamma}{V} \sum_{k=1}^{N} \langle \hat{\boldsymbol{I}}_{\boldsymbol{k}} \rangle. \tag{2.9}$$

The macroscopic magnetization is aligned along the external magnetic field (since the x and y components of the expected magnetization equal zero) and the magnetization M_0 in thermal equilibrium is

$$M_0 = \frac{\gamma}{V} \sum_{k=1}^{N} \langle \hat{I}_z \rangle = \frac{\gamma \hbar N}{V Z(T)} \sum_{m=-I}^{I} m e^{\frac{\hbar m \omega_0}{kT}}, \tag{2.10}$$

with the partition function $Z(T)$. For $\hbar\omega_0 \ll kT$ (which is certainly satisfied at body temperature), the high-temperature approximation can be used to simplify M_0 by doing a first-order expansion:

$$M_0 \approx \frac{N}{V}\frac{\gamma^2\hbar^2 I(I+1)B_0}{3kT}. \tag{2.11}$$

Consequently, M_0, which translates directly to the obtainable signal-to-noise ratio (SNR) using MRI, is directly proportional to the spin density N/V as well as to the square of γ. This predestines the hydrogen nucleus for clinical MRI since it is abundant in biological tissue in the form of water molecules and has a large gyromagnetic ratio.

The time evolution of $\boldsymbol{M}$ can be anticipated by considering the time evolution of an individual magnetic moment $\boldsymbol{\mu}$ given by

$$\frac{d\langle\hat{\boldsymbol{\mu}}\rangle}{dt} = \langle\frac{i}{\hbar}\left[\hat{H},\hat{\boldsymbol{\mu}}\right]\rangle = \frac{i\gamma^2}{\hbar}\langle\hat{\boldsymbol{I}}\left(\hat{\boldsymbol{I}}\cdot\boldsymbol{B}\right) - \left(\hat{\boldsymbol{I}}\cdot\boldsymbol{B}\right)\hat{\boldsymbol{I}}\rangle. \tag{2.12}$$

Component-wise evaluation using the Einstein notation yields

$$\hat{I}_k\hat{I}_l B_l - \hat{I}_l B_l \hat{I}_k = B_l\left(\hat{I}_k\hat{I}_l - \hat{I}_l\hat{I}_k\right) = B_l\left[\hat{I}_k,\hat{I}_l\right] = i\hbar B_l\hat{I}_m\varepsilon_{klm} = i\hbar\left(\boldsymbol{B}\times\hat{\boldsymbol{I}}\right)_k, \tag{2.13}$$

leading to the time evolution of $\boldsymbol{M}$ by summation over N particles in a volume V:

$$\frac{d\boldsymbol{M}}{dt} = \frac{1}{V}\sum_{k=1}^{N}\langle\frac{d\hat{\boldsymbol{\mu}}_{\boldsymbol{k}}}{dt}\rangle = \frac{\gamma}{V}\sum_{k=1}^{N}\langle\hat{\boldsymbol{\mu}}_{\boldsymbol{k}}\rangle\times\boldsymbol{B} = \gamma\boldsymbol{M}\times\boldsymbol{B}. \tag{2.14}$$

The solution to this gyroscopic equation corresponds to a precession of $\boldsymbol{M}$ around the direction of $\boldsymbol{B}$ with the angular frequency $\omega_0 = \gamma|\boldsymbol{B}|$.

2.3 Excitation

The angle α between $\boldsymbol{M}$ and $\boldsymbol{B} = (0,0,B_0)$ can be affected by applying an additional radiofrequency field $\boldsymbol{B}_1(t) = B_1\cdot(\cos(\omega_1 t), \sin(\omega_1 t), 0)$, polarized perpendicular to the axis of $\boldsymbol{B}$. The time dependence of the total magnetic field needs to be accounted for in eq. (2.14) yielding

$$\frac{d\boldsymbol{M}(t)}{dt} = \gamma\boldsymbol{M}(t)\times(B_1\cos(\omega_1 t), B_1\sin(\omega_1 t), B_0). \tag{2.15}$$

A simplified form of eq. (2.15) can be obtained by performing a transformation[29] from the laboratory system $(x,y,z,)$ into a coordinate system rotating with frequency ω_1 around the axis of $\boldsymbol{B}$ ($x' = x\cos(\omega_1 t) + y\sin(\omega_1 t)$, $y' = -x\sin(\omega_1 t) + y\cos(\omega_1 t)$, $z' = z$):

$$\frac{d\boldsymbol{M}(t)}{dt} = \gamma\boldsymbol{M}(t)\times\left(B_1, 0, B_0 - \frac{\omega_1}{\gamma}\right) = \gamma\boldsymbol{M}(t)\times\boldsymbol{B}_{\text{eff}}. \tag{2.16}$$

Again, the macroscopic magnetization performs a precession around the axis of the introduced effective magnetic field $\boldsymbol{B}_{\text{eff}} = \left(B_1, 0, B_0 - \frac{\omega_1}{\gamma}\right)$ with frequency $\omega_{\text{eff}} = \gamma \|\boldsymbol{B}_{\text{eff}}\|$. If the applied radio frequency meets the resonance condition $\omega_1 = \omega_0$, the z-component of $\boldsymbol{B}_{\text{eff}}$ vanishes and M rotates solely around the x-axis. This causes the angle α between $\boldsymbol{M}$ and $\boldsymbol{B} = (0,0,B_0)$ to vary depending on the duration t_{RF} and the strength B_1 of the applied radio frequency pulse

$$\alpha = \gamma B_1 t_{RF}. \tag{2.17}$$

After turning off the radiofrequency field, the accrued transverse magnetization $M_{xy} = M_0 \sin(\alpha)$ rotates around the axis of $\boldsymbol{B}$ with ω_0 in the laboratory system and can be expressed using the complex notation

$$M_{xy}(t) = M_{xy}(t_0) e^{i\omega_0 t} = M_x(t) + iM_y(t). \tag{2.18}$$

A temporary radiofrequency field is referred to as a radiofrequency pulse, while the change in the angle α between $\boldsymbol{M}$ and $\boldsymbol{B}$ caused by said pulse is referred to as its *flip angle*.

In turn, the resulting rotating transverse magnetization $M_{xy}(t)$ induces an electric current in the radiofrequency coils, which constitutes the measured signal $S(t)$ that ultimately leads to image formation (see chapter 3).

2.4 Relaxation

Interactions of the excited spins with their surrounding (spin-lattice) as well as among each other (spin-spin) cause relaxation processes and eventually the equilibrium magnetization $\boldsymbol{M}_0$ is restored.

T_1 Relaxation

The relaxation of the longitudinal magnetization M_z along the axis of $\boldsymbol{B}$ is facilitated by the thermal motion of the spins creating fluctuating magnetic fields. These fields carry spectral components at the Larmor frequency, thereby inducing transitions between the energy levels E_m at a specific rate $R_1 = 1/T_1$. Consequently, the spin-lattice relaxation time T_1 characterizes the exponential restoration of M_z. The energy released by this relaxation process is transferred as heat to the lattice, e.g. the measured object.

T_2 Relaxation

Conversely, the spin-spin relaxation time T_2 characterizes the decay of the transverse magnetization M_{xy} caused by a loss of phase coherence of the spins. Immediately after applying a radiofrequency pulse, excited spins rotate with a coherent phase around the z-axis. However, by inevitable dipole-dipole interactions, the spins experience small random variations in their local magnet fields causing discrepancies in their precession frequency and thereby leading to an irreversible loss of their phase coherence.

Additional local inhomogeneities in the magnetic field caused by magnetic inference fields (e.g. due to changes in susceptibility at surface boundaries) may dephase the spins as well, which is

termed T_2'-relaxation. Due to the static nature of these inference fields, the T_2'-relaxation is a reversible process by inverting the phases using a 180° inversion pulse (see section 2.5). The entire decay of the transverse magnetization M_{xy} can be summarized by the constant T_2^*

$$\frac{1}{T_2^*} = \frac{1}{T_2} + \frac{1}{T_2'}. \tag{2.19}$$

Generally[30] (but not in principle[31]), T_1 is greater than T_2. Within the range of clinically used magnetic field strengths of $0.5 - 3$ T, T_1 is more susceptible to the strength of the external magnetic field than T_2. However, at very high fields of 7 T and above, T_2 values of most tissues shorten substantially[32]. Furthermore, since T_2^* is influenced by field inhomogeneities, T_2^* is always equal or shorter than T_2 (as is evident from equation (2.19)).

Bloch equations

In 1946 Felix Bloch introduced empirically found equations[33], describing the aforementioned relaxation processes:

$$\frac{dM_x(t)}{dt} = \gamma(\boldsymbol{M}(t) \times \boldsymbol{B}(t))_x - \frac{M_x(t)}{T_2} \tag{2.20}$$

$$\frac{dM_y(t)}{dt} = \gamma(\boldsymbol{M}(t) \times \boldsymbol{B}(t))_y - \frac{M_y(t)}{T_2} \tag{2.21}$$

$$\frac{dM_z(t)}{dt} = \gamma(\boldsymbol{M}(t) \times \boldsymbol{B}(t))_z - \frac{M_z(t) - M_0}{T_1}. \tag{2.22}$$

Eqs. (2.20)-(2.22) can also be expressed in matrix form:

$$\frac{d\boldsymbol{M}(t)}{dt} = \gamma \boldsymbol{M}(t) \times \boldsymbol{B}(t) - \begin{pmatrix} 1/T_2 & 0 & 0 \\ 0 & 1/T_2 & 0 \\ 0 & 0 & 1/T_1 \end{pmatrix} (\boldsymbol{M}(t) - \boldsymbol{M_0}). \tag{2.23}$$

Using the previously introduced transverse magnetization M_{xy}, the solutions of the Bloch equations in the case of a constant and homogenous external magnetic field $\boldsymbol{B} = (0, 0, B_0)$ are given by

$$M_z(t) = M_0 - (M_0 - M_z(t_0))e^{-\frac{t}{T_1}} \tag{2.24}$$

$$M_{xy}(t) = M_{xy}(t_0)e^{i\omega_o t}e^{-\frac{t}{T_2}}. \tag{2.25}$$

In accordance with the previous description, M_z recovers exponentially with the time constant T_1, whereas M_{xy} decays exponentially with the time constant T_2 (since we ruled out field inhomogeneities), whilst precessing around the z-axis with the Larmor frequency ω_0. This time evolution of the magnetization is referred to as *free induction decay* (FID).

2.5 Echo generation

In the previous section it was mentioned that the T_2'-relaxation, caused by constant local inhomogeneities in the magnetic field, can be reversed.

Spin Echo

This can be achieved by irradiating a 180° pulse after a predefined delay $t = TE/2$ following the 90° (or any other flip angle) excitation pulse as is illustrated in Figure 2.1. The constant local inhomogeneities in the magnetic field cause spins to rotate at slightly varying frequencies depending on their spatial position, resulting in the accumulation of a phase. The 180° RF pulse inverts the magnetization vectors as well as the phases. Spins rotating at increased frequencies now have a delayed phase and are catching up with slower rotating spins. As the local precession frequencies are unaffected by the 180° pulse, the spins eventually rephase at the echo time $t = TE$, forming the so-called *spin echo*. The spin echo was initially discovered by Erwin Hahn[34] in 1950 and is the basis many modern MRI pulse sequences.

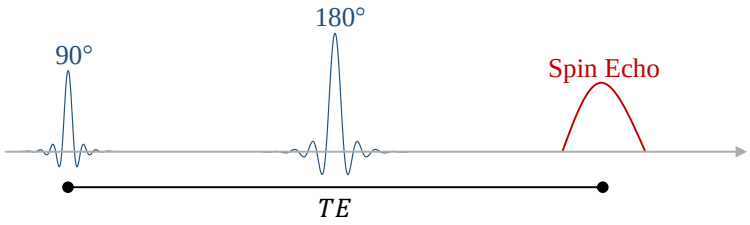

Figure 2.1: Generation of a spin echo: A 90° excitation pulse is followed by a predefined delay $t = TE\ /\ 2$ and a subsequent 180° pulse designed to reverse the T_2'-relaxation by inverting the phase of the precessing spins, causing them to form a spin echo at $t = TE$.

Stimulated Echo

Another sequence of pulses, designed to circumvent the excessive loss of signal due to relaxation processes, results in the formation of so-called stimulated echoes (STE). In contrast to spin echoes, stimulated echoes are formed by irradiating two 90° pulses instead of a single 180° inversion pulse (Figure 2.2). The first 90° pulse after the excitation at $t = TE/2$ tips the transverse magnetization m_{xy} in the xz-plane. During the mixing time TM, the resulting z-component of the spins is then subject to T_1-relaxation rather than the typically much faster T_2-relaxation until at $t = TE/2 + TM$ the third 90° pulse is irradiated and flips the z-components back into the xy-plane. The spins resume their precession around the z-axis and finally form the stimulated echo at $t = TE + TM$.

While the maximum signal intensity of a STEAM pulse sequence is inherently half that of a spin-echo amplitude with an equivalent echo time TE[35], the prevention of T_2-relaxation during TM allows one to realize long intervals between the excitation pulse and the data acquisition during the echo. In the context of imaging, the acronym STEAM for stimulated echo acquisition mode was introduced by Frahm et al.[36] in 1986, however, the phenomenon of stimulated echoes was initially described by Hahn[34] in 1950 alongside the spin echo as well.

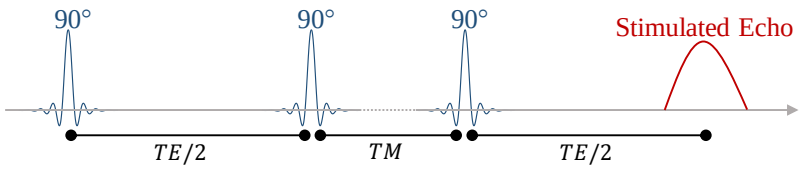

Figure 2.2: Generation of a stimulated echo: A 90° excitation pulse is followed by a predefined delay $t = TE\ /\ 2$ and a subsequent 90° pulse, tipping the transverse magnetization m_{xy} in the xz-plane. After the mixing time TM, a third 90° pulse flips the z-components back into the xy-plane, where the spins resume their precession around the z-axis and finally form the stimulated echo at $t = TE + TM$.

3 Magnetic Resonance Imaging

Having introduced nuclear magnetic resonance in the previous chapter, means to use this phenomenon for the formation of tomographic images will now be discussed. In section 3.1, the spatial encoding of the generated signal using magnetic gradient fields is shown. Section 3.2 explains how the magnetization can be selectively excited, effectively reducing the problem of spatial encoding to two dimensions, followed by a brief discussion of the concept of k-space in section 3.3. Finally, putting these aspects into context, one of the simplest and most relevant MRI pulse sequences, the spin-echo pulse sequence, is presented in section 3.4.

3.1 Gradient Fields and Spatial Encoding

To achieve a spatial encoding of the Larmor frequency ω_0, gradient coils are used to superimpose a linear magnetic gradient field $B_{z,g}$ in the form of

$$B_{z,g}(\boldsymbol{x}, t) = \boldsymbol{x} \cdot \boldsymbol{g}(t), \tag{3.1}$$

with the magnetic field gradient $\boldsymbol{g} = \nabla B_z = \left(\frac{\partial B_z}{\partial x}, \frac{\partial B_z}{\partial y}, \frac{\partial B_z}{\partial z}\right)$, onto the static magnetic field $\boldsymbol{B} = (0, 0, B_0)$. Consequently, the Larmor frequency will then be spatially dependent:

$$\omega(\boldsymbol{x}, t) = \gamma B_z(\boldsymbol{x}) = \gamma B_0 + \gamma \boldsymbol{x} \cdot \boldsymbol{g}(t). \tag{3.2}$$

Solving the Bloch equations in a rotating reference frame while taking this spatial dependency as well as a local spin density $\rho(\boldsymbol{x}) = N/V$ under account leads to

$$M_z(\boldsymbol{x}, t) = M_0(\boldsymbol{x}) - \big(M_0(\boldsymbol{x}) - M_z(\boldsymbol{x}, t_0)\big) e^{-\frac{t}{T_1}} \tag{3.3}$$

$$M_{xy}(\boldsymbol{x}, t) = M_{xy}(\boldsymbol{x}, t_0) e^{-i\phi(\boldsymbol{x},t)} e^{-\frac{t}{T_2}}, \tag{3.4}$$

where the effect of $\boldsymbol{g}$ on the equilibrium magnetization M_0 was assumed to be negligible (since the superimposed gradient field is typically small compared to the static field). The time evolution of the longitudinal magnetization M_z remains unchanged compared to equation (2.24), whereas the transverse magnetization accumulates a spatially dependent phase $\phi(\boldsymbol{x}, t)$:

$$\phi(\boldsymbol{x}, t) = \int_0^t \omega(\boldsymbol{x}, t')\, \mathrm{d}t' = \omega_0 t + \gamma \boldsymbol{x} \cdot \int_0^t \boldsymbol{g}(t') \mathrm{d}t' = \omega_0 t + \boldsymbol{k}(t)\boldsymbol{x}, \tag{3.5}$$

using the definition of the spatial wave vector

$$\boldsymbol{k}(t) = \gamma \int_0^t \boldsymbol{g}(t')\, \mathrm{d}t'. \tag{3.6}$$

The measured signal intensity $S(t)$ is proportional to the transverse magnetization M_{xy} and integration of eq. (3.4) over the volume V leads to

$$S\big(\boldsymbol{k}(t)\big) \propto \int_V M_{xy}(\boldsymbol{x}, t_0)\, e^{-i\boldsymbol{k}(t)\cdot\boldsymbol{x}}\, \mathrm{d}^3\boldsymbol{x}, \tag{3.7}$$

where the decay of the transverse magnetization due to T_2-relxation was neglected and the high frequency phase modulation $e^{i\omega_0 t}$ has been dropped. Eq. (3.7) dictates that the signal $S(\boldsymbol{k})$, measured in *k*-space, is proportional to the Fourier transform of the spatial distribution of the transverse magnetization $M_{xy}(\boldsymbol{x})$. Hence, measuring the signal $S(k_i)$ in a sufficient number of points k_i, $M_{xy}(\boldsymbol{x})$ can be reconstructed from the measured signal via the inverse Fourier transform:

$$M_{xy}(\boldsymbol{x}) \propto \int_{V_k} S(\boldsymbol{k_i}) e^{i\boldsymbol{k}_i\cdot\boldsymbol{x}} \mathrm{d}^3\boldsymbol{k}. \tag{3.8}$$

3.2 Slice-Selective Excitation

To reduce the problem of spatial encoding to just two dimensions, slice-selective excitation can be employed. According to equation (3.2), a superimposed magnetic gradient field results in a spatially dependent Larmor frequency $\omega(\boldsymbol{x})$. Assuming the gradient direction to be parallel to the z-axis, a radiofrequency pulse $B_1(t)$ with frequency ω_1 will then meet the resonance condition $\omega_1 = \omega(z) = \gamma B_0 + \gamma z \cdot g_z$ for just a single xy-plane. By using a radiofrequency pulse with a bandwidth $\Delta\omega$, protons inside a slice with finite thickness Δz can be exited (Figure 3.1).

The slice thickness Δz is therefore subject to the strength of the magnetic field gradient g and to the bandwidth size $\Delta\omega$ of the irradiated radio frequency:

$$\Delta z = \frac{\Delta\omega}{\gamma g}. \tag{3.9}$$

Using slice-selective excitation, the signal in eq. (3.7) becomes

$$S\big(k_x, k_y, t\big) \propto \int_{x,y} M_{xy}(x, y, t_0)\, e^{-i(k_x x + k_y y)} \mathrm{d}x\mathrm{d}y. \tag{3.10}$$

Spatial encoding and *k*-space sampling is then reduced to just two dimensions to be able to reconstruct a single tomographic image of a slice with thickness Δz.

Upon further consideration[37], the solution of the Bloch equations for the transverse magnetization M_{xy} in presence of a constant magnetic field gradient can be approximated for small flip angles by

$$\frac{\big|M_{xy}(t, \Delta\omega)\big|}{M_0} \approx \gamma \left| \int_0^t B_1(t) e^{i\Delta\omega t} \mathrm{d}t \right|. \tag{3.11}$$

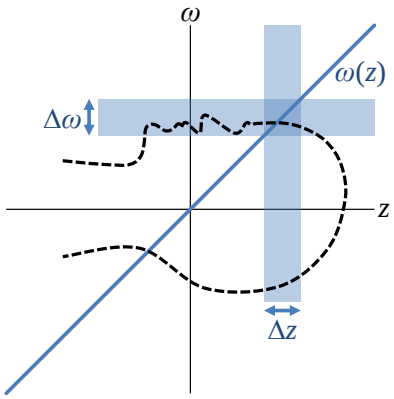

Figure 3.1: Slice-selective excitation: A linear magnetic gradient field in the $\boldsymbol{z}$-direction is superimposed onto $\boldsymbol{B}$ while a radiofrequency pulse with bandwidth $\Delta\boldsymbol{\omega}$ is applied. The resonance condition is met only for protons within $\Delta\boldsymbol{z}$, resulting in a single excited slice perpendicular to the gradient direction.

Accordingly, the slice profile of M_{xy} is given by the Fourier transform of the envelope function $B_1(t)$. A perfectly rectangular profile can theoretically be obtained by using an sinc-pulse[37] (of infinite duration)

$$B_1(t) = B_1 \operatorname{sinc}\left(t\frac{\Delta\omega}{2}\right), \tag{3.12}$$

however, the sinc-pulse can only be applied for a finite duration and therefore needs to be pruned, resulting in small deviations from a perfect rectangular shape in the magnetization profile.

3.3 k-Space Sampling

The navigation through k-space, i.e. the manipulation of $\boldsymbol{k}(t)$, is subject to the gradient field $\boldsymbol{g}(t)$, which in turn is manipulated by specifically designed gradient coils. There are three gradient coils in an MRI-system, one for each axis, allowing for arbitrary trajectories through k-space. Recalling eq. (3.6), in the two-dimensional case, the located k-space point is $(k_x, k_y) = \gamma(g_x t_x,\ g_y t_y)$. In the following, the k-space trajectory and sampling scheme will be related to the resolution and field of view (FOV) of the reconstructed images. For simplification, the spatial encoding will be reduced to a single dimension x.

Due to technical constraints, the k-space trajectory can only be sampled discretely, usually on an equidistantly spaced grid of N points. Rewriting eq. (3.8) for the one-dimensional case using the inverse discrete Fourier transform (DFT) yields

$$M_{xy}(x) \propto \sum_{n=-N/2}^{N/2} S(n\Delta k)e^{ixn\Delta k}, \tag{3.13}$$

with steps $\Delta k = \gamma G \Delta t$. Thus, the reconstructed distribution of the transverse magnetization appears periodically around the image center with field of view

$$FOV = \frac{2\pi}{\Delta k}. \tag{3.14}$$

As a consequence, for imaged objects larger than the FOV, the reconstructed magnetization distribution overlaps. This is referred to as aliasing effect.

The resolution Δx of the reconstructed image is given by

$$\Delta x = \frac{FOV}{N} = \frac{\pi}{k_{max}}, \tag{3.15}$$

with the width of the sampled k-space

$$k_{max} = \frac{N \Delta k}{2}. \tag{3.16}$$

As the width of the sampled k-space is increased, the resolution of the reconstructed image improves. It can further be anticipated, that the lower frequencies sampled at the k-space center define the image contrast, while high frequencies sampled at k_{max} allow to resolve smaller details.

3.4 Spin-Echo Pulse Sequence

Having the physical phenomena of nuclear magnetic resonance and the fundamentals of image formation in mind, it is now possible to discuss one of the simplest and most relevant MRI pulse sequences, the spin-echo pulse sequence (Figure 3.2).

The sequence begins with slice selective excitation using a RF pulse with a 90° flip angle while applying a magnetic gradient field g_z along the z-axis. As the gradients fields cannot be employed arbitrarily fast, they are typically trapezoidal in shape, with a short ramp-up and ramp-down time. The spin dephasing evoked by the slice selection gradient is counteracted by a subsequent gradient with inverse sign, followed by the first step of spatial encoding in the xy-plane: a gradient g_x along the x-axis is employed to target the k-space coordinate $(k_x, k_y) = (-k_{max}/2, 0)$.

Next, a second RF pulse, albeit with a flip angle of 180°, is applied, designed to reverse the T_2'-relaxation. Alike the 90° excitation pulse, the 180° inversion pulse is also made slice selective by employing a simultaneous gradient along the z-axis.

The next step is referred to as phase-encoding: a gradient in y-direction with varying strength g_y moves the targeted coordinate to the beginning of the k-space line $(k_x, k_y) = (-k_{max}/2, \gamma g_y t_y)$, that is to be read out during the current excitation. In a simple spin-echo sequence, the k-space is sampled in a line-wise fashion, while the respective k_y-coordinate of the sampled line is defined by the phase encoding step, i.e. the gradient strength g_y. By performing repeated excitations with varying gradient strengths g_y, eventually the entire selected *k*-space can be sampled.

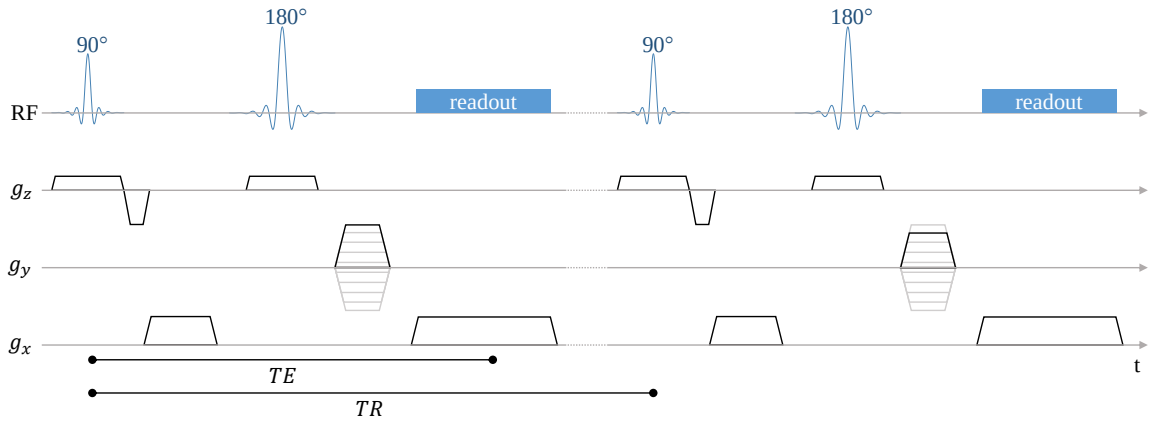

Figure 3.2: Diagram of a spin-echo sequence. Slice-selective excitation is followed by a gradient g_x along the x-axis to target the $k_x = -k_{max}$ coordinate. At $t = TE/2$ a second RF pulse with a flip angle of 180° is applied. The k_y coordinate is then targeted by a gradient with varying strength g_y. During the *readout* centered around $t = TE$, the RF signal is sampled at a specific number of equidistantly spaced points, while a gradient g_x moves the k-space coordinate from $k_x = -k_{max}$ to $k_x = k_{max}$. After the *repetition time* TR, a new excitation cycle begins to sample the next line in k-space.

A respective excitation cycle is concluded with the *readout* centered around $t = TE$, where the signal is recorded. A gradient g_x thereby moves the k-space coordinate from $k_x = -k_{max}$ to $k_x = k_{max}$, while the RF signal (measured with a dedicated receive coil) is sampled at a specific number of equidistantly spaced points, determined by the desired image matrix. After the *repetition time TR*, the next excitation cycle begins in order to sample the successive k-space line.

Aside from image characteristics such as resolution and field of view, the user is at liberty to freely adjust the *echo time* TE as well as the *repetition time* TR (aside from certain technical limitations and the obvious condition: $TE < TR$), achieving the desired image contrast:

- The influence of the T_2-relaxation on the image contrast (T_2-weighting) is defined by TE. A short TE ($TE \ll T_2$) causes the T_2-relaxation to be cut short, mitigating most of its impact on the image contrast. Yet, by choosing a long TE ($TE \sim T_2$), the image contrast is heavily influenced by the T_2-relaxation times of the respective tissue, where tissues with short T_2 times will appear dark and tissues with long T_2 times will be bright in comparison (T_2-weighted MRI).

- Varying TR will alter the T_1-weighting of the image contrast. A long TR ($TR \gg T_1$) will ensure that most of the longitudinal magnetization M_z has been restored before the next excitation cycle begins, leaving the contrast unaffected to differing T_1 relaxation times. A short TR ($TR \sim T_1$) however, does not allow for a complete restoration of M_z between successive excitations, causing tissues with long T_1 times to appear dark, while tissues with short T_1 times appear bright in comparison (T_1-weighted MRI).

As will be seen in the following chapters, there are possibilities to create image contrast based on further tissue properties, for example the thermal diffusion of the water molecules.

4 Diffusion-Weighted MRI

In this chapter, the fundamentals of diffusion-weighted magnetic resonance imaging (DW-MRI) will be discussed. Section 4.1 covers the free diffusion process of particles in liquids and gas, followed by the implications of this diffusive motion on the time-evolution of the magnetization in magnetic resonance experiments (section 4.2). The different pulse sequences used in the course of this work are covered in section 4.3, and section 4.4 discusses flow-induced spin dephasing in DW-MRI experiments[26,27].

4.1 Free Diffusion Process

At temperatures above absolute zero, all particles in liquids or gases possess thermal energy manifested by kinetic motion. Due to interactions with adjacent particles, the fashion of this motion is random and it is referred to as diffusion. The free diffusion process can be described quantitatively using Fick's laws of diffusion[38], where the first law relates the diffusion flux vector $\boldsymbol{j}$ to a concentration gradient ∇n via the diffusion coefficient D:

$$\boldsymbol{j} = -D\nabla n. \tag{4.1}$$

The diffusion coefficient D is a function of the viscosity and the temperature of the fluid as well as the size of the particles. Furthermore, the continuity equation under conservation of mass states

$$\frac{\partial n(\boldsymbol{x},t)}{\partial t} + \nabla \boldsymbol{j}(\boldsymbol{x},t) = 0, \tag{4.2}$$

yielding Fick's second law:

$$\frac{\partial n(\boldsymbol{x},t)}{\partial t} = \nabla \cdot \big(D\nabla n(\boldsymbol{x},t)\big) = D\Delta n(\boldsymbol{x},t), \tag{4.3}$$

where a constant (and scalar) diffusion coefficient D was assumed. This partial differential equation defines the change of the concentration $n(\boldsymbol{x},t)$ over time. Assuming an ensemble of particles with initial position $\boldsymbol{x}(t_0) = \boldsymbol{x}'$, the distribution of particles $n(\boldsymbol{x},t)$ is described by a three-dimensional Gaussian distribution with mean $\boldsymbol{x}'$ (Figure 4.1):

$$n(\boldsymbol{x},t) = \frac{1}{(4\pi Dt)^{3/2}} e^{\frac{-(\boldsymbol{x}-\boldsymbol{x}')^2}{4Dt}}. \tag{4.4}$$

Considering only the x-axis, the spatial distribution of particles $P_s(x,t)$ is given by a Gaussian distribution with the variance σ_x^2:

$$\sigma_x^2 = \langle x^2 \rangle = 2Dt. \tag{4.5}$$

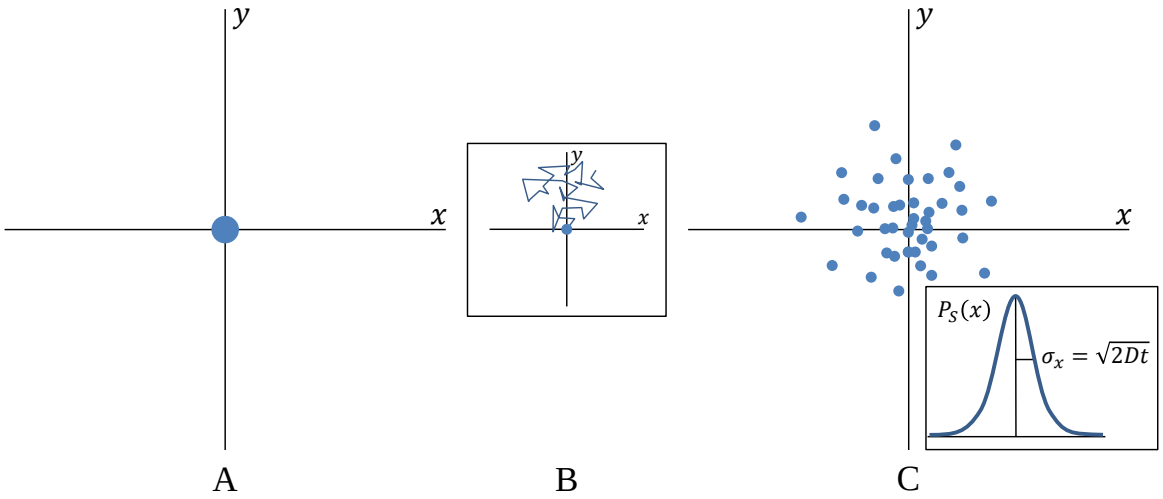

Figure 4.1: Illustration of the free diffusion process. Each particle in an ensemble with common starting position (A) performs a random walk motion as time passes (B). The distribution of particles after time t is described by a three-dimensional Gaussian distribution (C) with zero mean displacement. The standard deviation is proportional to the square root of the product of D and t (illustration after [26]).

In three dimensions the variance is given by $\sigma^2 = \langle \boldsymbol{x}^2 \rangle = 6Dt$. Thus, in contrast to a regular linear motion, the expected "translation" (root of the mean squared displacement, while the mean displacement is 0) of a single particle due to diffusion is merely increasing proportional to $\sqrt{t}$.

4.2 Bloch-Torrey Equations

The Bloch equations (eq. (2.20)-(2.22)) can be extended to include the effect of diffusive motion on the time evolution of the magnetization in magnetic resonance experiments. The resulting Bloch-Torrey equations in isotropic media (with scalar constant diffusion coefficient D and constant magnetic field $\boldsymbol{B}$ along the z-axis) are given by[7]

$$\frac{d\boldsymbol{M}}{dt} = \gamma \boldsymbol{M} \times \boldsymbol{B} - \begin{pmatrix} 1/T_2 & 0 & 0 \\ 0 & 1/T_2 & 0 \\ 0 & 0 & 1/T_1 \end{pmatrix} (\boldsymbol{M} - \boldsymbol{M_0}) + D\Delta \boldsymbol{M}. \tag{4.6}$$

In the presence of a magnetic field gradient $\boldsymbol{g}(t)$, eq. (4.6) yields for the time evolution of the transverse magnetization $M_{xy}(\boldsymbol{x}, t)$

$$\frac{\partial M_{xy}}{\partial t} = -i\gamma\big(B_0 + \boldsymbol{x} \cdot \boldsymbol{g}(t)\big) M_{xy} - \frac{M_{xy}}{T_2} + D\Delta M_{xy}. \tag{4.7}$$

To eliminate the Larmor precession as well as the T_2 signal decay, the transverse magnetization can be substituted by $M_{xy}(\boldsymbol{x},t) = m_{xy}(\boldsymbol{x},t)e^{-i\gamma B_0 t - \frac{t}{T_2}}$, simplifying eq. (4.7) to

$$\frac{\partial m_{xy}(\boldsymbol{x},t)}{\partial t} = -i\gamma m_{xy}(\boldsymbol{x},t)\boldsymbol{x}\cdot\boldsymbol{g} + D\Delta m_{xy}(\boldsymbol{x},t). \tag{4.8}$$

The measured signal in diffusion-weighted MRI is determined by the magnitude of m_{xy}. By substituting[7] $m_{xy}(\boldsymbol{x},t) = M(t)e^{-2\pi i\boldsymbol{x}\cdot\boldsymbol{k}(t)}$, using the definition of $\boldsymbol{k}$ given in eq. (3.6), the phase and magnitude of m_{xy} can be separated. The time derivative of $M(t)$ is then given by

$$\frac{\partial M(t)}{\partial t} = M(t)De^{i\boldsymbol{x}\cdot\boldsymbol{k}(t)}\Delta e^{-i\boldsymbol{x}\cdot\boldsymbol{k}(t)} = -DM(t)\boldsymbol{k}(t)\cdot\boldsymbol{k}(t), \tag{4.9}$$

and integration leads to

$$M(t) = M(0)\cdot\exp\left(-D\int_0^t \boldsymbol{k}(t')\cdot\boldsymbol{k}(t')dt'\right). \tag{4.10}$$

In a diffusion-weighted magnetic resonance experiment, the measured signal intensity at the echo time TE is therefore

$$S(TE) = S(0)\cdot\exp\left(-D\int_0^{TE} \boldsymbol{k}(t')\cdot\boldsymbol{k}(t')dt'\right) = S(0)\cdot e^{-bD}, \tag{4.11}$$

with the b-value

$$b = \gamma^2\int_0^{TE}\left(\int_0^t \boldsymbol{g}(t')dt'\right)^2 dt. \tag{4.12}$$

In a diffusion-weighted magnetic resonance experiment, the signal is attenuated due to diffusive motion and the b-value defines the strength of the diffusion weighting of the pulse sequence. As the b-value is increased, the signal attenuation due to diffusion becomes stronger, allowing one to quantify the diffusion coefficient D by repeated measurements of the signal intensity $S(b)$ with varying diffusion-weightings b_1 and b_2 as

$$D = \frac{\ln(S_{b1}/S_{b2})}{b_2 - b_1}. \tag{4.13}$$

In DW-MRI, the measured diffusion coefficient is often referred to as the apparent diffusion coefficient ADC, owed to the fact that eq. (4.11) is only correct for freely diffusing homogenous liquids or gases. Most DW-MRI applications measure diffusion coefficients within the tissue, where the water molecules interact with barriers such as cell membranes. This leads to reduction in the measured diffusion coefficient as well as deviations of the signal behavior from eq. (4.11), hence the term apparent diffusion coefficient[13].

In fact, depending on the tissue structure, the reduction in the measured diffusion coefficient

may not be isotropic. This effect is particularly strong in white matter for example, where the parallel architecture of the axons facilitates the diffusion of water molecules along their main direction, but hinders their perpendicular motion. The anisotropy of the molecular diffusion can be probed with a diffusion tensor imaging (DTI) experiment[39]. In a DTI experiment, the diffusion gradients are applied in many different spatial directions (at least 6) to calculate the diffusion tensor D_{ij} (a symmetric 3×3 matrix). The diffusion tensor contains the information about the directional dependency of the thermal diffusion and may be used to calculate a dimensionless measure called the fractional anisotropy FA via

$$FA = \sqrt{\frac{(\lambda_1 - \lambda_3)^2 + (\lambda_2 - \lambda_3)^2 + (\lambda_1 - \lambda_3)^2}{2\left({\lambda_1}^2 + {\lambda_2}^2 + {\lambda_3}^2\right)}}, \tag{4.14}$$

with the eigenvalues of the diffusion tensor λ_{1-3}. The FA is a measure of the diffusion anisotropy within an imaging voxel. Perfectly isotropic diffusion yields $FA = 0$ and approaches 1 for highly directional diffusion.

4.3 Pulse Sequence Design in DW-MRI

While the theoretical foundation of quantitative DW-MRI has been established as early as 1956[7], the applicability was hampered by high technical requirements and long acquisition times even after the introduction of clinical routine MRI in the 1980s. The total acquisition time T of a classic spin-echo sequence is given by

$$T = TR \cdot N_p \cdot N_A, \tag{4.15}$$

with the number of phase encoding steps N_p and the number of signal averages N_A. Due to limited gradient strengths, DW-MRI sequences typically have to resort to long echo times (> 50 ms) in order to achieve high b-values. Additionally, the signal-to-noise ratio is further decreased due to the diffusion weighting. This SNR starvation can be counteracted by acquiring multiple signal averages N_A and by choosing a long repetition time TR (also to avoid a T_1-weighted image contrast) to allow for a full relaxation of the longitudinal magnetization M_z. The resulting total acquisition time for multiple measurements with varying b-values may therefore be prohibitive for routine application. Without going into detail, it should also be mentioned that classic spin-echo sequences suffer from high susceptibility to artifacts caused by motion. A remedy to both of these shortcomings, a readout technique called echo-planar imaging (EPI), is introduced in subsection 4.3.1. Afterwards, the different diffusion gradient schemes used in this work are motivated and discussed in subsection 4.3.2

4.3.1 Echo-Planar Imaging

Echo-planar imaging (EPI), a readout technique designed to reduce the acquisition time in MRI sequences, was presented in 1977 by Mansfield[40], however, it was only realizable in the 1990s in clinical MRI systems. Today most DW-MRI experiments are performed using this technique, where in order to reduce the number of phase encoding steps N_p, large portions (segmented EPI)

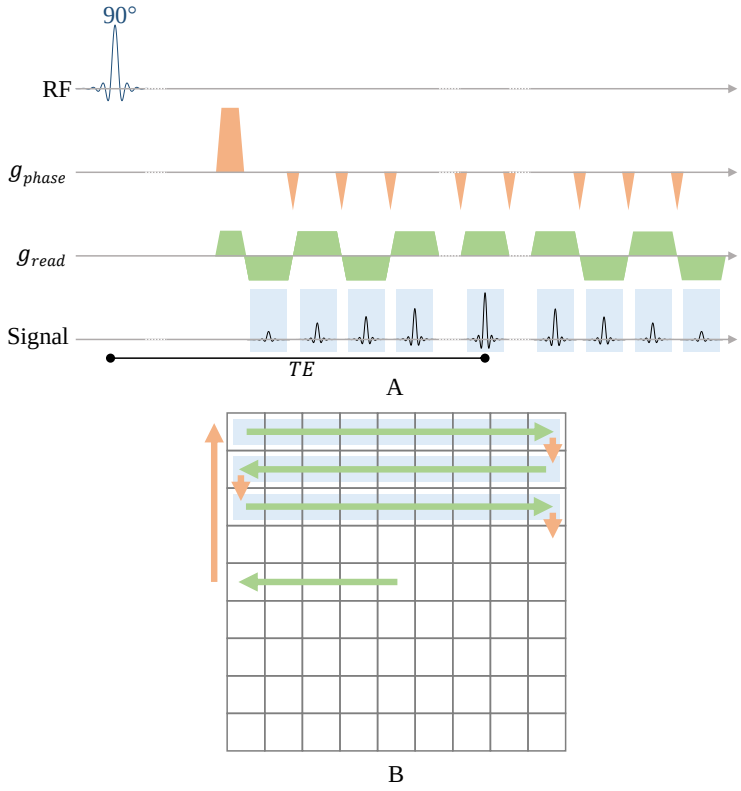

Figure 4.2: Diagram of a pulse sequence using echo-planar imaging (A) and the resulting k-space trajectory (B). After the initial localization of $(k_x, k_y) = (-k_{x_{max}}/2\,, k_{y_{max}}/2)$, oscillating gradients (green) in the readout direction, intersected by short phase-encoding blips (orange) allow for the sampling of the selected k-space in a meandering fashion (blue).

or even the entire selected k-space (single-shot EPI) is acquired during a single excitation cycle (Figure 4.2).

Using oscillating gradients in the readout direction, intersected by short phase-encoding blips, the k-space is sampled in a meandering fashion. The echo time TE of an EPI-sequence is usually defined by the point in time when the central k-space line is acquired, as it determines most of the image contrast. The refocusing pulses are timed accordingly to ensure the formation of the spin echo at $t = TE$. The pulse sequences employed for the DW-MRI experiments in this work all use the single-shot EPI readout technique.

A further advantage of single shot EPI pulse sequences (or any other fast single-shot readout technique) is the robustness to bulk motion. As the entire k-space is sampled after a single excitation, the acquired data represents a "snapshot" compared to conventional pulse sequences, where the k-space is sampled over multiple excitations and phase-encoding steps. Accordingly, the reconstructed images using single-shot-acquired data remain largely unaffected by bulk motion without the need for motion compensation techniques.

4.3.2 Diffusion Gradient Profiles

As discussed in section 4.2, the diffusion weighting or *b*-value of a sequence is determined by the strength and the timing of the applied diffusion gradients. To help understand how particle movement during the application of a magnetic field gradient may introduce a distribution of phases and therefore a change in the measured signal intensity, the concept of gradient moments is introduced.

Gradient Moments

The position $\boldsymbol{x}(t)$ of a particle can be written as a Taylor series

$$\boldsymbol{x}(t) = \boldsymbol{x_0} + t\boldsymbol{v_0} + \frac{t^2}{2}\boldsymbol{a_0} + \cdots, \tag{4.16}$$

with the starting position $\boldsymbol{x_0}$, the initial velocity $\boldsymbol{v_0}$ and the initial acceleration $\boldsymbol{a_0}$. According to eq. (3.5), the time-evolution of the phase ϕ' of the transverse magnetization M_{xy} of a particle moving along $\boldsymbol{x}(t)$ (calculated in a reference frame rotating with ω_0) is given by

$$\phi'_{\boldsymbol{x}(t)}(t) = \gamma \int_0^t \boldsymbol{x}(t') \cdot \boldsymbol{g}(t')\mathrm{d}t'. \tag{4.17}$$

Using the Taylor series for $\boldsymbol{x}(t)$ (eq. (4.16)), the phase ϕ' can be expanded to yield

$$\phi'_{\boldsymbol{x}(t)}(t) = \gamma \left(\boldsymbol{x_0} \cdot \boldsymbol{m_0}(t) + \boldsymbol{v_0} \cdot \boldsymbol{m_1}(t) + \frac{1}{2}\boldsymbol{a_0} \cdot \boldsymbol{m_2}(t) + \cdots \right), \tag{4.18}$$

with the n^{th} gradient moment $\boldsymbol{m}_n$

$$\boldsymbol{m_n}(t) = \int_0^t (t')^n \boldsymbol{g}(t')\mathrm{d}t'. \tag{4.19}$$

The 0^{th} gradient moment $\boldsymbol{m_0}$ introduces a phase based on the position $\boldsymbol{x_0}$ of the particle, which, as described in section 3.1, is utilized to encode the spatial localization in the MR signal using imaging gradients. Therefore, additional diffusion-sensitizing gradients must meet the *rephasing condition*, i.e. the total $\boldsymbol{m_0}$ of the diffusion gradient profile must be zero in order to avoid interference with the image formation and to ensure that the image contrast corresponds to the respective *b*-value.

A non-zero $\boldsymbol{m_1}$ will introduce a phase depending on the initial velocity $\boldsymbol{v_0}$. For diffusion gradient profiles with non-zero $\boldsymbol{m_1}$, bulk motion, i.e. uniform motion of all particles within a given volume with a constant velocity, will introduce a global phase, however, it is noteworthy that the magnitude of m_{xy} and therefore the signal intensity remains unaffected by this type of motion. In contrast, a set of particles moving with constant speeds albeit in different directions, for example flow in randomly oriented straight channels, will accumulate a phase based on the respective angle between the direction of the diffusion gradient $\boldsymbol{g}_d$ and each particles movement direction. This results in a distribution of phases and an attenuation of the signal as will be discussed in section 4.4. Diffusion-gradient profiles where the 1^{st} gradient moment $\boldsymbol{m_1}$ equals zero are referred to as

flow-compensated, as by using this type of gradient profile, particle movement with a constant speed void of acceleration will not introduce a phase, independent of the movement direction.

For the experiments in this work, diffusion gradient profiles with zero as well as non-zero $\boldsymbol{m_1}$ were used and will now be discussed in detail.

Monopolar spin-echo diffusion gradients

Initially devised for NMR measurements in 1965 by Stejskal and Tanner[41], the most basic diffusion-gradient profile consists of two symmetrical gradient lobes with (effectively) inverted signs (Figure 4.3). The gradient lobes are separated by a 180° inversion pulse, effectively inverting the sign of the second gradient lobe, which is thus applied in the same spatial direction as the first lobe (giving rise to the naming as *monopolar* profile). Using the notation from Figure 4.3, the b-value (eq. (4.12)) for a monopolar gradient profile b_{mp} is given by[37]

$$b_{mp} = \gamma^2 g^2 (\delta^2(\Delta - \delta/3) + \varepsilon^3/30 - \delta\varepsilon^2/6), \tag{4.20}$$

with the gradient amplitude g, the gradient duration δ, the interval between the start of the gradient lobes Δ, and the ramp time ε. Neglecting the ramp times ε for ideal rectangular gradient lobes, eq. (4.20) simplifies to

$$b_{mp} = \gamma^2 g^2 \delta^2 (\Delta - \delta/3). \tag{4.21}$$

As is depicted in Figure 4.3, the rephasing condition (total $\boldsymbol{m_0} = 0$) is met, provided the gradient lobes have the same net area. However, using this gradient profile flow-compensation (total $\boldsymbol{m_1} = 0$) cannot be achieved.

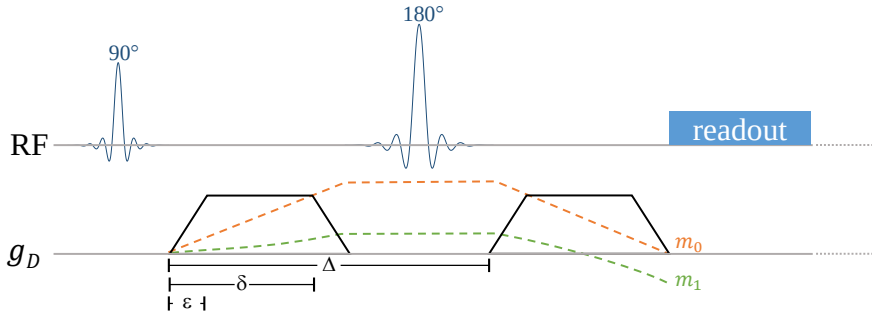

Figure 4.3: Stejskal-Tanner pulse sequence with monopolar diffusion gradient profile. The diffusion-sensitizing magnetic field gradients $\boldsymbol{g_D}$ are separated by the 180° inversion pulse, which effectively inverts the sign of the second gradient lobe. By having the same net area, the rephrasing condition is met with a zero total $\boldsymbol{m_0}$. However, the total first gradient moment $\boldsymbol{m_1}$ is non-zero, the gradient profile is therefore not flow-compensated.

Monopolar STEAM diffusion gradients

In contrast to the Stejskal-Tanner sequence, the gradient pair in the STEAM sequence is separated not by a single 180° inversion pulse, but two 90° pulses (Figure 4.4). This allows one to realize large intervals between the two gradient lobes, while avoiding an excessive loss of signal due to

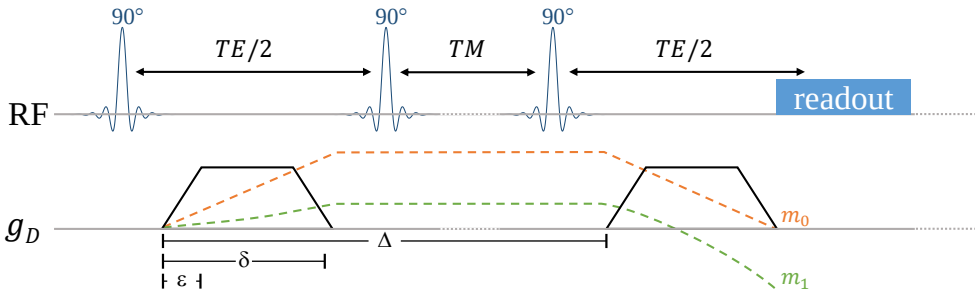

Figure 4.4: Monopolar diffusion gradient profile with STEAM pulse sequence. The two gradient lobes are separated by two 90° pulses, effectively inverting the sign of the second lobe. Analogous to the Stejskal-Tanner pulse sequence, the rephrasing condition is met with a zero total $\boldsymbol{m_0}$, while the total first gradient moment $\boldsymbol{m_1}$ is non-zero, resulting in a non-flow-compensated diffusion gradient profile.

T_2-relaxation (see section 2.5). The motivation for the use of such long intervals will become apparent in section 5.4.

As can be seen in Figure 4.4, the diffusion gradients describe a monopolar profile as well. Accordingly, the calculation of the *b*-value follows eq. (4.20) and (4.21). Alike the Stejskal-Tanner sequence, the total first gradient moment $\boldsymbol{m_1}$ is non-zero, in fact, the longer the interval between the gradient lobes is chosen (while reducing the gradient strength g_d, thus keeping the resulting *b*-value constant), the greater the absolute value of $\boldsymbol{m_1}$ will be.

Flow-compensated spin-echo diffusion gradients

A possible diffusion gradient profile achieving zero first gradient moment $\boldsymbol{m_1}$ consists of two gradient pairs separated by a 180°-pulse (as depicted in Figure 4.5). The two gradient pairs must be of (effectively) inverted sign to yield total $\boldsymbol{m_1 = 0}$. Using the notation from Figure 4.5 and neglecting the ramp times ε the *b*-value can be calculated as[37]

$$b_{fc} = \gamma^2 g^2 \frac{\delta^3}{6}, \tag{4.22}$$

with the gradient amplitude g and the bipolar gradient duration δ. As is apparent by comparing eq. (4.21) with eq. (4.22), the *b*-value of the flow-compensated diffusion gradient profile cannot be increased by elongating the interval between the start of the bipolar gradients Δ. Furthermore, assuming the limiting case $\Delta = \delta$, the flow-compensated gradients must be applied for twice the duration to achieve a *b*-value comparable to the monopolar gradient profile.

It is also noteworthy that any magnetic field gradient used throughout a pulse sequence (e.g. for slice-selective excitation or spatial encoding) affects the *b*-value as well. In quantitative DW-MRI, this becomes especially important for images without diffusion-weighting gradients, e.g. images where the *b*-value allegedly equals zero as this is de facto unobtainable in MRI. To counteract this potential source of error, in this work, the *b*-values of the images without diffusion weighting were calculated numerically using the exact timings of all employed gradients as will be discussed in subsection 7.1.3.

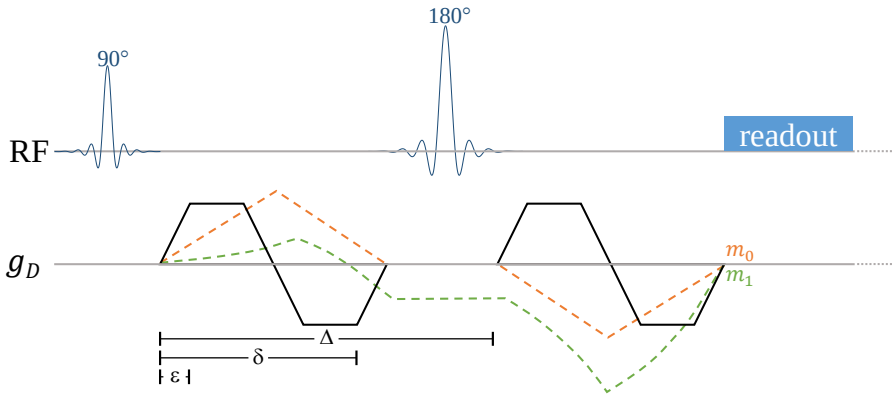

Figure 4.5: Flow-compensated diffusion-gradient profile. Two gradient pairs with effectively inverted sign are separated by a 180° pulse, yielding a zero total first gradient moment $\boldsymbol{m_1}$.

4.4 IVIM Dephasing due to Capillary Flow

Having introduced the gradient moments in subsection 4.3.2, it is apparent that particle movement besides thermal diffusion may introduce additional intravoxel dephasing, which in turn can affect the signal attenuation in a DW-MRI experiment. It was briefly mentioned, that bulk motion during the application of the diffusion-sensitizing gradients can introduce a global phase, however, the magnitude of m_{xy} and therefore the signal intensity remains unaffected by such a global phase. In contrast, incoherent motion, e.g. particles moving independently of one another in different directions inside a given voxel, may result in a distribution of phases and, accordingly, in an attenuation of the measured signal intensity. The thermal diffusion of water molecules constitutes such a form of incoherent motion and in section 4.2 it was shown, that the attenuation of the measured signal intensity due to free diffusion is a factor of the exponential form e^{-bD}, with the diffusion coefficient D. Another source of incoherent motion in tissue is capillary perfusion: the water molecules in blood are flowing through randomly oriented capillaries at varying speeds in different directions. Depending on the duration of the diffusion experiment and the diffusion gradient profile, this type of motion may result in a distribution of phases as well and therefore causes additional signal attenuation. This led to the formulation of the intravoxel incoherent motion (IVIM) model by Le Bihan et al.[42] in 1988, where the signal $S(b)$ as a function of the b-value is expressed in terms of two compartments

$$S(b) = S_0\left(f \cdot e^{-bD} \cdot F[\boldsymbol{x}(t), \boldsymbol{g}(t)] + (1-f) \cdot e^{-bD}\right). \tag{4.23}$$

The compartment with signal fraction $(1-f)$ is thereby only subject to thermal diffusion, while the compartment with signal fraction f experiences additional signal attenuation through further incoherent motion, specifically capillary perfusion, summarized in the factor $F[\boldsymbol{x}(t), \boldsymbol{g}(t)]$. The attenuation factor $F = F[\boldsymbol{x}(t), \boldsymbol{g}(t)]$ is a functional of (all) the particles' motion paths $\boldsymbol{x}(t)$ and the magnetic field gradient $\boldsymbol{g}(t) = \boldsymbol{g} \cdot a(t)$ with temporally varying amplitude $a(t)$ and (in the context of this thesis) constant gradient direction $\boldsymbol{g}$. In eq. (4.23) it was further assumed that both

compartments are governed by the same thermal diffusion coefficient D. Accordingly, the signal fraction f can be understood as the signal fraction attributed to blood in a given voxel. Accounting for the relaxation times of the two compartments as well as the sequence parameters TE and TR, f can further be translated to the actual blood volume in the tissue[43].

As has been stated by Le Bihan et al.[42], the manifestation of the factor F is dependent on the characteristics of the capillary blood flow. The important characteristics of the blood flow are the flow velocity $\boldsymbol{v}$ and the time τ until a particle changes its movement direction with respect to the duration T of the diffusion-sensitizing period. For the sake of simplicity, the capillary bed is assumed to consist of segments that are interconnected, approximately straight and randomly oriented. Accordingly, a directional change occurs as a particle traverses from one segment to the next. In order to approximate F, further assumptions about the nature of the capillary blood flow within a voxel must be made:

- Each water molecules within the capillary network is moving with constant speed $v = |\boldsymbol{v}|$ during the diffusion experiment, where the movement direction is dictated by the orientation of the capillary segment in which the molecule currently resides.
- Tentatively, a common speed v for all particles is assumed, however, in subsection 4.4.3 it will be shown how the results can be generalized to accommodate for a statistical distribution of speeds $\rho(v)$.
- The capillary segments have a constant length l, consequently, the duration a particle resides within a segment is given by $\tau = l/v$.
- Capillary segments are numerous within a single voxel and are randomly oriented, so that an isotropic distribution of particle movement directions can be inferred.
- The movement directions of a particle before and after changing a capillary segment are uncorrelated.

In subsection 4.4.1 an approximation for the signal attenuation factor in the limiting case $\tau \ll T$ (i.e., many directional changes during the diffusion preparation), called the pseudo-diffusion limit, will be introduced. Complementary, in subsection 4.4.2**,** an analytic solution for F in the limiting case $\tau \gg T$ (i.e., the duration T of the diffusion experiment is much shorter than the time τ until a particle changes its movement direction), which translates to isotropic straight flow, will be derived[44]. This is followed by the introduction of normalized phase distributions based on the works of Wetscherek at al.[26,27] in subsection 4.4.3, allowing one to analyze the signal attenuation with an arbitrary number of directional changes during the application of the diffusion-sensitizing gradients.

4.4.1 Pseudo-Diffusion Limit

Originally introduced by Le Bihan et al.[42], the pseudo-diffusion limit in IVIM MRI implies that the particle displacement due to capillary flow is approximately Gaussian, similar to thermal diffusion. This requires that the particles experience many directional changes during the diffusion-sensitizing period, i.e. $\tau \ll T$. The signal attenuation factor can then be approximated by the exponential function $F = e^{-bD^*}$, with the pseudo-diffusion coefficient D^*. As will be shown in subsec-

tion 4.4.3, D^* is related to τ and particle speed v via $D^* = v^2\tau/6$. Applying the pseudo-diffusion limit to eq. (4.23) yields

$$S(b) = S_0\left((1-f)\cdot e^{-bD} + f\cdot e^{-b(D+D^*)}\right). \tag{4.24}$$

According to Le Bihan et al., at least four directional changes during the diffusion-sensitizing period are required for eq. (4.24) to be applicable[42]. For a more detailed discourse on the domain of validity of the biexponential model, the reader shall be referred to section 5.5. Remarkably, eq. (4.24) does only depend on the b-value, but not on the temporal profile of the diffusion gradients. Therefore, in the pseudo-diffusion limit, the measured signal decay is expected to be independent of the employed gradient scheme.

4.4.2 Straight Flow Limit

Next, the attenuation factor F in the limiting case of straight flow ($\tau \gg T$) will be discussed. The straight flow case implies that particles may flow in randomly oriented directions, however, they experience no acceleration or changes in their movement direction during the diffusion experiment.

Considering an ensemble of particles, F can be expressed in terms of the sum of transverse magnetization vectors with phase distribution $\rho(\phi)$ induced by the incoherent flow during the diffusion experiment:

$$F = \left|\langle e^{i\phi}\rangle\right| = \left|\int_{-\pi}^{\pi}\rho(\phi)e^{i\phi}\mathrm{d}\phi\right|. \tag{4.25}$$

In order to estimate F, one must therefore derive the distribution of phases $\rho(\phi)$. Treated in a frame of reference rotating with ω_0, the phase accumulated by a single particle travelling along the path $\boldsymbol{x}(t)$ during T (duration of a diffusion experiment) is given by eq. (4.17) and partial integration leads to

$$\phi = \gamma\int_0^T \boldsymbol{x}(t)\cdot\boldsymbol{g}(t)\mathrm{d}t = -\gamma\int_0^T \boldsymbol{v}(t)\cdot\int_0^t \boldsymbol{g}(t')\mathrm{d}t'\mathrm{d}t. \tag{4.26}$$

Due to the rephasing condition $m_0 = \int_0^T \boldsymbol{g}(t)dt = 0$, which needs to be fulfilled to allow for unimpaired image formation, ϕ is independent of the individual particles' starting positions x_i.

As is evident from eq. (4.26), in an ensemble of particles moving uniformly during T, i.e. all particles are sharing the same relative path $\boldsymbol{x}(t)$ (bulk motion, rigid body motion), the accumulated phase will be equal for all particles. It can easily be appreciated that in this case, eq. (4.25) equates to 1 and therefore coherent motion of particles inside a given voxel does not introduce additional signal decay in diffusion-weighted images.

As an example of *in*coherent particle movement, we will consider the following simple case: In accordance with previously stated assumption, all particles inside a capillary network are moving with identical and constant speed v in isotropically distributed directions and the angle between a particle's movement direction and the axis of the applied diffusion gradient is further given by α.

The characteristic duration τ is assumed to be much longer than the duration of the diffusion experiment T, so that directional changes (changes between capillary segments) of particles can be neglected. Using integration by parts of $1 \cdot \int_0^t \boldsymbol{g}(t')\mathrm{d}t'$ and the rephasing condition from above, the acquired phase of a particle will be proportional to the cosine of α:

$$\phi = -\gamma \int_0^T \boldsymbol{v} \cdot \int_0^t \boldsymbol{g}(t')\mathrm{d}t'\mathrm{d}t = v \cdot \cos(\alpha) \cdot \gamma \int_0^T t \cdot g(t)\mathrm{d}t = v \cdot \cos(\alpha) \cdot m_1, \tag{4.27}$$

with the total first moment of the diffusion gradient profile $m_1 = \gamma \int_0^T t \cdot g(t)\mathrm{d}t$.

For 3D isotropically distributed velocity directions, the probability distribution of α is $\rho(\alpha) = \frac{1}{2}\sin\alpha$, with $0 \leq \alpha < \pi$. Substituting $u = \cos\alpha$, the integral in eq. (4.25) yields

$$F = \left|\frac{1}{2}\int_0^\pi \sin\alpha \; e^{im_1 v \cos\alpha}\mathrm{d}\alpha\right| = \left|\mathrm{sinc}(m_1 \cdot v)\right|. \tag{4.28}$$

For flow-compensated gradient profiles, the total m_1 is zero and F again equates to 1, leaving the signal of flow-compensated sequences insensitive to the aforementioned type of particle movement (constant speed, random direction). For non-flow-compensated gradient profiles, m_1 is non-zero and the signal decays sinc-modulated with increasing $m_1(b)$. In this case, the signal decay is therefore strongly dependent on the gradient scheme.

4.4.3 Normalized Phase Distributions

We will now consider a more general case, where particles are still moving at constant speeds, but are experiencing an arbitrary amount of directional changes during the diffusion-sensitizing period. For this purpose we follow a framework presented by Wetscherek et al.[26,27] making use of normalized phase distributions.

In DW-MRI experiments where the diffusion-sensitizing magnetic field gradient is fixed along a direction $\boldsymbol{e}_g$, $\boldsymbol{g}(t)$ can be expressed using a normalized temporal profile $h(t/T)$ by

$$\boldsymbol{g}(t) = gh\left(\frac{t}{T}\right)\boldsymbol{e}_g = gh(s)\boldsymbol{e}_g\,, \qquad 0 \leq s \leq 1, \tag{4.29}$$

with the maximum gradient amplitude g.

Using eq. (4.12), the maximum gradient amplitude is directly related to the b-value via substituting $s = t/T$ in the outer integral and $s' = t'/T$ in the squared inner integral:

$$b = \int_0^T \left[\gamma \int_0^t \boldsymbol{g}(t')\mathrm{d}t'\right]^2 \mathrm{d}t = \gamma^2 g^2 T^3 \int_0^1 m_0^2(s)\mathrm{d}s = a_h^2 \gamma^2 g^2 T^3, \tag{4.30}$$

with the accumulated 0^{th} gradient moment $m_0(s) = \int_0^s h(s')\mathrm{d}s'$ and $a_h := \sqrt{\int_0^1 m_0^2(s)\mathrm{d}s}$. The factor a_h thus relates the shape of the respective gradient profile to the b-value, i.e. a_h is a meas-

ure of a gradient profiles efficiency with regards to achieving a strong diffusion weighting.

Using eq. (4.30), $\boldsymbol{g}(t)$ can be expressed as

$$\boldsymbol{g}(t) = gh\left(\frac{t}{T}\right)\boldsymbol{e}_g = \frac{\sqrt{b}}{a_h \gamma T^{3/2}} h\left(\frac{t}{T}\right)\boldsymbol{e}_g. \tag{4.31}$$

Inserting eq. (4.31) into eq. (4.26) yields

$$\phi = \frac{-\sqrt{b}}{a_h T^{3/2}}\boldsymbol{e}_g \cdot \int_0^T \boldsymbol{v}(t) \int_0^t h\left(\frac{t'}{T}\right) \mathrm{d}t' \mathrm{d}t = \frac{\sqrt{b}}{a_h \sqrt{T}}\boldsymbol{e}_g \cdot \int_0^T \boldsymbol{v}(t)\, m_0\left(\frac{t}{T}\right) \mathrm{d}t. \tag{4.32}$$

To evaluate this integral, we now apply the assumptions made in our particle movement model:

- Each particle moves with constant speed $v = |\boldsymbol{v}(t)|$
- Each particle's movement direction $\boldsymbol{e}_v(t)$ changes randomly after a constant time val τ
- The first directional change of a given particle occurs randomized in time at $t_1 = \tau \cdot r$, with $r \in U(0,1)$, where $U(0,1)$ is the uniform random distribution between 0 and 1 (excluding 0).

Using this model, the integral in eq. (4.32) can be split in $M = \lceil T/\tau + 1 - r \rceil$ intervals of constant movement, with the ceiling function $\lceil \cdots \rceil$. The k^{th} directional change is therefore only dependent on r and τ and occurs at $t_k = (r + k - 1)\tau$. We further define that the 0^{th} directional change occurs at $t_0 = 0$ and the last at $t_M = T$. The current movement segment is given by $k(t) = \lfloor t/\tau - r + 1 \rfloor$, with the floor function $\lfloor \cdots \rfloor$ and starting with $k = 0$ for the initial segment (segment before the 1^{st} directional change occurs). A particles velocity at the time t in the k^{th} segment is then given by $\boldsymbol{v}(t) = v \cdot \boldsymbol{e}_{k(t)}$, with the movement direction $\boldsymbol{e}_k$ in the k^{th} segment.

Applying this mode, eq. (4.32) transforms to

$$\begin{aligned} \phi_h(b, v, T, \tau, r) &= \frac{v\sqrt{b}}{a_h \sqrt{T}} \sum_{k=0}^{M-1} \boldsymbol{e_g} \cdot \boldsymbol{e_k} \int_{t_k}^{t_{k+1}} m_0\left(\frac{t}{T}\right) \mathrm{d}t \\ &= \frac{v\sqrt{bT}}{a_h} \sum_{k=0}^{M-1} \boldsymbol{e_g} \cdot \boldsymbol{e_k} \int_{s_k}^{s_{k+1}} m_0(s) \mathrm{d}s, \end{aligned} \tag{4.33}$$

where again, the normalized times $s = t/T$ and $s_k = t_k/T$ were used.

It is now possible to rewrite eq. (4.33) using a normalized phase ϑ_h, which only depends on the temporal gradient profile $h(s)$, r and the average (i.e., non-integer) number of directional changes $M = T/\tau$, using the dimensionless product $v\sqrt{bT}$ to define:

$$\phi_h(b, v, T, \tau, r) = v\sqrt{bT}\, \vartheta_h(M, r). \tag{4.34}$$

Thus, the normalized phases are given by

$$\vartheta_h(M,r) = \frac{1}{a_h}\sum_{k=0}^{N-1} \boldsymbol{e}_g \cdot \boldsymbol{e}_k \int_{s_k}^{s_{k+1}} m_0(s)\mathrm{d}s. \tag{4.35}$$

The problem of determining the signal attenuation factor F is therefore reduced to calculating the distribution of normalized phases $\rho_{\vartheta_h}(\vartheta, M)$ for a given gradient scheme $h(s)$ and average number of directional changes M. The distribution ρ_{ϕ_h} of the original phase ϕ_h is then given by

$$\rho_{\phi_h}(\phi, M) = \rho_{\vartheta_h}\left(\frac{\phi}{v\sqrt{bT}}, M\right) \cdot \frac{1}{v\sqrt{bT}}, \tag{4.36}$$

and the signal attenuation from eq. (4.25) is

$$F_h(b,v,T,\tau) = \left|\int_{-\infty}^{\infty} \rho_{\phi_h}\left(\phi, \frac{T}{\tau}\right) e^{i\phi}\mathrm{d}\phi\right| = \left|\int_{-\infty}^{\infty} \rho_{\vartheta_h}\left(\vartheta, \frac{T}{\tau}\right) e^{iv\sqrt{bT}\vartheta}\mathrm{d}\vartheta\right|. \tag{4.37}$$

Using this expression, it is possible to calculate the normalized phase distributions for a given $h(s)$ and M only once and then scale according to the sequence parameters b and T and to the particle velocity v to determine the respective attenuation factor F.

In the following it will be shown how the distribution ρ_{ϑ_h} for a given $h(s)$ and M can be evaluated by numerical simulation.

For a particle ensemble with isotropic distribution of movement directions, the statistical distribution of angles $\theta \in (0, \pi)$ between the diffusion gradient and the particle paths is given by $\rho(\theta) = \frac{1}{2}\sin\theta$. With $u_k := \boldsymbol{e}_g \cdot \boldsymbol{e}_k = \cos\theta_k$, the distribution $\rho(u_k)$ is given by

$$\rho(u_k) = \rho\big(\theta(u_k)\big) \cdot \left|\frac{d\theta}{du_k}\right| = \frac{\sin(\cos^{-1}(u_k))}{2} \cdot \frac{1}{\sqrt{1-{u_k}^2}} = \frac{1}{2}. \tag{4.38}$$

Accordingly, $u_k \in U(-1,1)$ is uniformly distributed between –1 and 1 and the product $\boldsymbol{e}_g \cdot \boldsymbol{e}_k$ in eq. (4.35) can be replaced by randomly drawn u_k for the purpose of numerical simulation. Furthermore, the integral in eq. (4.35) can be regarded as a weighting factor of the particle movement in the k^{th} segment. Following this idea, we can introduce the weightings c_h

$$c_h(r+k, M) := \frac{1}{a_h}\int_{s_k}^{s_{k+1}} m_0(s)\mathrm{d}s = \frac{1}{a_h}\int_{\min\left(1,\frac{k+r}{M}\right)}^{\min\left(1,\max\left(0,\frac{k+r-1}{M}\right)\right)} m_0(s)\mathrm{d}s, \tag{4.39}$$

and insertion in eq. (4.35) finally yields

$$\vartheta_h(M,r) = \sum_{k=0}^{\lceil M\rceil} u_k c_h(r+k, M). \tag{4.40}$$

Eq. (4.40) can then be used to generate the normalized phase distributions by performing Monte Carlo experiments for a large number of particles: tuples of random variables $(r, u_0, \dots, u_{\lfloor M \rfloor})$ are generated for each particle, allowing one to obtain a histogram of the resulting phases ϑ_h.

The phase-distribution framework can also be used to deduce the attenuation factor F in the pseudo-diffusion limit (large M). The normalized phase ϑ_h is a weighted sum of many uniformly distributed random variables u_k with zero mean and standard deviation $\sigma_k = 1/\sqrt{3}$. Therefore, the central limit theorem applies[45] and ρ_{ϑ_h} can be approximated as Gaussian with zero mean and standard deviation $\sigma = \sigma_k/\sqrt{M} = 1/\sqrt{3M}$ for large M:

$$\rho_{\vartheta_h}(\vartheta, M) \approx \sqrt{\frac{3M}{2\pi}} \cdot e^{-\frac{3M}{2}\vartheta^2} \text{ for } M \gg 1. \tag{4.41}$$

Applying the Gaussian phase approximation to eq. (4.25), F is simply the Fourier transform of a Gaussian, given by $G(\omega) = e^{-\omega^2\sigma^2/2}$, at the coordinate $\omega = v\sqrt{bT}$:

$$F_h(b, v, T, \tau) = \left| \int_{-\infty}^{\infty} \rho_{\vartheta_h}\left(\vartheta, \frac{T}{\tau}\right) e^{iv\sqrt{bT}\vartheta} \mathrm{d}\vartheta \right| \approx e^{-\frac{bTv^2}{6M}} = e^{-\frac{bv^2\tau}{6}} = e^{-bD^*}. \tag{4.42}$$

In the last step, the relationship $D^* = v^2\tau/6$ was established. Thus, in the case of large M, the phase-distribution framework results in an exponentially decaying F as a function of the applied b-value as well (compare to subsection 4.4.1).

The phase distributions generated by evaluating eq. (4.40) for a large number of particles are valid only for the particular values of M used for the respective simulation. It can be shown that the exact phase distribution for any $M < 1$ is given by a linear interpolation of $\rho_{\vartheta_h}(\vartheta, 0)$ and $\rho_{\vartheta_h}(\vartheta, 1)$[26]:

$$\rho_{\vartheta_h}(\vartheta, M) = (1 - M)\rho_{\vartheta_h}(\vartheta, 0) + M\rho_{\vartheta_h}(\vartheta, 1), \quad 0 < M < 1. \tag{4.43}$$

By sampling a fine grid of N_M exponentially spaced $M_k = \exp(k/N_M \cdot \log(M_{max})) > 1$, with $k = (1, 2, \dots, N_M)$, close approximations of the phase distributions for arbitrary (non-integer) M can again be obtained by linear interpolation.

General Distributions of Particle Speeds

So far, only ensembles of particles with a common speed v and, therefore, a common M were considered, i.e. the (implied) distribution of particle speeds was considered to follow a delta distribution. It is possible to calculate normalized phase distributions $\rho'_{\vartheta_h}(\vartheta, M)$ for arbitrary speed distributions $\rho(v), v \geq 0$ with mean $\langle v \rangle$ by introducing the distribution of (dimensionless) relative speeds $v_{rel} = v/\langle v \rangle$

$$\rho_{rel}(v_{rel}) = \langle v \rangle \, \rho(\langle v \rangle v_{rel}) \, . \tag{4.44}$$

The distribution of relative speeds $\rho_{rel}(v_{rel})$ therefore has the same shape as $\rho(v)$, yet is distribut-

ed around the mean value 1. The distribution of normalized phases $\rho_{\vartheta_h}(\vartheta, M)$ is implicitly dependent on the relative speeds since the width (maximum obtainable phase) as well as the average number of directional changes are linearly proportional to the respective relative speed v_{rel}. This can be accommodated for by adjusting the distribution of normalized phases for the relative speeds as

$$\rho_{v_{rel}}(\vartheta, M) = \frac{\rho_{\vartheta_h}(\vartheta / v_{rel}, v_{rel} M)}{v_{rel}}. \tag{4.45}$$

Finally, $\rho'_{\vartheta_h}(\vartheta, M)$ can be calculated by integrating the speed-adjusted phase distributions $\rho_{v_{rel}}(\vartheta, M)$ multiplied by the distribution of relative speeds $\rho(v_{rel})$ with respect to v_{rel}:

$$\rho'_{\vartheta_h}(\vartheta, M) = \int_0^\infty \rho(v_{rel}) \cdot \rho_{v_{rel}}(\vartheta, M) \mathrm{d}v_{rel}. \tag{4.46}$$

Replacing $\rho_{\vartheta_h}(\vartheta, M)$ in eq. (4.37) by $\rho'_{\vartheta_h}(\vartheta, M)$, the speed v corresponds to the mean $\langle v \rangle$ of the respective speed distribution $\rho(v)$.

A particle ensemble with common speed translates to delta-distributed speed, which, as is easily verified using eq. (4.44)-(4.46), results in $\rho_{\vartheta_h}(\vartheta, M) = \rho'_{\vartheta_h}(\vartheta, M)$. In section 5.1 suitable relative speed distributions $\rho(v_{rel})$ for the constructed capillary phantom (chapter 6) will be introduced.

5 Simulations and Theoretical Results

In this chapter, specifics regarding the generation of the normalized phase distributions and the analysis of MRI data are given, followed by precursory results based on simulations.

To properly model the spin dephasing induced by capillary flow, an approximation of the underlying particle speed distribution in the investigated object must be found. In chapter 6, the construction of a perfusable capillary phantom will be described. Based on information gained by characterizing the capillary phantom via optical microscopy (section 6.2) and previously published research in the field of fracture networks, a capillary network speed distribution $\rho_{\mathrm{CN}}(v)$ is deduced in section 5.1. Section 5.2 discusses the generation of the gradient profile respective phase distributions and prospects the emerging signal decay for different flow scenarios. Subsequently, section 5.3 details the model fitting and error estimation method. In section 5.4, a relationship between the diffusion duration experiments and the parameter estimation accuracy is established, serving as a basis for the design of the experiments in chapter 7. Finally, utilizing the generated phase distributions, signal decay curves for different flow-scenarios were simulated and analyzed in section 5.5 to assess the adequacy of the biexponential IVIM model and to facilitate the interpretation of the results in chapter 7.

5.1 Particle Speed Distribution

Section 4.4 was concluded by linking the distribution of normalized phases $\rho_{\vartheta_h}(\vartheta, M)$ with an arbitrary particle speed distribution $\rho(v)$. Having an adequate approximation of the statistical speed distribution of the flowing particles is crucial to facilitate an accurate model fit to the measured data and generate meaningful parameter estimates, as will become apparent in this chapter. In this section, a statistical distribution of particle speeds for the constructed capillary phantom will be motivated based on two considerations: Subsection 5.1.1 will cover the particle speed distribution inside a single capillary segment, while in subsection 5.1.2 the distribution of capillary-averaged speeds is discussed. The conjunction of those two considerations leads to the overall particle speed distribution $\rho_{\mathrm{CN}}(v)$.

5.1.1 Laminar Flow

As a first step to approximate the velocity distribution inside the capillary network, it is necessary to determine if fluid flow inside a single segment can be described as turbulent or laminar. The former manifests itself in chaotic motion and strong fluctuations in the particle velocities, while the latter is characterized by streamlined and ordered motion. This distinction can be made by calculating the ratio of inertial forces to viscous forces of the fluid called the Reynolds number Re[46]:

$$Re = \frac{\bar{v}D}{\nu} = \frac{\rho \bar{v} D}{\mu}, \tag{5.1}$$

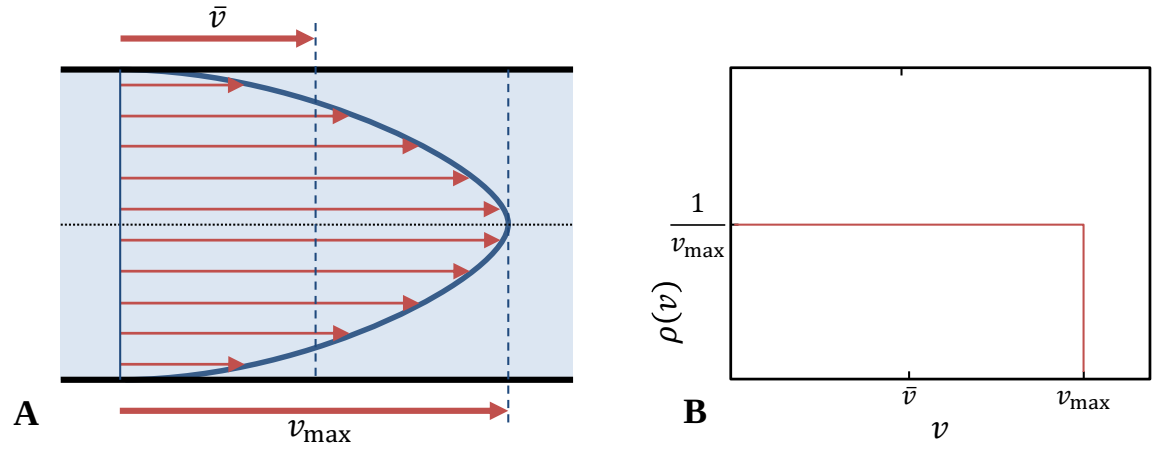

Figure 5.1: Illustration of fully developed laminar flow profile in a cylindrical capillary (panel A) and the corresponding uniform speed distribution $\rho(v)$ (panel B). The average velocity $\bar{v}$ through a cross section is given by the half of the maximum particle velocity: $\bar{v} = v_{max}/2$.

with the average particle speed $\bar{v}$, the characteristic length of the confining geometry D, and the kinematic viscosity $\nu = \mu/\rho$. Fluid flow is laminar for $Re \leq 2300$ under most practical conditions[46]. If we assume the confining geometry to be cylindrical tubes with a diameter of $D = 30\ \mu m$ (maximum diameter measured using optical microscopy in section 6.2) and the flowing liquid to be the NaCl solution determined in section 6.3 at room temperature ($\nu \approx 1.33 \times 10^{-6}\ m^2/s$ according to Kestin et al.[47]), eq. (5.1) dictates that the flow can be expected to be laminar for $\bar{v} \leq 57\ m/s$. To achieve flow velocities of that magnitude inside the capillary system would require exorbitant pumping pressure, which would most likely result in the destruction of the phantom. As will be shown in chapter 7 the determined average particle speed using the data from the flow-dependent DW-MRI experiments are in the order of $10^{-3}\ m/s$. It is therefore reasonable to assume that flow is laminar inside the capillaries.

Laminar flow is characterized by a constant axial velocity of each fluid particle along a streamline, absent of motion in the radial direction (Figure 5.1). The speed profile is a parabolic function of the radial position r and can be written as

$$v(r) = 2\bar{v}\left(1 - \frac{r^2}{(D/2)^2}\right). \tag{5.2}$$

Integration over an entire cross section yields for the distribution $\rho_{lam,\bar{v}}(v)$ of (non-negative) speeds

$$\rho_{lam,\bar{v}}(v) = \frac{\Theta(2\bar{v} - v)}{2\bar{v}}, \tag{5.3}$$

with the Heaviside function Θ. The particle speeds v are therefore uniformly distributed between 0 and $v_{max} = 2\bar{v}$.

5.1.2 Speed Distribution in Capillary Networks

The speed distribution in eq. (5.3) was derived for a single capillary, but will also be valid for a network of capillary segments assuming the average speed $\bar{v}$ is common across different capillary segments. As a more general approach, one may assume that different capillaries will yield varying average speeds, due to variations in the diameters, lengths and pressure differences. The overall statistical speed distribution $\rho(v)$, taking the distribution of average speeds $\rho(\bar{v})$ as well as the capillary respective speed distribution $\rho_{\mathrm{lam},\bar{v}}(v)$ due to laminar flow into consideration, is then given by the convolution

$$\rho(v) = \int_0^\infty \rho(\bar{v}) \cdot \rho_{\mathrm{lam},\bar{v}}(v)\mathrm{d}\bar{v} = \int_0^\infty \rho(\bar{v}) \cdot \frac{\Theta(2\bar{v} - v)}{2\bar{v}}\mathrm{d}\bar{v} = \int_{v/2}^\infty \frac{\rho(\bar{v})}{2\bar{v}}\mathrm{d}\bar{v}, \tag{5.4}$$

where the Heaviside function $\Theta(2\bar{v} - v)$ was eliminated by adjusting the integral bounds.

As will become apparent in this chapter, a reasonable approximation of the underlying distribution of average speeds $\rho(\bar{v})$ is crucial for the accurate estimation of the flow parameters. While it would in theory be possible to formulate an inverse problem using the data obtained in chapter 7 to fit the underlying speed distribution, the ill-posedness of this problem would require extensive regularization (aside from an exorbitant computing power), limiting the meaningfulness of the generated result. One way to obtain an approximation of the speed distribution is to perform fluid flow simulations using an exact digital 3D model of the capillary phantom. Unfortunately, this approach entails significant difficulties. Firstly, due to the very small details of the capillary structure in the micrometer range, accurately capturing the entire phantom poses a considerable technical challenge. While advanced X-ray microtomography scanners are able to deliver resolutions at 1 µm isotropic resolution, the phantom dimensions do not conform to the required maximum sample size. As the sample size and with it the field of view increases, the achievable resolution decreases. Consequentially, the phantom would have need to be cut up into smaller sections to be scanned separately and pieced together subsequently, rendering the phantom unusable for any subsequent MRI measurements. Furthermore, the accurate simulation of fluid flow in complex geometries is far from straight forward and topic of current research.

Hence, a more practical approach was taken by applying results from related research in the field of particle transport in fracture networks. Particle transport through fractured rock is an important issue in subsurface hydrology, particular in regards to the geological disposal of nuclear waste[48]. In particle transport, one is primarily interested in the Lagrangian flow velocities, tracking individual particles as they move through space and time[46]. In the Lagrangian picture, the particles are labeled by a time-independent vector $\boldsymbol{x_0}$ (e.g., their initial position at $t = 0$), and the flow is described by the function

$$\mathbf{X}(\mathbf{x_0}, t), \tag{5.5}$$

giving the position of a particle at time t. This is contrasted by the Eulerian picture, where one is interested in the velocity field $\mathbf{u}(\mathbf{x}, t)$ within a fixed observation frame.

The Lagrangian and the Eulerian descriptions of flow are related by[49]

$$\mathbf{u}(\mathbf{X}(\mathbf{x_0}, t), t) = \frac{\partial \mathbf{X}}{\partial t}(\mathbf{x_0}, t). \tag{5.6}$$

The analysis of flow-induced spin dephasing in DW-MRI experiments adheres to the Eulerian picture, since the observation frame is fixed by the imaging parameters. Fortunately, the analysis of the Lagrangian velocities in particle transport is usually based on the initial simulation of Eulerian velocity fields.

Particle transport analyses by Painter et al.[48] as well as by Frampton and Cvetkovic[50,51] were based on a simulated three-dimensional fracture network with uniformly oriented fractures of log-normally distributed lengths and apertures (length and apertures uncorrelated). As will be shown in section 6.2, the distribution of the capillary lengths inside the phantom, determined using optical microscopy, is well approximated by a log-normal distribution. Assuming cylindrical capillaries, the distribution of apertures in the phantom is given by

$$\rho(a) = \pi\rho\left(\left(\frac{d}{2}\right)^2\right), \tag{5.7}$$

with the measured diameters d. Fitting a log-normal distribution to $\rho(a)$ and subsequently performing a Kolmogorov-Smirnov test to compare the actual and fitted distributions yields a statistic of $D_n = 0.022$ and $p = 0.367$. The strong similarity of the measured capillary and aperture distributions to log-normal distributions serves as reasonable basis for the applicability of the results by the aforementioned studies. Their findings indicate, that the distribution of the "segment slowness" $\rho(\beta) = \rho(1/\bar{v})$, with the particle speed $\bar{v}$, is closely approximated by a Pareto power-law distribution[52]:

$$\rho(\beta) = \alpha{\beta_{\min}}^{\alpha} \cdot \Theta(\beta - \beta_{\min}) \cdot \beta^{-\alpha-1}, \tag{5.8}$$

with the scale parameter $\beta_{\min} > 0$ and the shape parameter $\alpha > 0$. The notation $\bar{v}$ was used since in the works of Frampton and Cvetkovic[50,51] the particle flow inside the capillaries was approximated as plug flow and $\bar{v} = 1/\beta$ can therefore be considered as the average speed within a capillary with regard to a laminar flow profile (see previous section). The distribution of the average particle speeds as a function of v, $\rho(\bar{v})$, can be obtained via

$$\rho(\bar{v}) = \rho\big(\beta(\bar{v})\big) \cdot \left|\frac{d\beta}{d\bar{v}}\right|. \tag{5.9}$$

By substituting $\beta_{\min} = 1/\bar{v}_{\max}$ follows

$$\rho\big(\beta(\bar{v})\big) = \frac{\alpha}{\bar{v}_{\max}^{\alpha}} \cdot \Theta\left(\frac{1}{\bar{v}} - \frac{1}{\bar{v}_{\max}}\right) \cdot \bar{v}^{\alpha+1} = \frac{\alpha}{\bar{v}_{\max}^{\alpha}} \cdot \Theta(\bar{v}_{\max} - \bar{v}) \cdot \bar{v}^{\alpha+1} \tag{5.10}$$

and

$$\beta = \frac{1}{\bar{v}} \rightarrow \frac{\mathrm{d}\beta}{\mathrm{d}\bar{v}} = \frac{-1}{\bar{v}^2}. \tag{5.11}$$

Insertion into (5.9) yields

$$\rho(\bar{v}) = \frac{a}{\bar{v}_{\max}^{\alpha}} \cdot \Theta(\bar{v}_{\max} - \bar{v}) \cdot \bar{v}^{\alpha-1}. \tag{5.12}$$

A comparison of $\rho(\bar{v})$ for varying α is shown in Figure 5.2 A. Depending on α, the PDF is either positively skewed ($\alpha < 1$), uniform ($\alpha = 1$) or negatively skewed ($\alpha > 1$).

The maximum particle speed $\bar{v}_{\max}$ can be related to the average particle speed by calculating the expectation value $\mathrm{E}[\bar{v}] = \langle \bar{v} \rangle$

$$\langle \bar{v} \rangle = \int_0^{\infty} \bar{v} \cdot \rho(\bar{v}) \mathrm{d}v = \frac{\alpha}{\bar{v}_{\max}^{\alpha}} \int_0^{\bar{v}_{\max}} \bar{v}^{\alpha} \mathrm{d}\bar{v} = \frac{\alpha}{\alpha + 1} \bar{v}_{\max}. \tag{5.13}$$

Hence, eq. (5.12) can be expressed as

$$\rho(\bar{v}) = \alpha \left(\frac{\alpha}{\langle \bar{v} \rangle (\alpha + 1)} \right)^{\alpha} \Theta\left(\frac{\langle \bar{v} \rangle (\alpha + 1)}{\alpha} - \bar{v} \right) \bar{v}^{\alpha-1}, \tag{5.14}$$

which simplifies for $\alpha = 1$ to the uniform distribution

$$\rho(\bar{v},\ \alpha = 1) = \frac{1}{2\langle \bar{v} \rangle} \Theta(2\langle \bar{v} \rangle - \bar{v}). \tag{5.15}$$

Taking into account the laminar flow profile inside the capillaries, eq. (5.4) must be applied to eq. (5.14) and eq. (5.15) to obtain the overall speed distribution which is then finally given by

$$\rho(v) = \begin{cases} \dfrac{\alpha^2 \left(1 - \left(\dfrac{\alpha v}{2\langle v \rangle (\alpha + 1)} \right)^{\alpha-1} \right)}{2\langle v \rangle (\alpha + 1)(\alpha - 1)} \cdot \Theta\left(\dfrac{\langle v \rangle (\alpha + 1)}{\alpha} - \dfrac{v}{2} \right) & \alpha \neq 1 \\ \dfrac{\ln(2\langle v \rangle) - \ln\left(\dfrac{v}{2}\right)}{4\langle v \rangle} & \alpha = 1 \end{cases} \tag{5.16}$$

Figure 5.2 B illustrates the resulting particle speed distributions for varying α values. After considering the laminar flow profile, the distributions are positively skewed regardless of the value of α. However, as α decreases the distributions display a more pronounced L-shape with an elongated tail towards higher speeds as the maximum speed is given by $v_{\max} = 2\langle v \rangle (\alpha + 1)/\alpha$. The appropriate value of the shape parameter α is dictated by the frame of reference, i.e. Eulerian or Lagrangian picture[46]. A phenomenon called preferential flow[53] describes how the majority of particles follow the fastest flowing path. Consequently, in the Lagrangian frame of reference, where one is following individual particles, α is larger than 1, resulting in a $\rho(\bar{v})$ that is negatively skewed towards faster particle speeds (see Figure 5.2).

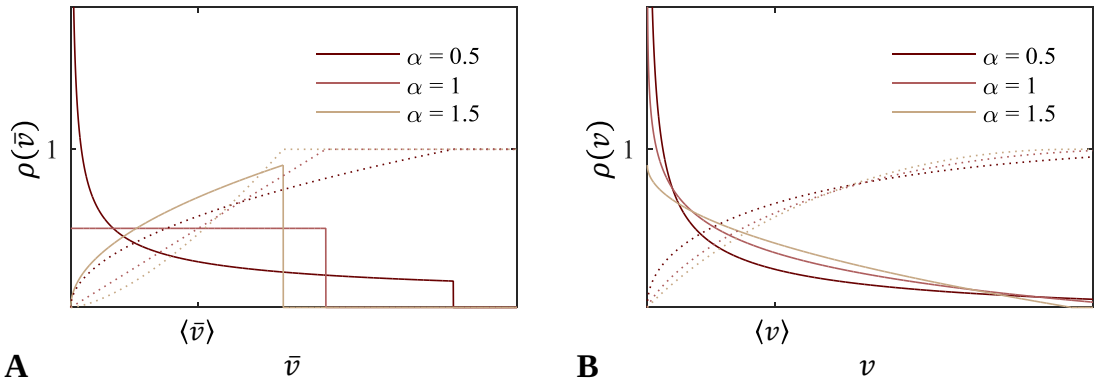

Figure 5.2: Comparison of the PDFs (solid lines) and CDFs (dotted lines) of the average particle speeds within capillaries $\rho(\bar{v})$ (eq. (5.12)) in panel **A** and the overall particle speeds (including also the laminar flow profiles) $\rho(v)$ (eq. (5.16)) in panel **B** for varying shape parameters α. The PDFs were normalized to yield an equal expectation value $\mathrm{E}[\bar{v}] = \langle\bar{v}\rangle$ and $\mathrm{E}[v] = \langle v\rangle$, respectively.

In the Eulerian frame of reference, where one is observing a fixed location in space, the slow velocities dominate and can become arbitrarily small. In this case, the shape parameter α is smaller than 1 and $\rho(\bar{v})$ is positively skewed.

During the course of the analysis of the experimental data, the determination of the optimum value for α based on the model fits has not proven to be expedient (see chapter 7). However, it will become apparent that a positively skewed speed distribution can indeed be deduced clearly from the measured signal intensities. It will be shown that using a value of $\alpha = 0.5$ leads to a high goodness of fit and to physically meaningful parameter estimates. The distribution derived in eq. (5.16) with $\alpha = 0.5$ will in the following simply referred to as the capillary network speed distribution $\rho_{\mathrm{CN}}(v)$ and is given by

$$\rho_{\mathrm{CN}}(v) = \frac{1}{6\langle v\rangle}\left(\frac{\sqrt{6\langle v\rangle}}{\sqrt{v}} - 1\right) \cdot \Theta(6\langle v\rangle - v). \tag{5.17}$$

Thus, $\rho_{\mathrm{CN}}(v)$ has essentially the shape of $f(x) = 1/\sqrt{x}$ but is scaled and shifted along the y-axis such that the zero occurs at $v_{\max} = 6\langle v\rangle$.

5.2 Phase Distributions

In subsection 4.4.3, it was demonstrated that the normalized phase of a single particle acquired during a diffusion MRI experiment due to flow in randomly oriented capillaries can be expressed as

$$\vartheta_h(M, r) = \sum_{k=0}^{\lceil M\rceil} u_k c_h(r + k, M), \tag{5.18}$$

with random variables $(r, u_0, \ldots, u_{\lfloor M\rfloor})$, the number of directional changes M and the weighting of each movement segment c_h. Sampling a vast number of normalized phases allows one to approxi-

mate the underlying normalized phase distribution and finally to determine the respective signal attenuation factor F (optionally applying a particle speed distribution beforehand as in eq. (4.46)). The weightings c_h of the movement segments depend on the normalized profile $h(s)$ of the employed gradients. More specifically, the normalized 0^{th} gradient moment $m_0(s)$ as well as $a_h = \sqrt{\int_0^1 m_0^2(s)\mathrm{d}s}$ have to be determined.

The calculation of the normalized phase distributions for the gradient profiles employed in the diffusion experiments (chapter 7) is discussed in detail in subsection 5.2.1. Subsequently, the obtained phase distributions and the corresponding signal attenuation factors F is discussed in subsection 0 with a focus on the influence of M as well as the particle speed distributions.

5.2.1 Generating Normalized Phase Distributions

To obtain distributions of the normalized phases $\rho_{\vartheta_h}(\vartheta, M)$ according to eq. (5.18) using Monte Carlo simulations, $h(s)$, $m(s)$ and a_h have to be determined for each employed gradient scheme. First, the monopolar gradient scheme (Figure 5.3) will be discussed.

Due to technical limitations, the diffusion gradients cannot be employed arbitrarily fast. A short interval τ ($\sim$0.7 ms, depending on the maximum gradient amplitude) is required to ramp the gradients up and down, respectively, which is exaggeratedly depicted in the exact gradient profile in Figure 5.3. The interval between the start of the ramp-up and ramp-down is given by δ, while the interval between the start of each lobe, separated by the 180° inversion pulse, is given by Δ. To simplify the temporal gradient profile $h(s)$ for the calculation of the normalized phases, the gradient lobes were modelled as step functions. Hereby, the maximum gradient amplitude duration was increased by $\tau/2$ on each side to accommodate for the ramping-duration, before normalizing the temporal profile on the resulting total gradient scheme duration $\Delta + \delta$. Note that the 180° inversion pulse inverts the effective sign of subsequent gradients, which is ignored for the temporal gradient profile $h(s)$ in Figure 5.3, but is reflected in the following equation for $h(s)$ and the resulting 0^{th} gradient moment $m_0(s)$:

$$\text{monopolar:} \qquad h(s) = \begin{cases} 1 \\ 0 \\ -1 \end{cases}; \qquad m_0(s) = \begin{cases} s & 0 \le s < a \\ a & a \le s < b, \\ 1-s & b \le s < 1 \end{cases} \tag{5.19}$$

with

$$a = \frac{\delta}{\Delta + \delta};\ b = \frac{\Delta}{\Delta + \delta}. \tag{5.20}$$

For a_h follows with $\int_0^1 m_0^2(s)\mathrm{d}s = \int_0^a s^2\mathrm{d}s + \int_a^b a^2\mathrm{d}s + \int_b^1 (1-s)^2\mathrm{d}s$:

$$a_h = \sqrt{\int_0^1 m_0^2(s)\mathrm{d}s} = \sqrt{\frac{1}{3} - b + b^2 - \frac{b^3}{3} + a^2 b - \frac{2a^3}{3}} = \sqrt{\frac{\delta^2(3\Delta - \delta)}{3(\delta + \Delta)^3}}. \tag{5.21}$$

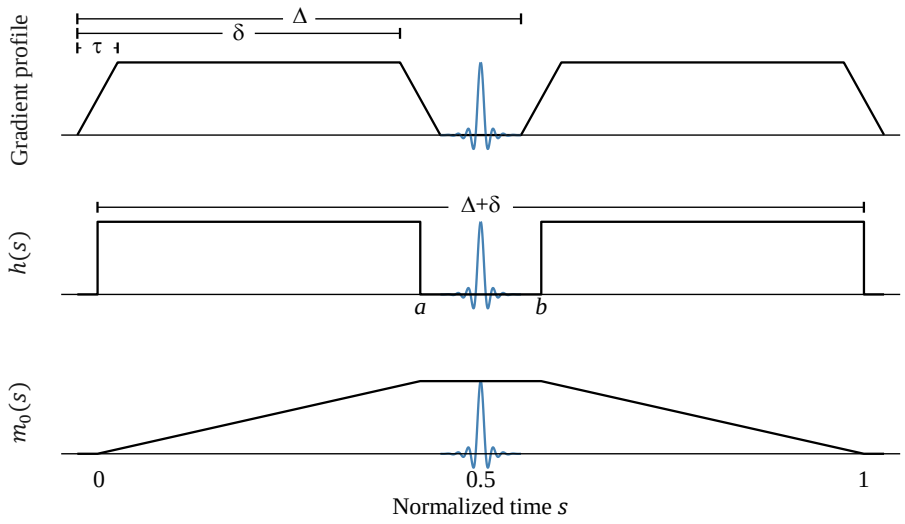

Figure 5.3: Exact gradient profile, simplified temporal gradient profile $h(s)$ and 0^{th} gradient moment $m_0(s)$ of the monopolar gradient scheme.

Considering the trapezoidal shape of $m_0(s)$, the integral in eq. (4.39) can be evaluated for arbitrary bounds $s_L < s_U$ using

$$\int_{s_L}^{s_U} m_0(s)ds = \frac{1}{2}\big({s_U}^2 - {s_L}^2 - max(0, s_U - a)\,(s_U - a) - max(0, s_U - b)\,(s_U - b) + max(0, s_L - a)\,(s_L - a) + max(0, s_L - b)\,(s_L - b)\big). \tag{5.22}$$

The here deduced equations are also valid to generate the phase distributions for STEAM pulse sequences using monopolar diffusion gradients. As discussed in subsection 4.3.2, STEAM pulse sequences allow for increased diffusion times while preserving acceptable SNR values by circumventing T2 relaxation effects. Instead of a 180° pulse, STEAM sequences employ two subsequent 90° pulses, separated by an adjustable time interval, which can be accommodated for in the above-introduced temporal gradient profile $h(s)$ for monopolar diffusion gradients by adjusting the value of Δ accordingly.

Next, the flow-compensated gradient scheme (Figure 5.4) will be treated in an equivalent manner. Again, the temporal gradient profile $h(s)$ was modelled as a step function, where the gradient ramp-duration τ was taken into account by extending the duration of the maximum gradient amplitudes. After normalization, $h(s)$ and $m(s)$ are given by

$$\text{flow-compensated:} \quad h(s) = \begin{cases} 1 \\ 0 \\ -1 \\ 0 \\ -1 \\ 0 \\ 1 \end{cases}; \quad m_0(s) = \begin{cases} s & 0 \le s < a \\ a & a \le s < b \\ c - s & b \le s < c \\ 0 & c \le s < d, \\ d - s & d \le s < e \\ -a & e \le s < f \\ s - 1 & f \le s < 1 \end{cases} \tag{5.23}$$

with

$$a = \frac{\delta - \tau}{2(\Delta + \delta)};\ b = \frac{\delta + \tau}{2(\Delta + \delta)};\ c = \frac{\delta}{\Delta + \delta};$$
$$d = \frac{\Delta}{\Delta + \delta};\ e = \frac{\delta + 2\Delta - \tau}{2(\Delta + \delta)};\ f = \frac{\delta + 2\Delta + \tau}{2(\Delta + \delta)}. \tag{5.24}$$

For a_h follows (by piecewise integration as before)

$$\begin{aligned} a_h &= \sqrt{\frac{1}{3} - \frac{2a^3}{3} + a^2 b + \frac{c^3}{3} - c^2 b + cb^2 - \frac{b^3}{3} + d^2 e - de^2 + \frac{e^3}{3} - \frac{d^3}{3} + a^2 f - a^2 e - \frac{f^3}{3} + f^2 - f} \\ &= \sqrt{\frac{1}{3} + \frac{4}{3}\frac{(\delta - \tau)^2(\delta + 2\tau) - 2(\Delta + \delta)^3}{8(\Delta + \delta)^3}} = \sqrt{\frac{(\delta - \tau)^2(\delta + 2\tau)}{6(\Delta + \delta)^3}}. \end{aligned} \tag{5.25}$$

Approaching the integral $\int_{s_L}^{s_U} m_0(s)ds$ for arbitrary bounds $s_L < s_U$ analogously as in the monopolar case leads to

$$\begin{aligned} \int_{s_L}^{s_U} m_0(s)ds = \frac{1}{2}\big(& {s_U}^2 - {s_L}^2 - max(0, s_U - a)\,(s_U - a) + max(0, s_L - a)\,(s_L - a) \\ & - max(0, s_U - b)\,(s_U - b) + max(0, s_L - b)\,(s_L - b) \\ & + max(0, s_U - c)\,(s_U - c) - max(0, s_L - c)\,(s_L - c) \\ & - max(0, s_U - d)\,(s_U - d) + max(0, s_L - d)\,(s_L - d) \\ & + max(0, s_U - e)\,(s_U - e) - max(0, s_L - e)\,(s_L - e) \\ & + max(0, s_U - f)\,(s_U - f) - max(0, s_L - f)\,(s_L - a)\big). \end{aligned} \tag{5.26}$$

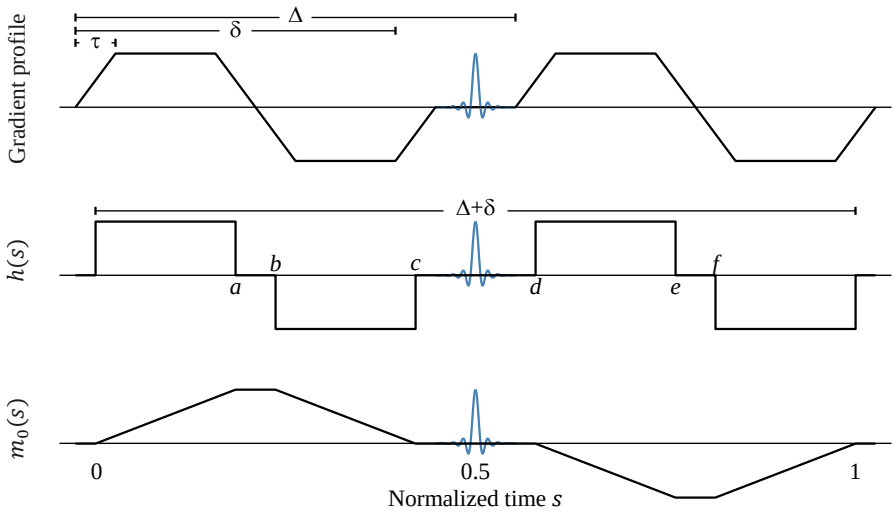

Figure 5.4: Exact gradient profile, simplified temporal gradient profile $h(s)$ and 0^{th} gradient moment $m_0(s)$ of the flow-compensated gradient scheme.

For the diffusion-weighted MRI experiments with applied flow through the phantom, four different sequences with varying gradient schemes and gradient timings were used as summarized in Table 5.1. The sequence ID is referring to the monopolar (MP) or flow-compensated (FC) gradient profiles followed by the leading edge separation between two gradient lobes, also referred to as diffusion time interval t_D. For the monopolar diffusion gradient profiles t_D corresponds to Δ, whereas for the flow-compensated profiles t_D equals to $(\delta + \tau)/2$.

Having deduced the above-mentioned expressions for $h(s)$, $m(s)$ and a_h, the Monte Carlo experiments to obtain the normalized phase distributions $\rho_{\vartheta_h}(\vartheta, M)$ were performed using Matlab (The MathWorks, Natick, Massachusetts, USA). For each gradient profile, the normalized phase distributions were generated for 256 logarithmically spaced values for the number of directional changes M ranging from 1 to 30 by simulating paths for 640,000,000 particles. As mentioned in subsection 4.4.3, $\rho_{\vartheta_h}(\vartheta, M < 1)$ is given by linear interpolation of $\rho_{\vartheta_h}(\vartheta, 0)$ and $\rho_{\vartheta_h}(\vartheta, 1)$, whereas $\rho_{\vartheta_h}(\vartheta, M > 30)$ can be approximated by a Gaussian distribution for all of the employed gradient profiles. Lastly, the normalized phase distributions for the different particle speed distributions were calculated according to eq. (5.4).

Table 5.1: Sequences with varying gradient schemes and gradient timings used for the diffusion-weighted MRI experiments with applied flow through the phantom.

ID	Gradient scheme	b-values[s/mm²]	Δ[ms]	δ[ms]	τ[ms]	a_h	TE[ms]
FC11	Flow-compensated	0-200	25.4	21.7	0.7	0.126	58
FC18	Flow-compensated	0-800	38.8	34.7	0.7	0.132	84
MP28	Monopolar	0-800	28.1	22.3	0.7	0.283	60
MP171	Monopolar (STEAM)	5-800	171.2	16.2	0.7	0.081	47

5.2.2 Signal Decay

The purpose of this section is to show how the generated normalized phase distributions and the resulting signal attenuation depend on the number of directional changes M as well as to illustrate the significance of applying a speed distribution other than a delta distribution.

Figure 5.5 shows the generated normalized phase distributions $\rho_{\vartheta_h}(\vartheta, M)$ as well as the resulting attenuation factors F for the gradient schemes with ID 'FC18' (flow-compensated gradients) and 'MP28' (monopolar gradients) when no further particle speed distribution was applied. Using a constant particle speed $v = 1\ \mathrm{mm/s}$, F is hereby plotted as a function of the diffusion weighting (b-value).

The flow-compensated gradients show no dephasing for $M = 0$, such that the factor F remains constant independent of the applied b-value. This is consistent with eq. (4.28) derived for the straight flow case. For $0 < M < 1$, F decreases with increasing b-value, however, in a non-exponential fashion and with a limit greater than zero. Eventually, as M is further increased, the phase distribution starts to approximate a Gaussian distribution. Accordingly, at large M the attenuation factor F decreases exponentially with increasing b-value.

The monopolar gradient on the other hand shows the fastest dephasing in the case of $M = 0$, as the normalized phases take on a uniform distribution. The associated attenuation factor decreases steeply with increasing b-value in a sinc-like fashion in accordance with eq. (4.28), creating local

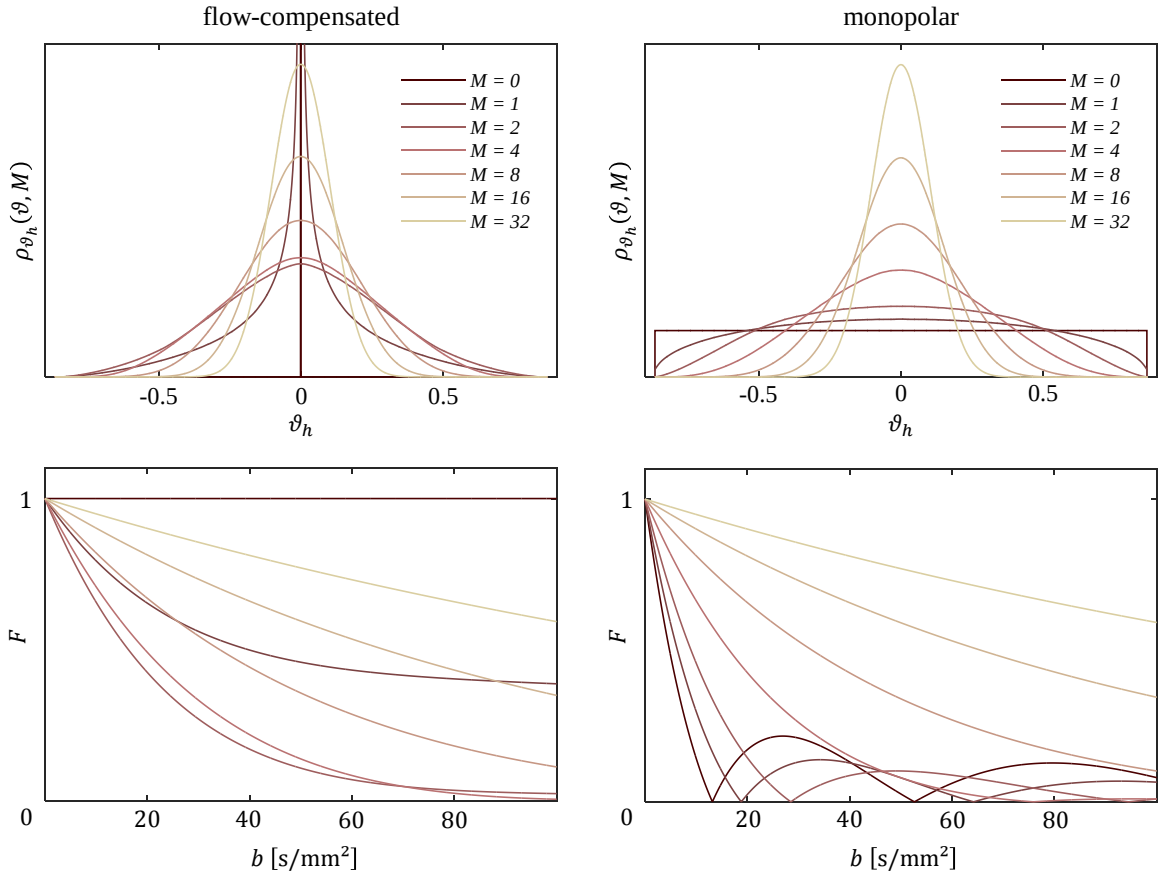

Figure 5.5: Generated normalized phase distributions $\rho_{\vartheta_h}(\vartheta, M)$ (top row) and the corresponding signal attenuation factors F (bottom row) using a delta-distributed particle speed with a constant particle speed $v = 1\ \mathrm{mm/s}$ for flow-compensated (left column) and monopolar (right column) gradients.

minima where particles completely dephase and local maxima where they partly rephase. As M is increased, the distribution of the normalized phases is passing over dome-shaped to eventually approximating Gaussian for large M as well. Simultaneously, the slope of F is decreasing, pushing the local minima to higher b-values until they disappear as the phase distribution becomes Gaussian. As can be inferred from Figure 5.5, for $M = 32$ the phase distributions for the two gradient profiles are virtually identical and the respective attenuation factors F both decrease exponentially with increasing b-value at the same rate. It is noteworthy that there are no results to be found in the literature demonstrating an unambiguous sinc-like signal decay in a diffusion-weighted MRI experiment where capillary perfusion was investigated. By applying an appropriate particle speed distribution (see section 5.1) this seemingly unphysiological behavior can be remedied for, as will be shown in the following paragraph.

Figure 5.6 shows the generated normalized phase distributions $\rho_{\vartheta_h}(\vartheta, M)$ and the resulting attenuation factors F when the speed distribution $\rho_{\mathrm{CN}}(v)$ determined in section 5.1 (which was derived from the Pareto power-law distribution with $\alpha = 0.5$) was applied, again with an average particle speed of $v = 1\ \mathrm{mm/s}$. For both the flow-compensated and the monopolar gradients, the

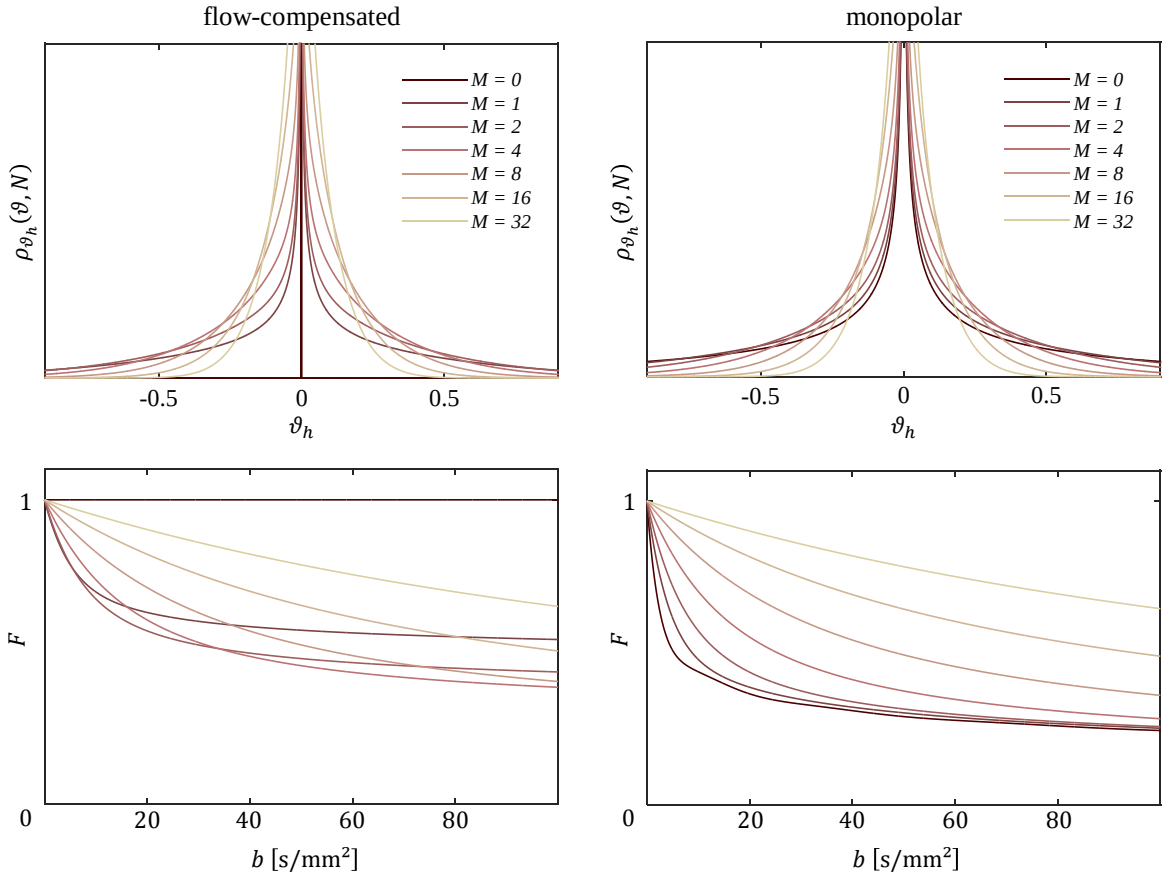

Figure 5.6: Generated normalized phase distributions $\rho_{\vartheta_h}(\vartheta, M)$ (top row) and the corresponding signal attenuation factors F (bottom row) using the speed distribution $\rho_{\mathrm{CN}}(v)$ determined in section 5.1 (derived from the Pareto power-law distribution with $\alpha = 0.5$) with an average particle speed $v = 1\,\mathrm{mm/s}$ for flow-compensated (left column) and monopolar (right column) gradients.

generated phase distributions appear asymptotic, however, all but the flow-compensated gradients with $0 \leq M < 1$ lead to a well-defined (i.e. finite) value for $\rho_{\vartheta_h}(0, M)$. Most noticeably, the local minima and maxima for the attenuation factor F in the monopolar case have disappeared, as the shape of the generated phase distributions does no longer facilitate a complete dephasing and subsequent rephasing of the spins as the b-value is increased. Again, for large M, the phase distributions and thus the decay shapes of F from the two gradient profiles appear alike. However, due to the wide distribution of particle speeds, the decay of F deviates from a true exponential decay even at large M, as will be discussed in section 5.5.

Another way of illustrating the differences in the signal attenuation factor F and therefore differences in the resulting signal intensities $S(b)$ between the monopolar and flow-compensated gradients is shown in Figure 5.7, where the maximum absolute slope of the attenuation factor, i.e. the slope at $b = 0$, $\lim_{b\to 0}\left|\frac{\partial F}{\partial b}\right|$, is plotted versus the number of directional changes M. At small values of M, the slopes differ vastly between gradient profiles, therefore a large deviation in the respective signal decay is to be expected. However, if the particles experience many directional

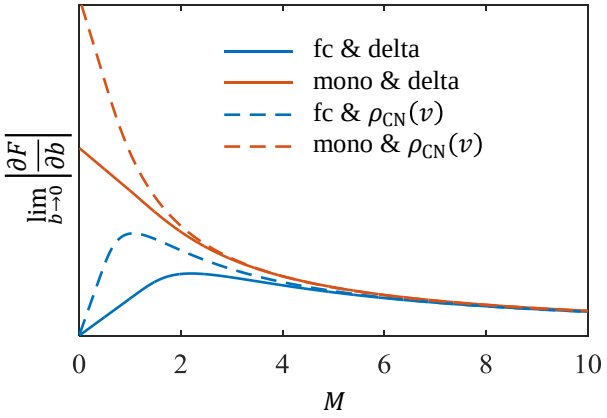

Figure 5.7: Maximum absolute slope of the attenuation factor $\lim_{b\to 0}\left|\frac{\partial F}{\partial b}\right|$ versus the number of directional changes M using different gradient profiles (blue: fc = flow-compensated; red: mono = monopolar) and particle speed distributions (solid: delta distribution; dashed: $\rho_{CN}(v)$).

changes M during the diffusion experiment ($M \gtrsim 6$), the maximum absolute slope becomes largely independent of the gradient profile and the particle speed distribution. It should be noted that while the maximum absolute slope of the attenuation factor is independent of the particle speed distribution at large M, this does not apply to the further decay of the attenuation factor (section 5.5).

5.3 Parameter Fitting and Error Estimation

The normalized phase distributions $\rho_{\vartheta_h}(\vartheta, M)$, as derived in subsection 5.2.1, enables one to formulate an optimization problem using simulated (section 5.4) or measured (chapter 7) data and the signal model given in eq. (4.23). The model is fitted to the data to obtain estimates for the model parameters. Specifically, these parameters are the unweighted signal intensity S_0, the thermal diffusion coefficient D, the fraction f of the signal coming from particles within perfused capillaries (as opposed to "static" particles outside the perfused capillaries), the average particle speed v due to flow in the capillaries and the characteristic duration τ a particle remains in a capillary segment on average. Note that if n different gradient profiles are considered within an experimental setup, n separate unweighted signal intensities S_0 as well as n effective (apparent) diffusion coefficients D_0 have to be fitted. Fitting separate diffusion coefficients is required since the matrix material of the constructed phantom restricts the Brownian motion of the water molecules (see chapter 6). The effect of this restriction on the measured signal decay is dependent on the respective gradient profile (see section 4.2 and 7.2) which has to be accounted for to facilitate an appropriate modelling of the measured data. The reasoning is trivial for S_0 as each measured signal decay has an independent y-axis intercept. The fraction f, the speed v as well as the duration τ are "shared" parameters, i.e. they are independent of the gradient scheme and are fitted with respect to all data.

The parameter fitting was done using the Matlab function *fminunc*, a nonlinear programming solver which finds the minimum of an unconstrained multivariable function using the quasi-newton algorithm[54]. The multivariable function is defined as the sum of the squared residuals RSS.

Using k to index the gradient profiles and g to index the respective b-values, the RSS is given by:

$$RSS = \sum_{i=1}^{N} r_i^2 = \sum_{k=1}^{n} \sum_{g=1}^{m_k} \left(S_{k,g} - S_k\left(b_{k,g}, S_{0_k}, D_k, f, v, \tau\right)\right)^2, \tag{5.27}$$

where $S_k\left(b_{k,g},\ S(0)_k, D_k, f, v, \tau\right)$ are the modelled signal intensities, $S_{k,g}$ are the actual (measured or simulated) signal intensities and N is the total amount of acquired data points. For a thorough discourse of error estimations in nonlinear modelling the reader is referred to Gallant[55] and Bates[56], only the essential steps are listed in the following.

The determined parameter estimates P can be used to estimate the unbiased variance of the residuals $\sigma_r = \frac{1}{N-k}\sum_{i=1}^{N} r_i^2$, with the number of model parameters k. The $k \times k$ covariance matrix is then given by

$$\mathrm{cov}(P) = \ \sigma_r \left(J_S^T(P) J_S(P)\right)^{-1}, \tag{5.28}$$

with the $N \times k$ Jacobian matrix $J_S(P) = \frac{\partial S}{\partial x}(P)$. Finally, the standard error of the estimated parameters can be determined as the square root of the diagonal elements of the covariance matrix

$$se_i = \sqrt{\mathrm{cov}(P)_{ii}}. \tag{5.29}$$

The capillary length l does not appear explicitly in the signal decay model, but is calculated as the product $v \cdot \tau$. Applying the propagation of uncertainty, its standard error se_l is given by

$$se_l = \sqrt{(se_v \cdot \tau)^2 + (se_\tau \cdot v)^2}. \tag{5.30}$$

5.4 Estimation Accuracy and Gradient Duration

In subsection 4.4, it was demonstrated how the signal attenuation factor F can be assigned to different regimes, depending on the number of directional changes M the particles experience during the diffusion experiment. M is dependent on the particle speed and capillary length of the underlying system and on the adjustable duration of the diffusion experiment T. An anticipatory choice of the duration of the diffusion experiment can therefore facilitate a more accurate estimation of the model parameters by sampling a more informative regime of F. To illuminate this issue further, a Monte Carlo simulation was performed.

Signal intensities were simulated for a theoretical two-compartment system with the following properties: fraction of particles inside perfused capillaries $f = 0.5$; thermal diffusion coefficient $D = 1 \times 10^{-3}\,\mathrm{mm}^2/\mathrm{s}$; average particle speed due to flow $v = 1\,\mathrm{mm/s}$; characteristic duration until a directional change occurs $\tau = 100\,\mathrm{ms}$ (which translates to a capillary length $l = 0.1\,\mathrm{mm}$); statistical speed distribution $\rho_{\mathrm{CN}}(v)$. A measurement consisting of two diffusion experiments, one with a monopolar and one with a flow-compensated gradient profile, was considered (in actuality it is of course beneficial to perform more than two experiments; however, time constraints may be

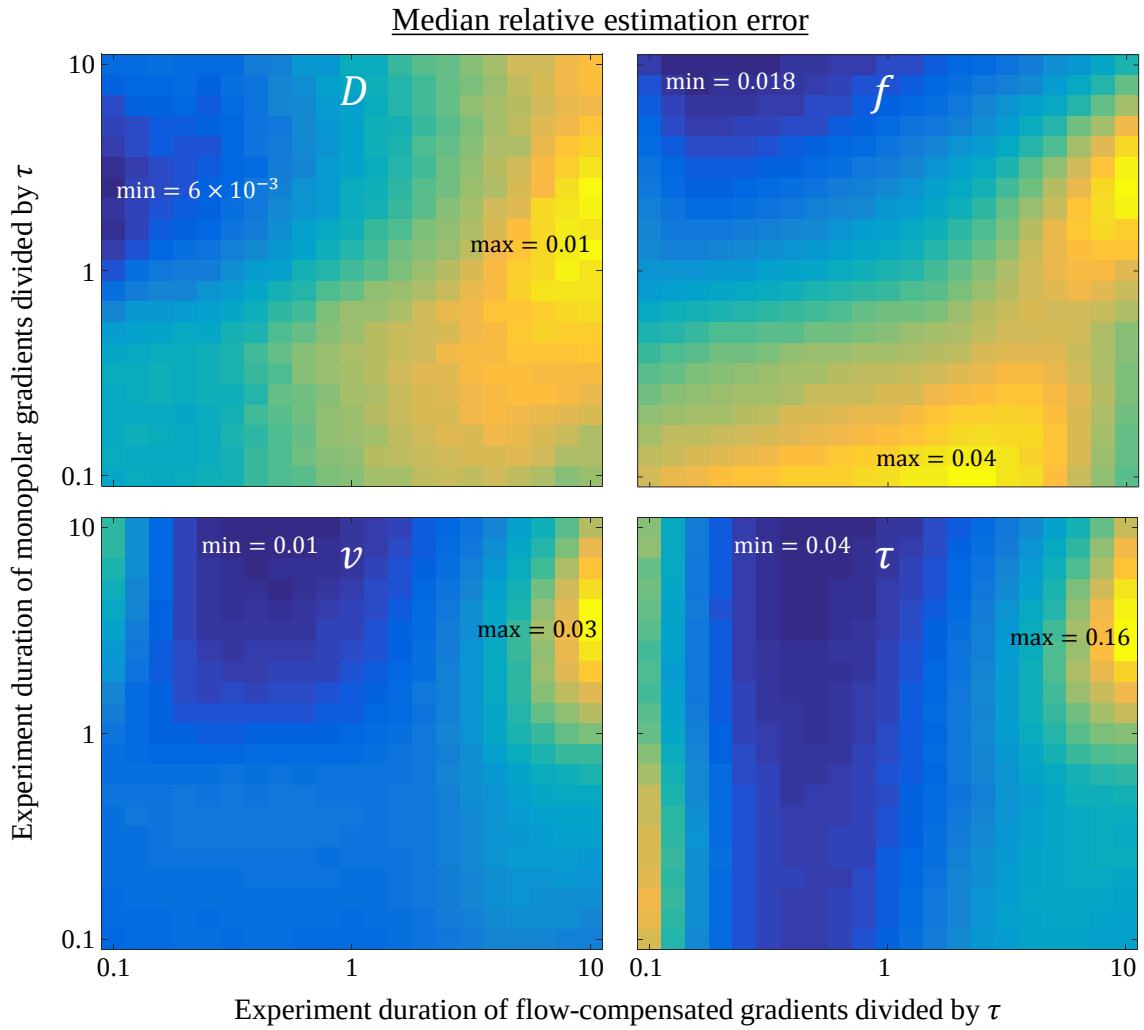

Figure 5.8: Median relative parameter estimation error by performing two diffusion experiments of varying duration with monopolar and flow-compensated gradients, respectively. The duration of each of the two diffusion experiments was varied independently relative to the characteristic interval between directional changes τ due to capillary flow.

prohibitive) with respective b-value sampling scheme $b = 0;\ 5;\ 10;\ 15;\ 20;\ 30;\ 45;\ 60;\ 80;\ 110;\ 150;\ 200;\ 280;\ 400;\ 600;\ 800\ \mathrm{s/mm^2}$. The duration of the diffusion preparation of each of the two experiments was varied independently, taking on 20 logarithmically spaced values between $T = \tau/10 = 10$ ms and $T = 10\tau = 1$ s. For each of the resulting 400 diffusion experiment duration pairs, 1000 iterations were run by adding Rician noise[57,58] to the simulated signal (corresponding to a signal-to-noise ratio of approx. 95 at $b = 0$) und subsequently obtaining parameter estimates as well as error estimates (see section 5.3).

Figure 5.8 shows the median relative estimation error (estimation error divided by the respective parameter value) for each model parameter depending on the duration of the diffusion experiments. As a general trend, it is observable that the simulated measurements where the experiment duration of the monopolar gradient was longer than τ and the experiment duration of the flow-

compensated gradients was shorter than τ yielded the lowest relative errors for all parameters. This therefore serves as a useful rule of thumb for defining measurement settings, provided τ can be roughly estimated a priori. In detail, the estimate for the thermal diffusion D has the smallest overall median relative error and profits from shortening the duration of the flow-compensated gradient as much as possible. This is intuitive, since exceedingly short flow-compensated gradients "compensate" the majority of the dephasing due to capillary flow and the resulting signal attenuation will solely be characteristic of the thermal diffusion. The estimation accuracy of the perfusion fraction f can be optimized by choosing a long experiment duration for the monopolar gradients, resulting in a biexponential decay of the respective attenuation factor F. Following the previously formulated rule of thumb minimizes the estimation error of the particle speed v as well as the characteristic duration τ and it can be appreciated that an optimal choice within the investigated range of the experiment durations may decrease the error of τ by a factor of 4. It should be noted that there is an interrelation between the true parameter values and the relative estimation errors. A small fraction f and/or a slow particle speed v impede the differentiation between the two compartments, reducing the parameter estimation accuracy in general.

To devise optimal measurement settings, the here deduced insights must be complemented by further considerations. Increasing the duration of the diffusion gradients inevitably increases the duration of the MRI sequence as a whole. For spin-echo sequences, this entails an increased echo time TE and may cause a significant loss of overall SNR due to T_2-relaxation effects. STEAM pulse sequences pose an option to mitigate this issue; however, this is accompanied with an inherent loss of half of the signal. In addition, T_1-relaxation will take place in between the $90°$ pulses and constrains in terms of total acquisition time may also play a prohibitive role. On the other hand, the minimum diffusion gradient duration is limited by the finite gradient amplitude and the desired maximum b-value of the diffusion experiment. Thus, for the measurements described in chapter 7, a flow-compensated diffusion experiment with shorter gradient durations (FC11) was employed using a reduced b-value set with a maximum b-value of $200\ \mathrm{s/mm^2}$ (see Table 5.1).

5.5 Phase-Distributions vs. Pseudo-Diffusion

In the course of section 4.4 it was shown how the attenuation factor F decays exponentially as a function of the applied b-value when the necessary preconditions are met, giving rise to the biexponential pseudo-diffusion model

$$S(b) = S_0\left((1-f)\cdot e^{-bD} + f\cdot e^{-b(D+D^*)}\right), \tag{5.31}$$

where the dephasing effect due to capillary flow is conveyed by the pseudo-diffusion coefficient $D^* = v^2\tau/6 = vl/6$, with the capillary length l. Due to its simplicity and reduced set of parameters, the biexponential model is the preferred choice in the literature for the analysis of perfusion effects using DW-MRI. However, whether the necessary preconditions, namely a large amount of directional changes M during the experiment and a particle speed distribution that results in a Gaussian phase distribution, are met for the biexponential model to be appropriate is often unclear or ignored. The biexponential model implies a linear relationship (assuming a constant capillary length l) between the pseudo-diffusion coefficient D^* and the average particle speed v. Using the

biexponential model to analyze a DW-MRI experiment, one can therefore deduce the average particle speed via[43] $v_{\mathrm{biexp}} = 6D^*/l$.

In the following, the ambiguity of the pseudo-diffusion coefficient D^* and the perfusion fraction f when the pseudo-diffusion preconditions are not met will be assessed by relating the biexponential-model-deduced parameters to predefined characteristics of a simulated system with capillary flow. For this purpose, a variety of capillary flow scenarios is considered to generate data akin to typical IVIM measurements with monopolar diffusion gradients using the phase-distribution model in combination with the MP28 gradient profile. Subsequent analysis of the generated signal decays facilitates a comparison between the true underlying flow characteristics and the parameter estimates obtained using the biexponential pseudo-diffusion model.

In subsection 5.5.1, a system comprising solely of perfused capillaries is considered, while in subsection 5.5.2 a two-compartment system is analyzed.

5.5.1 Perfusion Fraction Only

Assuming an exponential decay of the attenuation factor F as a function of the applied b-value, the pseudo-diffusion coefficient D^* constitutes the decay rate of $F(b)$ and is calculated as

$$D^* = \frac{-\ln\left(\frac{F(b_2)}{F(b_1)}\right)}{b_2 - b_1} = \frac{-\ln\big(F(b_2)\big)}{b_2}, \tag{5.32}$$

with $b_1 = 0$ and $F(0) = 1$. In Figure 5.9 it is shown how the determined value for D^* is affected by the choice of b_2 for different underlying particle speed distributions by relating $v_{\mathrm{biexp}} = 6D^*/l$ to the actual average particle speed v_{true}. For $M = 2$, the respective normalized phase distributions are distinctively non-Gaussian (see Figure 5.5), accordingly, $F(b)$ does not decay exponentially and v_{biexp} is highly dependent on the choice of b_2 (Figure 5.9 A). The estimate v_{biexp} deteriorates with respect to the actual average particle speed v_{true} as b_2 increases. Moreover, v_{biexp} underestimates the particle speed consistently, except for the delta-distributed particle speeds, where the zeros of the sinc-like decay of $F(b)$ leads to an asymptotic behavior of v_{biexp}. For $M = 16$, the discrepancy between v_{biexp} and v_{true} is much less severe (Figure 5.9 B). As b_2 approaches zero, v_{true} is well approximated by v_{biexp} independent of the speed distributions, however, for large b-values non-delta-distributed particle speeds again result in an underestimated v_{biexp}. The different behaviors illustrated in Figure 5.9 A and Figure 5.9 B emphasize the impact of varying M on the applicability of the biexponential model.

In Figure 5.10 this is further broken down by showing the behavior of v_{biexp} as a function of M and the particle speed v_{true}, using varying values for b_2 and the particle speed distribution $\rho_{\mathrm{CN}}(v)$. Panel A shows v_{biexp} divided by v_{true} as a function of M while keeping the particle speed v_{true} and the diffusion duration T constant (achieved by adapting τ, which translates to effectively adapting the capillary length l). As anticipated, v_{biexp} heavily underestimates v_{true} for small M, which improves as M is increased, however, v_{biexp} remains biased even up to large M depending on the value of b_2. In panel B the particle speed v_{true} is variable while keeping $M = 8$ constant (which again translates to adapting the capillary length l). At small particle speeds, v_{biexp}

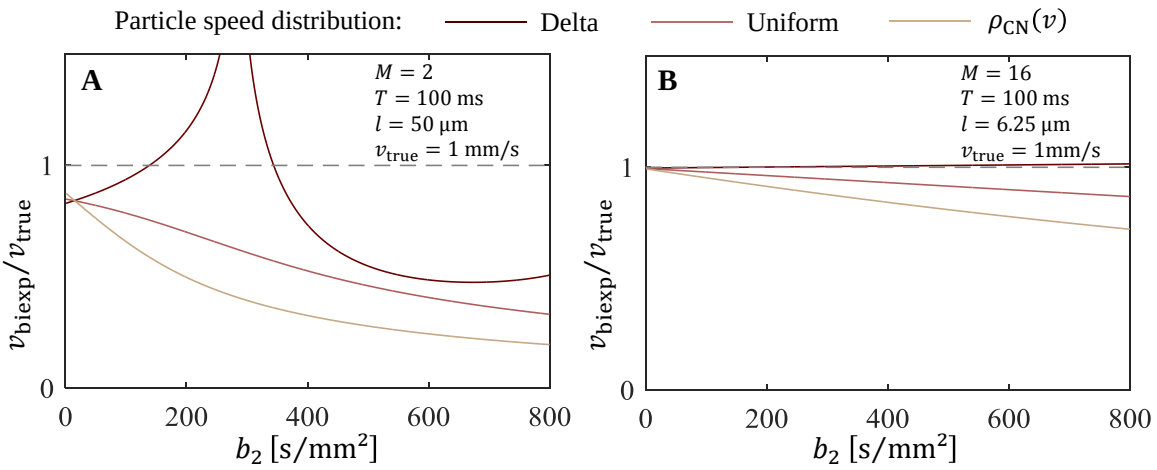

Figure 5.9: Relationship between the estimated particle speed v_{biexp} and the actual particle speed v_{true} depending on the choice of the diffusion weighting (b_2-value) for different underlying particle speed distributions. **A**: For $M = 2$, the estimate v_{biexp} is highly dependent on the diffusion weighting, severely underestimating the particle speed v_{true}. **B**: At a higher value of $M = 16$, the estimate v_{biexp} improves, however, a dependency on the diffusion weighting as well as the underestimation bias remains for non-delta-distributed particle speeds.

approximates v_{true} well, since even the highest used b_2-value ($= 400\,\mathrm{s/mm^2}$) acts as a "low" b-value due to the very slow decay of $F(b)$ at small particle speeds. In contrast, a strong discrepancy is observed at high particle speeds, where $F(b)$ decays rapidly. Usually, the capillary length l is constant in the investigated object of interest, meaning that the particle speed v_{true} and the number of directional changes M are linearly proportional to each other. Panel C shows how v_{biexp} behaves in such a scenario. The capillary length l and the duration of the experiment T were hereby chosen such that $M = v_{\mathrm{true}}/[\mathrm{mm/s}]$. The resulting behavior of v_{biexp} is essentially a combination of panel A and panel B: At small M, v_{biexp} underestimates v_{true} heavily, which improves with increasing M. Coincidentally, fast particle speeds introduce a bias as illustrated in panel B. Panel D is an alternative illustration of the same scenario, where v_{biexp} is not normalized and plotted vs v_{true} and M, respectively. While v_{biexp} does increase monotonously with v_{true}, it is apparent that v_{biexp} is an inaccurate estimate of the particle speed in this single compartment scenario when the pseudo-diffusion preconditions are not fully met.

The results from this section demonstrate the ambiguity of the pseudo-diffusion coefficient D^* in the investigated scenario. The relationship between D^* and the particle flow speed v established by Le Bihan and Turner[43] seems to be only valid under restrictive preconditions, which should be verified in an actual experiment. However, densely sampling the initial signal decay using small b-values of less than $50\ \mathrm{s/mm^2}$ potentially alleviates the negative bias of v_{biexp}.

5.5.2 Two-Compartment Model

Based on the phenomena described in the previous section, it is of interest to investigate the consequences of varying flow characteristics in a hypothetical IVIM measurement. In contrast to the previous section, a two-compartment system is now considered: One compartment is governed by

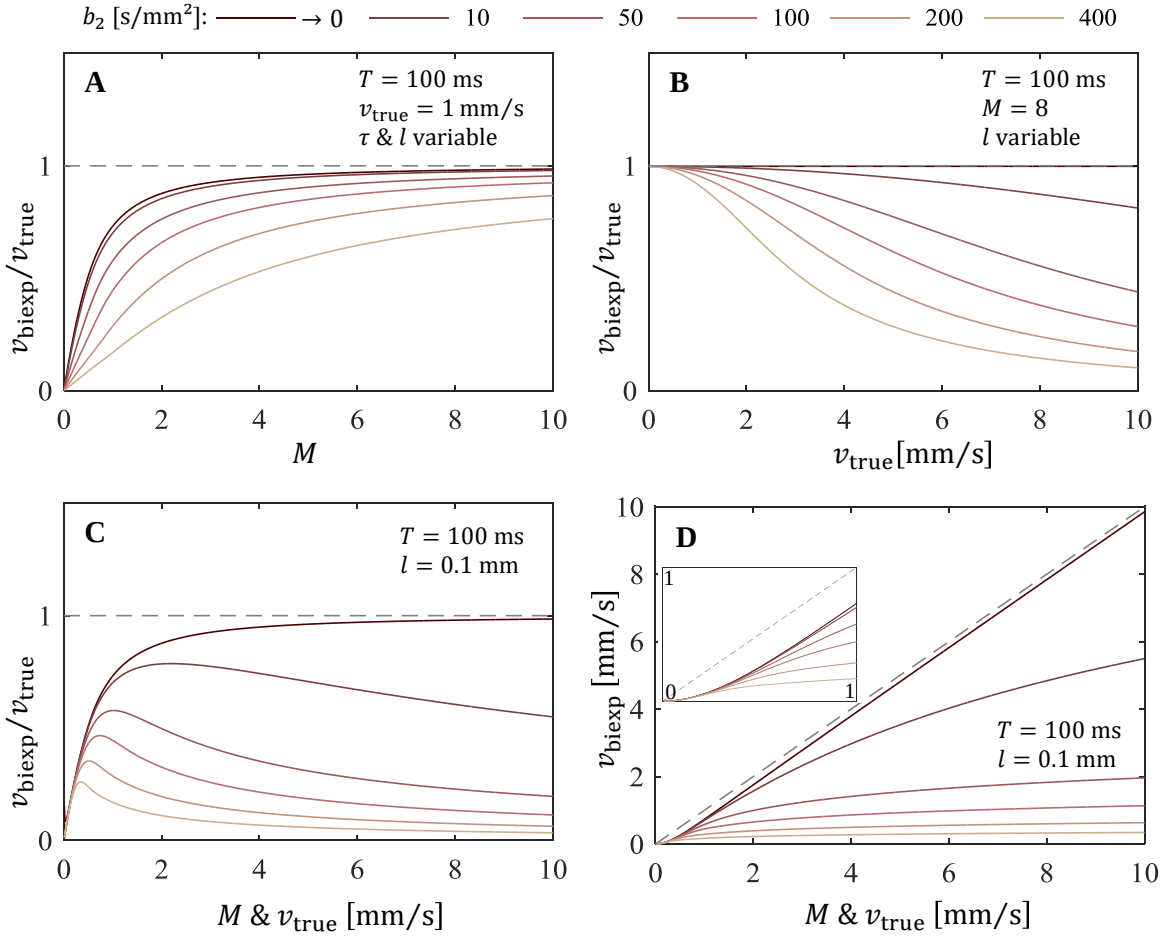

Figure 5.10: Behavior of v_{biexp} as a function of M and the particle speed v_{true}, using varying values for b_2. **A**: $v_{\mathrm{biexp}}/v_{\mathrm{true}}$ as a function of M with constant v_{true} and T. **B**: $v_{\mathrm{biexp}}/v_{\mathrm{true}}$ as a function of v_{true} with constant M and T. **C**: $v_{\mathrm{biexp}}/v_{\mathrm{true}}$ as a function of $M = v_{\mathrm{true}}/[\mathrm{mm/s}]$ with constant T and l. **D**: v_{biexp} as a function of $M = v_{\mathrm{true}}/[\mathrm{mm/s}]$ with constant $T$and l.

thermal diffusion only (fraction $1 - f$), while the other is subjected to additional flow effects (fraction f). The methodology of an IVIM measurement to assess capillary perfusion is generally as follows: A multitude (usually ≥ 8) of different b-values is sampled using a monopolar (or more generally non-flow-compensated) diffusion gradient scheme. The sampling is more dense for small b-values to improve the estimation accuracy of the perfusion-related parameters: the pseudo-diffusion coefficient D^* and perfusion fraction f. Subsequently, the measured signal intensities are used to estimate the biexponential model (eq. (5.31)) parameters using a Levenberg-Marquardt nonlinear least-squares algorithm. For the analytical assessment in this section, the sampling scheme $b = 0;\ 5;\ 10;\ 15;\ 20;\ 30;\ 45;\ 60;\ 80;\ 110;\ 150;\ 200;\ 280;\ 400;\ 600;\ 800\,\mathrm{s/mm^2}$ was used. The signal intensities $S(b)$ were simulated according to eq. (4.23) using a constant perfusion fraction $f_{\mathrm{true}} = 0.3$ and thermal diffusion coefficient $D_{\mathrm{true}} = 1 \times 10^{-3}\,\mathrm{mm^2/s}$ while varying the two flow-related parameters "average particle speed" v and "number of directional changes during the diffusion experiment" M. The total duration $\Delta + \delta$ of the monopolar diffusion gradients was set to $T = 100\,\mathrm{ms}$ with no gap between the gradient lobes. For the flow-induced particle

speed distribution, $\rho_{CN}(v)$ was used. For each set of flow parameters, the respective model parameters f, D, D^* (and therefore v_{biexp}) were determined via least squares fitting.

Figure 5.11 A and B depict the determined normalized v_{biexp} and the determined perfusion fraction f, respectively, as a function of the average particle speed v_{true}. At slow particle speeds, the dephasing effect due to flow is small, resulting in a similar signal decay of the two compartments. The differentiation of the two compartments is thus impeded[59], reflected by the unsteady behavior of v_{biexp}, f and D. This effect is more persistent for large M, since more directional changes (while v_{true} is kept constant) during T lead to a reduction in the variance of $\rho_{\vartheta_h}(\vartheta, M)$ (see subsection 0). As the particle speed increases, the least squares fit becomes more stable, however, contrary to the findings in the previous section, v_{biexp} initially overestimates v_{true}. This behavior is owed to the interaction of D^* and f: As the least-squares algorithm minimizes the residual sum of squares between the simulated data and a biexponential signal decay (as presumed by the pseudo-diffusion model), large parts of the perfusion fraction are wrongly ascribed to the solely diffusing fraction. Consequently, the determined f substantially underestimates f_{true} for all M while overestimating the decay rate of the perfusion fraction, in turn leading to the overestimation of $D^*$and thus v_{biexp}. Furthermore, D consistently overestimates D_{true} for the larger flow rates as well, however, here the bias is less severe. As v_{true} increases, the normalized v_{biexp} decreases and eventually underestimates v_{true} at fast flow speeds. The particle speed at which this crossing appears increases with M. Figure 5.11 D shows the deceptive nature of the biexponential model fit: The fitted curve seems to represent the data well and it is extremely difficult to perceive any discrepancies visually. Panel E, however, clearly illustrates the systematic residuals between simulated data and model fit. Note, that the simulated signal is void of any noise. In an actual measurement, any such observation will be further obfuscated by noise.

Figure 5.12 illustrates the behavior of v_{biexp} when f as well S_0 are fixed to their true value, i.e. $f = f_{\mathrm{true}} = 0.3$ and $S_0 = S_{0_{\mathrm{true}}} = 1$, effectively reducing the free model parameters to D and D^*. The estimation problem is now similar to the conditions in the previous section, since the amplitude of each fraction is fixed and the remaining degrees of freedom are merely to fit the slope of the signal decay. Accordingly, the relationship between v_{biexp} and v_{true} in Figure 5.12 A is similar to the findings shown in Figure 5.10 B with $b_2 \approx 100\ \mathrm{s/mm^2}$, demonstrating a consistent underestimation of v_{true}. However, Figure 5.12 B plainly shows the inability of the biexponential model to represent the simulated data accurately when the compartment amplitudes are fixed to their correct values.

Finally, in Figure 5.13, a case is investigated where v_{true} and M are linearly proportional, i.e. the capillary length l stays constant (as in the previous section, the capillary length l and the duration of the experiment T where chosen so that $M = v_{\mathrm{true}}/[\mathrm{mm}/s]$). This creates a situation similar to chapter 7, where experiments with incrementally increasing flow through a constructed phantom were performed. Once more, all biexponential model parameters were fit freely. Again, at slow v_{true} the estimated parameters are showing an erratic behavior until the fitting becomes more stable at higher flow speeds. Panel A illustrates a rather benign deviation of v_{biexp} from v_{true}. This can be logically deduced from Figure 5.11 A: At slow flow speeds, v_{true} is best estimated by

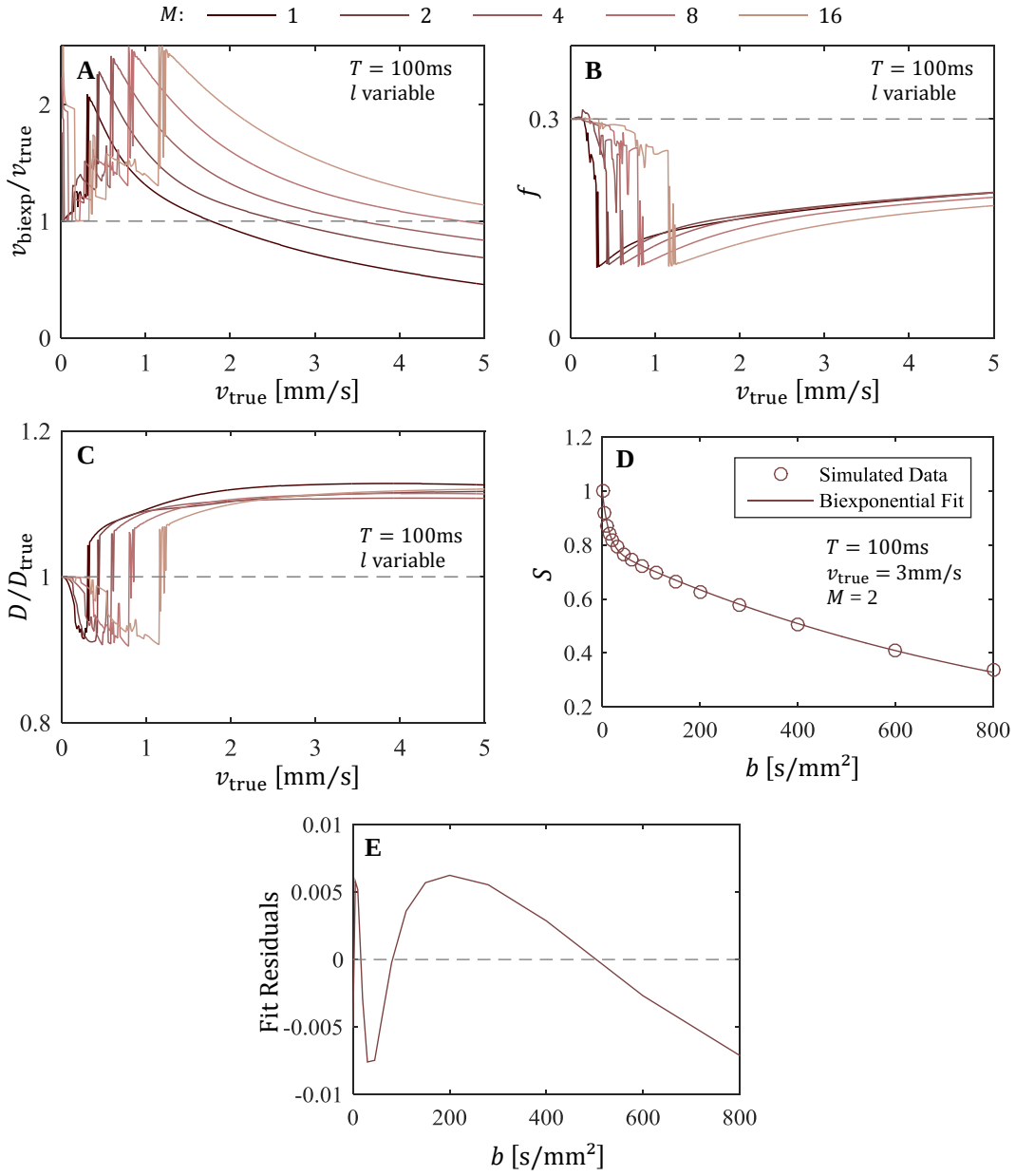

Figure 5.11: Study of biexponential model parameter estimates as a function of the particle flow speed v_{true} for varying M in a two-compartment system. For simulation and parameter estimation details please refer to the text in subsection 5.5.2. **A** and **B**: $v_{\text{biexp}}/v_{\text{true}}$ and f, respectively, as a function of v_{true}. At slow particle speeds, the differentiation of the two compartments by the least squares model fit is impeded, reflected by the unsteady behavior of v_{biexp} and f. Once the least squares fit stabilizes, v_{biexp} initially overestimates v_{true} owed to the interaction with f, which heavily underestimates f_{true}, independent of M. As v_{true} increases, it is eventually underestimated by v_{biexp} (depending on M), while f remains well short of f_{true}. **C**: The fitted diffusion coefficient D displays an unsteady behavior at slow speeds as well, followed by a consistent overestimation of D_{true} of approx. 10% at higher flow rates. **D**: Simulated data and biexponential model fit for $M = 2$. The inappropriate model fits the data well and it is difficult to recognize discrepancies, however, panel **E** clearly illustrates that the residuals show a systematic pattern.

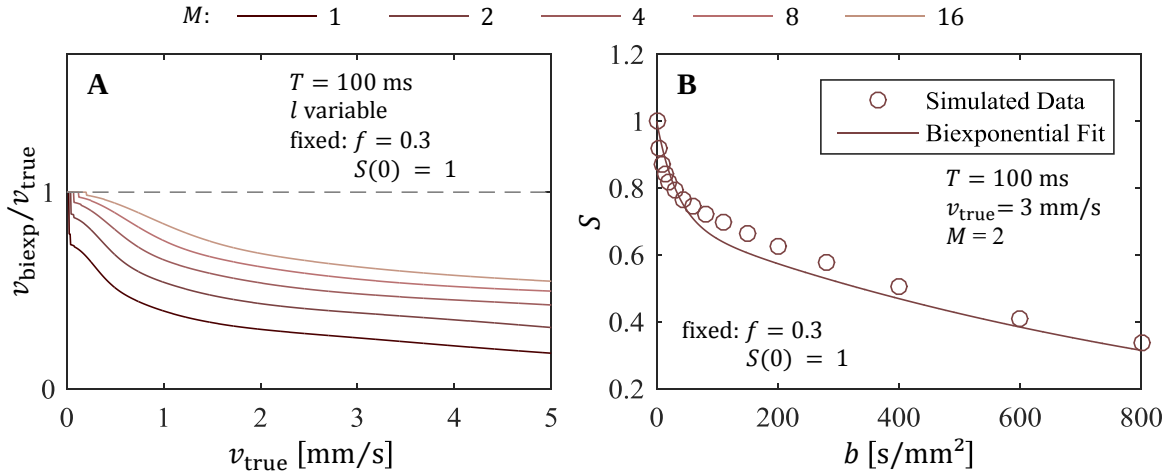

Figure 5.12: Simulated data of a two compartment model, as previously described, analyzed using the biexponential model with parameter constraints. The parameters f as well S_0 are fixed to their true value, i.e. $f = f_{\text{true}} = 0.3$ and $S_0 = S_{0\,\text{true}} = 1$, effectively reducing the free model parameters to D and D^*. **A**: The relationship between v_{biexp} and v_{true} is now similar to the findings shown in Figure 5.10 with $b_2 = 100\ \text{s/mm}^2$, demonstrating a consistent underestimation of v_{true}. **B**: When the amplitudes of the two compartments are fixed to their true value, the biexponential model fails to result in a proper fit of the data.

v_{biexp} in a small M scenario. As v_{true} increases however, larger M scenarios yield a better estimate. Consequently, since v_{true} and M are linearly proportional in the scenario in Figure 5.13, the overall deviation of v_{biexp} from v_{true} is less severe compared to the previous findings. The estimated perfusion fraction f in Figure 5.13 B increases slightly as v_{true} increases, yet a significant bias remains. Panel C is an alternative representation of panel A where the estimated v_{biexp} was not normalized, therefore deviations at slow v_{true} appear less severe and v_{biexp} as a function of v_{true} stays appreciably close to the identity line.

The findings in this section highlight potential fallacies resulting from inappropriately applying the pseudo-diffusion model to analyze capillary flow. The biexponential model is seemingly able to fit a wide array of decays that are not of biexponential nature[60] while keeping residuals small and inconspicuous in the presence of noise. Furthermore, the interaction of the parameters in the biexponential model impedes the a priori estimation of the potential biases. Aside from the number of directional changes M during the diffusion experiment, the particle speed distribution was shown to be of great impact on the signal decay. This section focused on the signal decay resulting from the previously deduced particle speed distribution $\rho_{\text{CN}}(v)$. Due to the L-shape of $\rho_{\text{CN}}(v)$ far higher values of M are needed to result in an approximately Gaussian phase distribution compared to delta-distributed particle speeds, making the biexponential signal-decay model inappropriate for the considered scenarios.

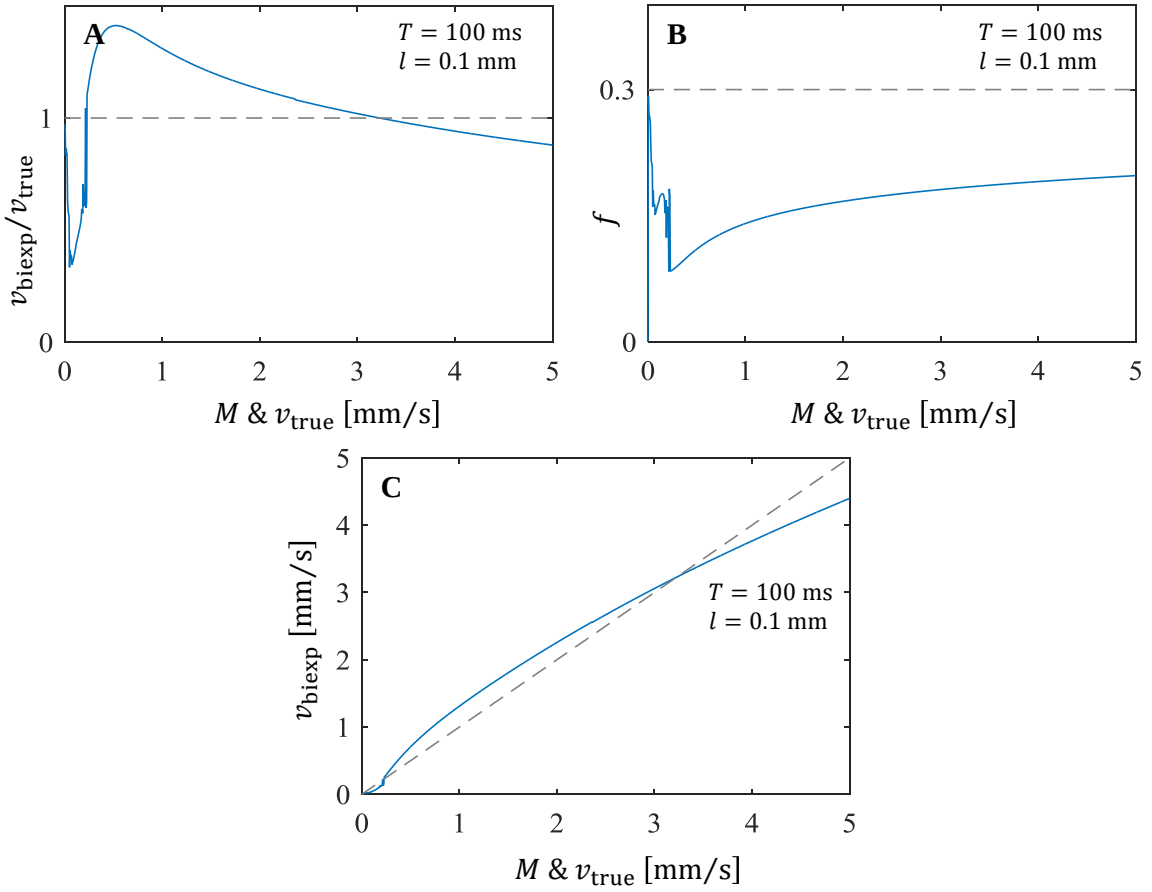

Figure 5.13: Scenario in which M and v_{true} are linearly proportional (i.e. constant capillary length l), comparable to the measurement series in chapter 7. **A**: The deviation between v_{biexp} and v_{true} is more benign than in the previous scenarios. **B**: f still severely underestimated f_{true} and increases slightly with faster flow speeds. **C**: The estimated v_{biexp} is not normalized, therefore deviations at slow v_{true} appear less severe and v_{biexp} as a function of v_{true} stays appreciably close to the identity line.

6 Capillary Phantom: Construction & Characterization

This chapter describes the construction and characterization of a capillary phantom, designed to facilitate the investigation of dephasing effects in DW-MRI due to flow in an interconnected, randomly orientated network. Constructing a perfusable network that matches the dimensions of in vivo capillary beds is challenging. So far, studies analyzing the effects of capillary flow in diffusion-weighted MRI have resorted to using flow phantoms made of sponges[61], plastic tubes[44,62] or columns packed with microspheres[42,63,64] to simulate capillary perfusion. While these phantoms may be able to provide some form of flow-induced dephasing, their structure deviates substantially from in vivo capillary beds limiting their applicability, especially with regard to the phase-distribution model.

Section 6.1 describes the construction process of a perfusable capillary phantom, closely mimicking the geometry of in vivo capillary beds. Subsequently, the qualitative and quantitative analysis of the constructed phantom using optical microscopy is presented in section 6.2. Differences of the magnetic susceptibility between the matrix material and the liquid inside the capillary bed may lead to undesirable effects such as image artifacts and rapid relaxation processes when performing MRI experiments. To minimize these potential issues, a susceptibility-matched sodium chloride solution was determined via a dilution series, described in section 6.3. After flooding the capillary phantom with the matched sodium chloride solution, basic magnetic resonance imaging as well as quantitative analysis of the relaxation processes and thermal diffusion in the absence of flow are presented in section 6.4.

6.1 Phantom Construction Process

As previously proposed by Bellan et al.[65], a 3-dimensional microchannel network was constructed using melt-spun sugar fibers embedded in a synthetic resin (Figure 6.1). With this method, it is possible to fabricate a sealed-off artificial capillary bed, accessible via two macro-channels. Sugar fibers were produced using a modified cotton candy machine (Candyland, Klarstein, Berlin, Germany), optimized in terms of rotational speed and heating temperature to adjust the diameter of the sugar filaments to match in vivo capillary scales of $2 - 10$ µm as reported by Potter and Groom[66]. Store-bought granulate sugar was used for the manufacturing of melt-spun fibers, which were collected on a paper cone and afterwards evenly compressed to a homogenous and dense interconnected fiber ball. To provide the phantom with an inlet and an outlet, sugar sticks were molded around metal wires and attached to Luer-Lock adapters. Parts of the metal wires protruded beyond the Luer-Lock adapters to enable a fastening of the construct for the curing process later on. Subsequently, the sugar sticks were carefully attached to the fiber ball on opposing ends. In order to facilitate a large number of connections in between the ball and the macrochannel sugar sticks,

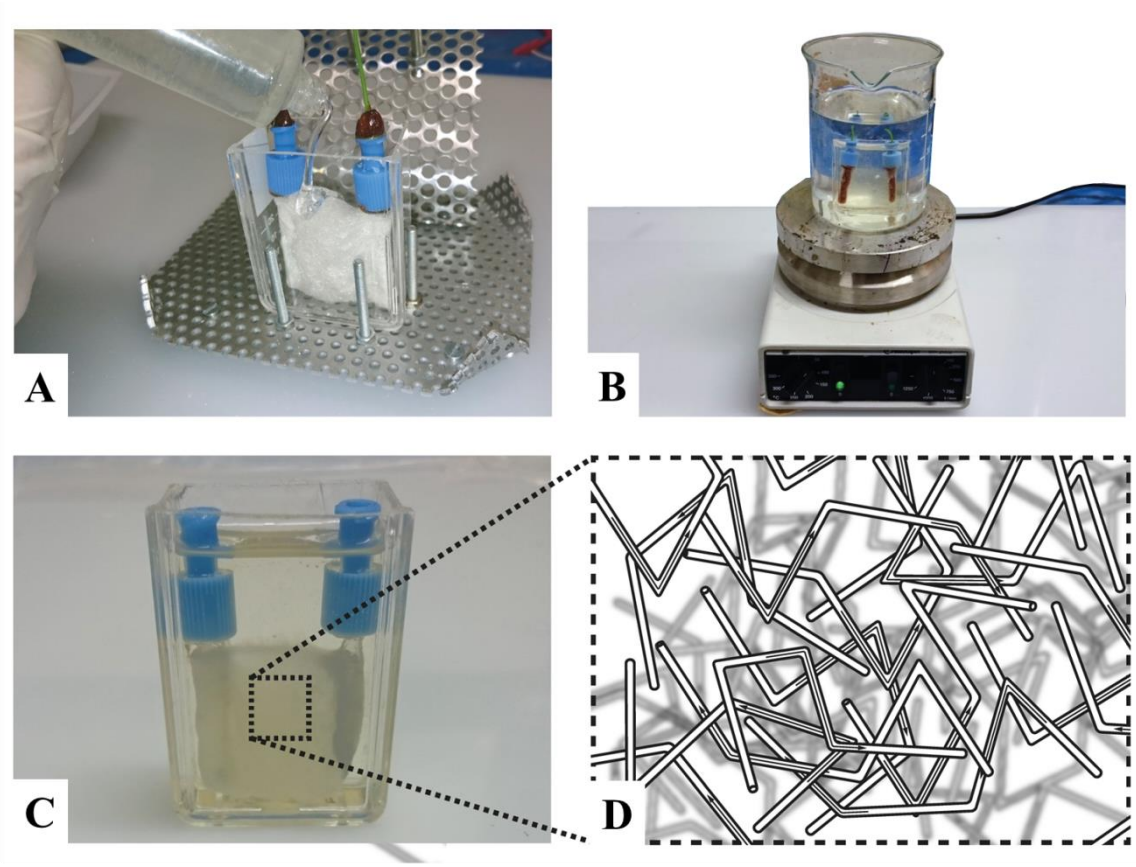

Figure 6.1: Construction process of the capillary phantom. **A**: A cotton candy fiber ball, attached to two sugar sticks serving as feeding and draining macrochannels, was placed inside a plastic mold and covered with two-component synthetic resin. **B**: After curing, the phantom was placed in a water-ethanol bath to dissolve the sugar structures embedded in the epoxy. **C** and **D**: Eventually, a highly interconnected capillary system remains, which was filled with a sodium chloride solution of 213 g NaCl/l using demineralized water as solvent (illustration with permission after[120]).

it is crucial to expose the fiber system to an environment of increased humidity. The fiber ball with the attached sugar sticks was then placed in a box-shaped plastic container ($5 \times 3 \times 2$ cm^3) and fastened to a custom-built framework. In its original design proposed by Bellan et al., the matrix material consisted of either PDMS (a silicon-based polymer) or epoxy. Our initial experiments have shown that the PDMS does not withstand enough pressure for the intended use, therefore, a low viscosity two-component epoxy resin (E45GB, Breddermann Kunstharze, Schapen, Germany) was used as matrix material. The epoxy was carefully poured into the container along the inner side, ensuring that the resin rose slowly from the bottom to the top of the fiber ball to avoid the entrapping of air bubbles. To degas the system further, the phantom was placed in a vacuum chamber for several minutes until no residual air bubbles were visible within the epoxy resin. After 24 hours of subsequent curing, the epoxy-sugar block was placed in a water-ethanol bath at 40°C for several days to dissolve the sugar structures embedded in the hardened epoxy, leaving a highly interconnected capillary system. Once the sugar was completely dissolved, the capillary network was filled with a sodium chloride solution of 213 g NaCl/l using demineralized water as solvent (see section 6.3).

6.2 Characterization by Optical Microscopy

To obtain structural information about the capillary network, such as average capillary diameter and segment length, optical microscopy of the constructed phantom was performed. The images were taken using an optical microscope of type DM2500 (Leica, Wetzlar, Germany). The flooded phantom is opaque, impeding the acquisition of contrast-rich images using transmitted light only. This was counteracted by additionally illuminating the phantom laterally during microscopy, giving the resulting images a relief-like appearance (exemplary image portrayed in Figure 6.2).

The microscopy images show clearly that the dissolved sugar structures indeed leave a highly interconnected capillary system. Furthermore, the network seems to be strewn with circular dilations. Taking the non-illustrated z-dimension into account, it is likely that these dilations are actually spherical in shape. They appear to originate from sugar crystals sticking to the melt-spun sugar and residual bubbles of air that were not completely degassed during the construction process. It will become apparent in chapter 7 that these dilations play an important role with regard to the signal decay in the flow-dependent DW-MRI experiments.

A total of 9 imaged sections of the capillary network were analyzed using the software ImageJ[67]. Capillary segments were manually drawn in along their axis of orientation (longitudinal), yielding their length and their angular orientation within the imaged xy-plane. The diameter of the capillary segments was estimated by measuring the width perpendicular to the axis of orientation (transverse), the diameter of all discernible spherical dilations was drawn in and measured as well. It should be noted that the longitudinal (length and angular orientation) and transverse (diameter) measurement of the capillary segments was not performed in a pairwise fashion, however, in

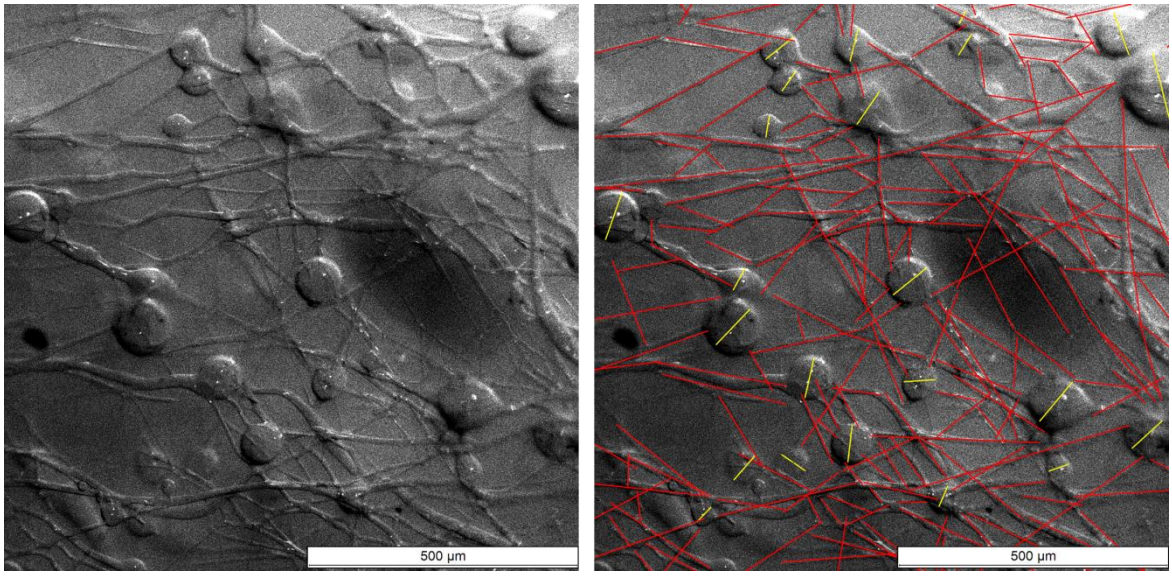

Figure 6.2: Exemplary microscopy image of the capillary network taken with a DM2500 (Leica, Wetzlar, Germany) optical microscope. Due to the opaqueness of the phantom, image contrast was enhanced by exposing the phantom to light from a lateral direction, giving the image a relief-like appearance. A highly interconnected capillary system is left by the dissolved sugar structures, strewn with spherically shaped dilations presumably caused by residual air bubbles and sugar crystals. On the right, the marked capillary segments (red) and spherical dilations (yellow) are illustrated.

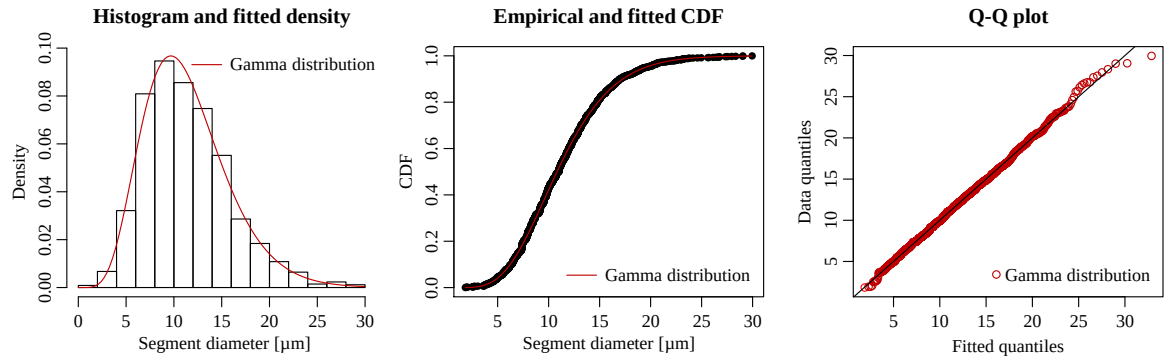

Figure 6.3: Capillary segment diameter measured using optical microscopy. The average segment diameter was 11.4 ± 4.4 µm. The histogram was well approximated by a fitted gamma distribution with shape parameter $\alpha = 6.679$, rate parameter $\beta = 0.587$ as demonstrated in the Q-Q plot. The Q-Q plot, comparing the quantiles derived from the measurements and the theoretical gamma distributed quantiles, closely follows the identity line.

particular for the longitudinal measurement, importance was attached to mark every discernible segment. In total, 1726 capillary segments and 225 spherical dilations were marked inside the 9 imaged sections. As optical microscopy results in a 2D representation of the imaged object, the propagation of capillaries in z-direction could not be captured, which may lead to an underestimation of capillary lengths. However, this effect is somewhat mitigated by the fact that the analysis was restricted to structures that were clearly delineated in their entirety, which precludes capillaries strongly aligned with the z-direction due to the limited depth of focus.

Figure 6.3 depicts the histogram of the measured capillary segment diameters with an average segment diameter of 11.4 ± 4.4 µm. The histogram was analyzed using the R[68] package fitdistrplus[69] and best approximated by a gamma distribution with fitted shape parameter $\alpha = 6.679$ and rate parameter $\beta = 0.587$ (mean of fitted distribution: $E[X] = \alpha/\theta = 11.39$). A Kolmogorov–Smirnov test was performed to compare the equality of the measured values and the fitted distribution. The test yielded a Kolmogorov–Smirnov statistic of $D_n = 0.017$ and a p-value of $p = 0.693$, suggesting a high similarity between the distribution of diameters and the fitted gamma distribution ($0 \leq D_n \leq 1$ and $D_n = 0$ when comparing identical distributions).

The measured average segment length was 162 ± 78 µm and the histogram was best approximated by a Log-normal distribution with parameters $\mu = 4.972$ and $\sigma = 0.484$ and mean $E[X] = \exp(\mu + \sigma^2/2) = 162.3$ (Figure 6.4). The Kolmogorov–Smirnov statistic was $D_n = 0.021$ with a p-value of $p = 0.448$.

The dimensions of the capillaries are within the range of values reported from the human cerebral capillary system[70] (reported lengths: 63.3 ± 53.7 µm; reported diameters: 6.56 ± 1.27 µm) and the cerebral cortex of cats[71] (reported lengths: 12 to 302 µm; reported diameters: 5.0 ± 0.91 µm).

As briefly mentioned, Figure 6.2 depicts multiple circular dilations, strewn in the capillary network, which will become important with regard to the signal decay in the flow-dependent DW-MRI experiments. The measured average dilation diameter was 62.4 ± 20.6 µm and the histogram was best approximated by a Log-normal distribution with parameters $\mu = 4.081$ and $\sigma = 0.326$

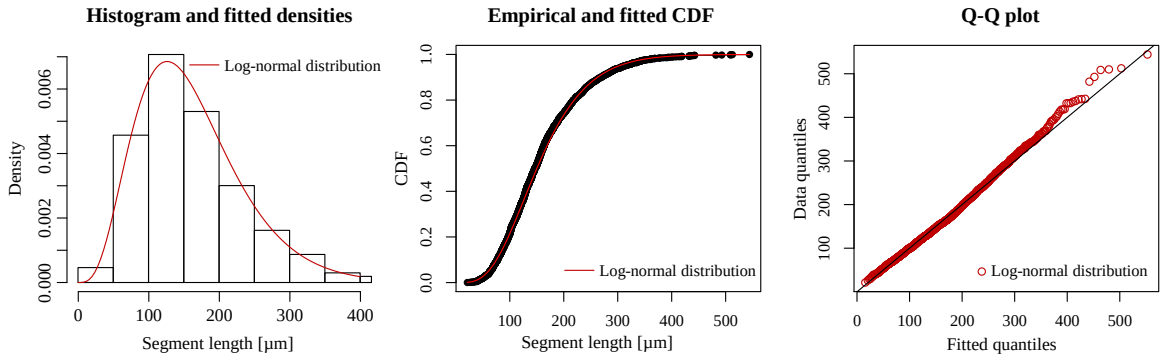

Figure 6.4: Capillary segment lengths measured using optical microscopy. The average segment length was 162 ± 78 µm. The histogram was well approximated by a Log-normal distribution with parameters $\mu = 4.972$ and $\sigma = 0.484$ as demonstrated in the Q-Q plot. The Q-Q plot, comparing the quantiles derived from the measurements and the theoretical gamma distributed quantiles, closely follows the identity line.

and mean $E[X] = \exp(\mu + \sigma^2/2) = 62.4$ (Figure 6.5). The Kolmogorov–Smirnov statistic was $D_n = 0.069$ with a p-value of $p = 0.239$.

It is of interest to estimate the ratio of the volume inside the capillaries V_{cap} to the total network volume $V_{\text{cap}} + V_{\text{dil}}$. In the following calculations, a conservative observational error of the individual measurements of ± 3 µm was used for the error propagation. For the imaged sections, V_{dil} can be calculated by assuming a spherical geometry and summarizing the individual volumes of the marked dilations

$$V_{\text{dil}} = \sum_{i=1}^{K} \frac{\pi}{6} {d_{\text{dil},i}}^3 = 39.0 \pm 0.2 \text{ mm}^3, \tag{6.1}$$

with the diameter $d_{\text{dil},i}$ of dilation i. To calculate V_{cap}, the capillary geometry was assumed to be cylindrical. Due to the fact that the capillary lengths and diameters were not measured in a pairwise fashion, V_{cap} was estimated by using the mean of the distribution of the squared diameters as

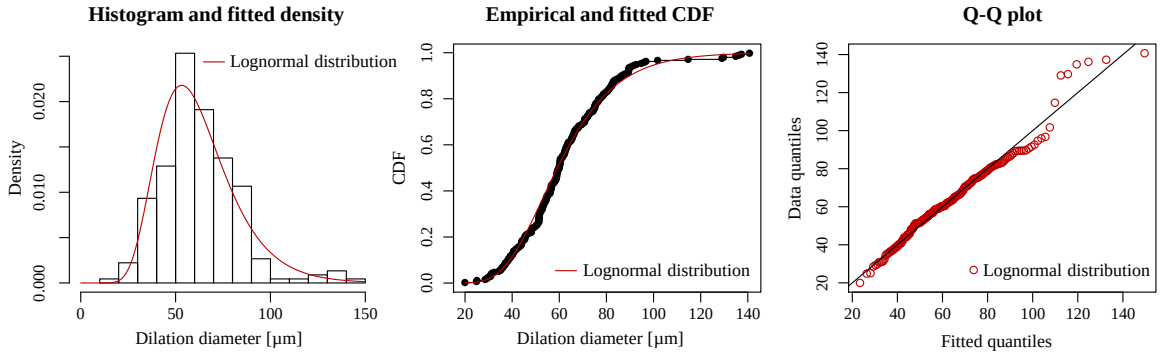

Figure 6.5: Dilation diameters measured using optical microscopy. The average dilation diameter was 62.4 ± 20.6 µm. The histogram was moderately approximated by a Log-normal distribution with parameters $\mu = 4.081$ and $\sigma = 0.326$.

follows:

$$V_{\mathrm{cap}} = \sum_{i=1}^{N} l_{\mathrm{cap},i} \sum_{k=1}^{M} \frac{\pi}{M} \left(\frac{d_{\mathrm{cap},k}}{2} \right)^2 = 32.6 \pm 0.05\ \mathrm{mm}^3, \tag{6.2}$$

with the diameter $d_{\mathrm{cap},k}$ of capillary segment k and the length $l_{\mathrm{cap},i}$ of capillary segment i. Using the results from eq. (6.1) and (6.2), one can calculate

$$\frac{V_{\mathrm{cap}}}{V_{\mathrm{cap}} + V_{\mathrm{dil}}} = 0.454 \pm 0.002. \tag{6.3}$$

It should be emphasized that the ratio deduced in eq. (6.3) is a rough estimate. The calculated error is small due to the large number of measured capillaries and dilations; however, the achieved coverage using optical microscopy is sparse and the structure of the phantom may vary in unsampled areas. Nevertheless, it can be deduced that the total volumes of the dilations V_{dil} and the capillary segments V_{cap} are most likely to be of the same order of magnitude and to be comparable in size.

The distribution of the angular orientations of the marked capillaries within the imaged sections is visualized in Figure 6.6. The visual impression of uniformly distributed angles is supported by a Kolmogorov–Smirnov statistic of $D_n = 0.0102$ with $p = 0.808$, when comparing the measured angles with a uniform distribution. Unfortunately, the angular distribution in the z-direction could not be probed by means of optical microscopy, however, the randomness of the construction process and the uniform distribution in the xy-plane imply that the 3D orientation distribution is isotropic on the macroscopic scale of an imaged voxel ($5 \times 5 \times 5\ \mathrm{mm}^3$).

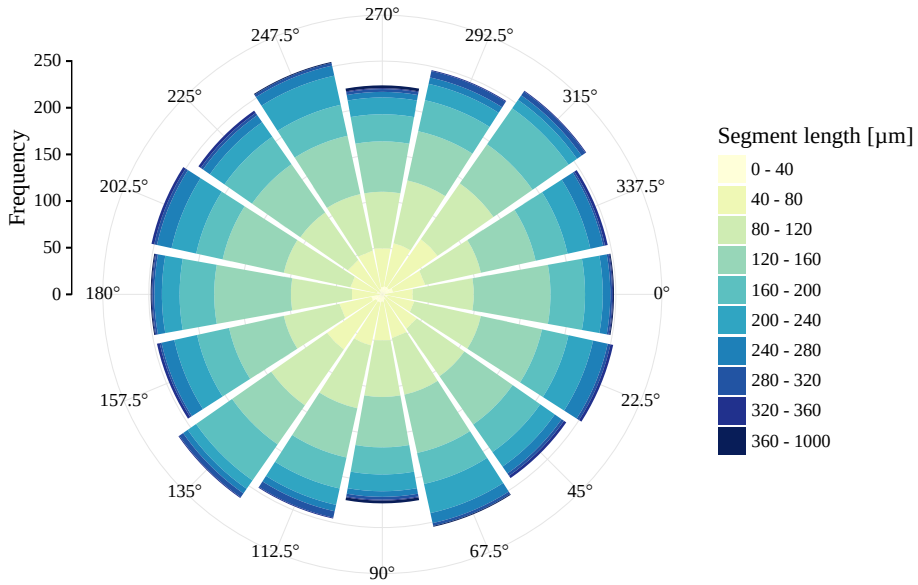

Figure 6.6: Visualization of the angular distribution of the marked capillaries within the imaged plane. The angular distribution was mapped onto a polar rose plot, creating a direction-intensity histogram. All angles were mirrored on the horizontal axis, as a capillary orientation of $\alpha > 180°$ corresponds to $\alpha' = 180° - \alpha$ and vice versa. The angular distribution appears to be uniform.

6.3 Susceptibility-Matched Filling Fluid

The dimensionless magnetic susceptibility χ of a substance describes its magnetic behavior when placed in an external magnetic field. Substances with susceptibility $\chi < 0$ are referred to as *diamagnetic* and form an internal magnetization that opposes the external field, resulting in a repellant force and an attenuation of the local magnetic field strength. Conversely, substances with susceptibility $\chi > 0$ are referred to as *paramagnetic* and form an internal magnetization that aligns with the external field, resulting in an attraction of the substance and an increased local magnetic field strength. Substances imaged using MRI generally have a very weak interaction with the external magnetic field, however, even small differences of the magnetic susceptibilities of adjacent substances can lead to inhomogeneities in the local magnetic field. These inhomogeneities can cause severe artifacts in the acquired images[72], which is especially true for EPI sequences[73] commonly used for DW-MRI (subsection 4.3.1). Furthermore, it has been shown by simulation and experiments, that T_2-relaxation times are strongly influenced by local susceptibility changes[74]. To avoid any of the previously mentioned negative effects impairing the data quality, the magnetic susceptibility of the matrix material and the fluid inside the capillaries needed to be matched.

According to Arrighini et al.[75] the volume magnetic susceptibility of water is given by $\chi_v(\mathrm{H_2O}) = -9.035 \times 10^{-6}$. In a study by Keyser and Jefferts[76], investigating the magnetic susceptibility of materials used for apparatus construction, the volume magnetic susceptibility of 5 different epoxy resins was measured, ranging from -8.50×10^{-6} to -9.98×10^{-6}. This indicates that some of the measured epoxies are more diamagnetic than pure water, while some were measured to be less diamagnetic. A more recent study by Wapler et al.[77] measured the magnetic susceptibility of two epoxy resins (Epotec 201 and Araldite 2020) to be -9.646×10^{-6} and -9.697×10^{-6}, respectively. Concluding from the literature, the magnetic susceptibility varies between different types of epoxy resins, however, as described below, the magnetic susceptibility of the epoxy used for the construction of the capillary phantom (E45GB, Breddermann Kunstharze, Schapen, Germany) was determined to be more diamagnetic than demineralized water ($\chi_v(\mathrm{H_2O}) > \chi_v(\mathrm{E45GB})$). As it is difficult to alter the magnetic susceptibility of the epoxy, the magnetic susceptibility of the water was adapted instead. A simple means of doing so is by solving an appropriate amount of sodium chloride in water, which decreases its magnetic susceptibility to the desired value. The appropriate sodium chloride concentration was determined as follows.

Magnetic field inhomogeneities arising from susceptibility changes will result in localized phase variations of spins during an MRI measurement. Thus, information about the magnetic field inhomogeneity, and therefore about local susceptibility changes, can be obtained from phase maps generated from the complex-valued MRI-signal[78] of gradient-echo pulse sequences. A dedicated phantom was built for phase imaging, consisting of a cylindrical epoxy core (diameter 15 mm, height 50 mm) enclosed by a cylindrical body (diameter 77 mm, height 55 mm) fillable with the respective sodium chloride solution. Phase imaging was performed on a 3-Tesla clinical MRI scanner (Magnetom Skyra, Siemens Healthineers, Erlangen, Germany) using a 15-channel knee coil. A 3D gradient-echo pulse sequence[37] was employed with a sufficiently long echo time of $TE = 40$ ms to allow for a pronounced phase evolution caused by the susceptibility variations. Other sequence parameters were: slice thickness 2 mm; $TR = 50$ ms; acquisition matrix 256×192; FoV 256×192 mm²; flip angle 30°. The cylindrical phantom was filled with the respective sodium chloride solution and subsequently placed upright inside the imaging coil. Sodium chloride

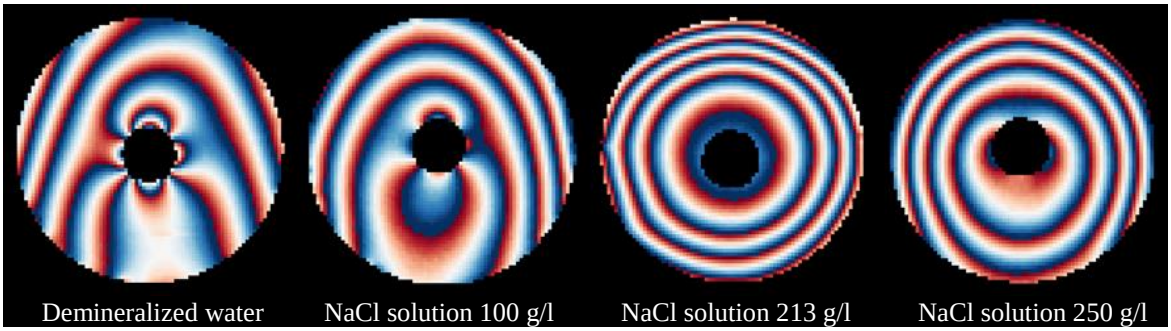

Figure 6.7: Phase maps visualizing differences in the magnetic susceptibility of the epoxy core and the surrounding sodium chloride solution. Using pure demineralized water led to strong disturbances at the interface between the water and the epoxy core, which attenuated as the sodium chloride concentration was increased. At a concentration of 213g NaCl/l, no disturbances were discernible; higher concentrations re-introduced local phase effects.

solutions between 0 g NaCl/l and 300 g NaCl/l were used for the measurement series. After imaging, coronal slices through the vertical axis at the center of the phantom were visually assessed (Figure 6.7). Using pure demineralized water, the phase maps show an obvious disturbance at the interface between the water and the epoxy core (since the epoxy core yields no MRI signal, the phase maps show only noise which was blanked out in Figure 6.7). As the sodium chloride concentration was increased, the phase disturbances attenuated. Solving sodium chloride in water decreases its magnetic susceptibility, indicating that the epoxy is more diamagnetic than pure water. An optimum concentration, where phase disturbances were not discernible, was found at 213 g NaCl/l. Further increasing the concentration induced local phase effects once more, indicating that the solution was now more diamagnetic than the epoxy.

The determined optimum solution was filled into a syringe (diameter approx. 10 cm) and subsequently analyzed in terms of the relaxation times T_1 and T_2 as well as the ADC. For the T_1 relaxometry, an inversion-recovery fast low-angle-shot (FLASH) sequence[79] was used with the following sequence parameters: $TR/TE = 5000\ \text{ms}/1.57\ \text{ms}$; flip angle $\alpha = 12°$; voxel size $0.6 \times 0.6 \times 5\ \text{mm}^3$; inversion recovery durations $TI = 300,\ 400,\ 600,\ 800,\ 1000,\ 1500,\ 2000,\ 3000,\ 4000$ ms. T_1 was determined by fitting the model $S(TI) = S_0\left(1 - 2\exp(-TI/T_1)\right)$ to the measured signal intensities yielding a T_1 of 2.71 ± 0.05 s. For the T_2 relaxometry, a spin-echo sequences with varying echo times TE were employed: $TR = 3800$ ms; voxel size $0.6 \times 0.6 \times 5\ \text{mm}^3$; $TE = 10,\ 500,\ 1000$ ms. By fitting the model $S(TE) = S_0\left(\exp(-TE/T_2)\right)$ to the measured signal intensities, a T_2 of 1.25 ± 0.18 s was determined. In line with the literature[80], both T_1 and T_2 are shortened due to the high concentration of NaCl compared to pure water with $T_1 = 5$ s and $T_2 = 3.1$ s at 3T according to Rohrer et al[81]. However, the T_2 relaxation appears to be long enough to have no significant impact on image quality in terms of a reduced signal-to-noise ratio. The apparent diffusion coefficient at room temperature was measured using a spin-echo single-shot sequence with EPI readout, monopolar diffusion gradients (3 orthogonal directions) and the following sequence parameters: $TR/TE = 3000\ \text{ms}/65\ \text{ms}$; voxel size $1.25 \times 1.25 \times 10\ \text{mm}^3$; diffusion-weightings: $b = 5,\ 10,\ 15,\ 20,\ 30,\ 45,\ 60,\ 80,\ 110,\ 150,\ 200,\ 280,\ 400,\ 600,\ 800\ \text{s/mm}^2$. The measured signal intensities were used to fit the model

$S(b) = S_0\big(\exp(-b \cdot ADC)\big)$, yielding an ADC of $1.63 \pm 0.01 \times 10^{-3}\,\mathrm{mm^2/s}$. The measured ADC demonstrates a reduced self-diffusion of the water molecules compared to pure water ($D_{H2O} = 2.023 \times 10^{-3}\,\mathrm{mm^2/s}$ at $20°C$[82]), and the determined value is in accordance with previously published literature[80,83–85].

6.4 MRI Phantom Characterization with Static Fluid

After the capillary phantom was filled with the determined sodium chloride solution, the inlet and outlet were closed to perform MRI in the absence of flow. It should be noted that the matrix material does not yield any MRI signal due to an extremely fast T_2-relaxation process; any measured signal can therefore be attributed solely to the sodium chloride solution. As before, imaging was performed using a 3-Tesla clinical MRI scanner (Magnetom Skyra, Siemens Healthineers, Erlangen, Germany). The capillary phantom was placed inside a 16-channel wrist coil; however, due to the small dimensions of the phantom it was positioned near the third coil element containing 8 channels (Figure 6.8), the remaining coil elements were not used for imaging. Additionally, since the total volume of H_2O inside the phantom is small, two foot-ankle phantoms (Siemens Healthineers, Erlangen, Germany) were placed around the wrist coil to allow for a better determination of the proton resonance frequency of the MRI system.

Figure 6.8: Setup inside of the MRI scanner. The capillary phantom was placed near the third coil element of a 16-channel wrist coil. Additional foot-ankle phantoms were placed around the upper part of the coil to facilitate the determination of the proton resonance frequency.

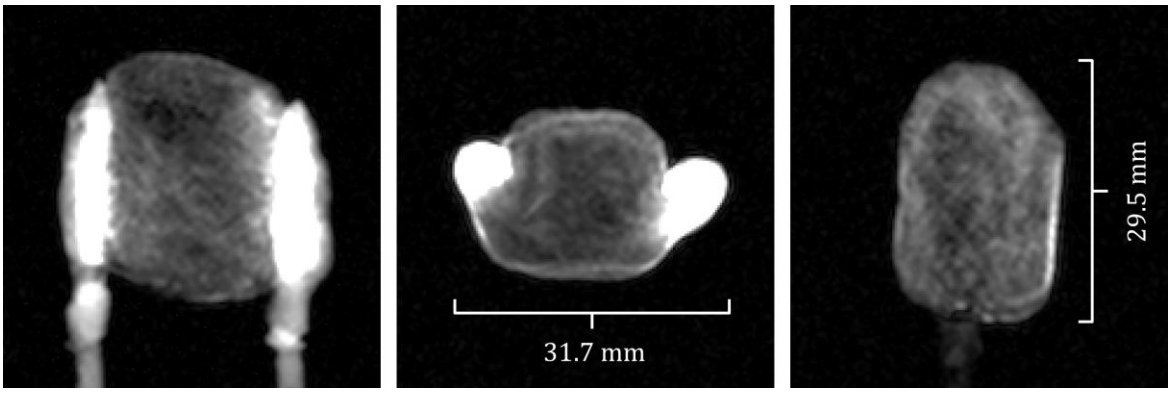

Figure 6.9: Coronal, axial and sagittal views through the capillary phantom using a fast low-angle shot (FLASH[86]) sequence.

Figure 6.9 shows coronal, axial and sagittal views through the phantom using a fast low-angle-shot (FLASH[86]) sequence ($TR/TE = 11\,\text{ms}/4.5\,\text{ms}$; flip angle $\alpha = 20°$; reconstructed voxel size $0.27 \times 0.27 \times 8\,\text{mm}^3$). The macro-channels serving as in- and outlet demonstrate high SNR. Between them, the capillary network is situated, yielding lower signal intensity since the matrix material is taking up most of the volume.

6.4.1 Relaxometry

For the subsequent T_1 and T_2 relaxometry as well as all DW-MRI experiments, imaging was performed in the sagittal plane, yielding a similar view as shown in Figure 6.9 on the right. This orientation was chosen to ensure that the signal in the analyzed image was coming solely from the solution inside the capillary network excluding the macro-channels.

As described in the previous section, inversion-recovery FLASH sequences were used for T_1 relaxometry ($TR/TE = 5000\,\text{ms}/2.82\,\text{ms}$; flip angle $\alpha = 12°$; voxel size $2.34 \times 2.34 \times 7\,\text{mm}^3$; inversion-recovery times $TI = 400, 800,\ 1500, 3000, 4500\,\text{ms}$.) and spin-echo sequences were used for T_2 relaxometry ($TR = 3800\,\text{ms}$; voxel size $2.34 \times 2.34 \times 7\,\text{mm}^3$; $TE = 10,\ 100,$

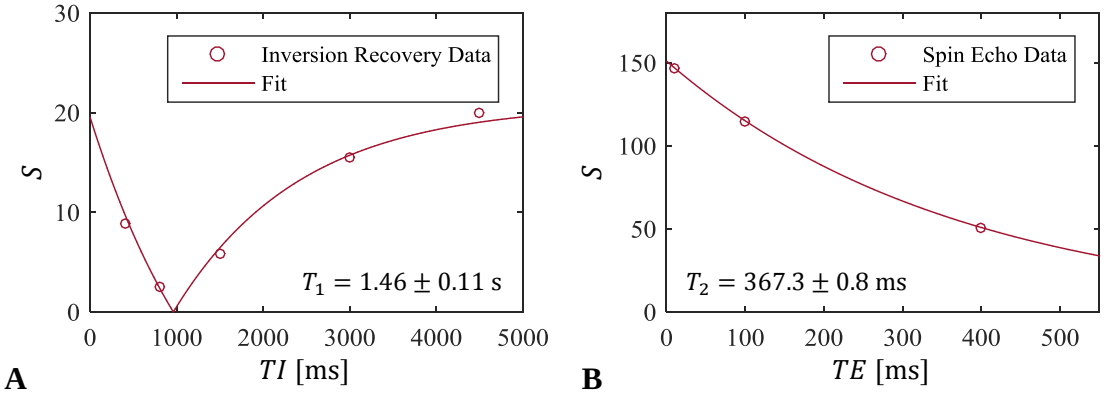

Figure 6.10: T_1 and T_2 relaxometry of the sodium chloride solution inside the capillary network. **A:** Using inversion recovery FLASH sequences with varying inversion times TI a T_1 of 1.46 ± 0.11 s was estimated. **B:** Spin-echo sequences with varying echo times TE yielded a T_2 of 367.3 ± 0.8 ms.

400 ms). Figure 6.10 displays the measured signal intensities (averaged inside a region of interest covering the entire cross section of the capillary network) and the respective fitted decay models. The determined T_1 was 1.46 ± 0.11 s and T_2 was 367.3 ± 0.8 ms. Both, T_1 and T_2 are shortened when measured inside the capillary network compared to the values determined in the syringe (see previous section), most likely due to magnetization transfer effects[87,88]. However, the shortened relaxation times did not constitute an issue for DW-MRI in terms of reduced SNR due to premature T_2 relaxation.

6.4.2 DW-MRI

For DW-MRI inside the capillary phantom, a single-shot EPI sequence was employed using the sequence parameters stated in the previous section (section 6.3) except for the voxel size, which was increased to $5 \times 5 \times 7\ \mathrm{mm}^3$ because of the low proton density. Figure 6.11 shows the measured signal intensities (again cross section averaged) as a function of the applied diffusion weighting and the respective model fits. Aside from the regular monoexponential ADC model in panel A, in panel B the kurtosis model

$$S(b) = S_0\left(\exp\left(-b \cdot D_K + \frac{b^2}{6} \cdot {D_K}^2 \cdot K\right)\right) \tag{6.4}$$

was fitted to the signal decay, yielding the kurtosis K and an adjusted diffusion coefficient D_K. In freely diffusing homogenous liquids, the probability distribution function (PDF) of the particle displacement during the diffusion experiment is Gaussian, leading to a strictly monoexponential signal decay as a function of the diffusion weighting b. However, a particle's diffusive motion may be restricted by obstacles such as cell membranes or, in the present case, the matrix material, reducing the mean squared particle displacement (i.e., reducing the variance of the PDF) as well as leading to a non-Gaussianity of the particle displacement PDF. The kurtosis model introduces a dimensionless statistical metric K to attribute for the degree of the non-Gaussianity of the particle displacement PDF[89]. The ADC measured in the capillary phantom of just $1.26 \pm 0.01 \times 10^{-3}\ \mathrm{mm}^2/s$ is markedly reduced compared to the value determined in the previous section inside of the syringe ($1.63 \pm 0.01 \times 10^{-3}\ \mathrm{mm}^2/\mathrm{s}$). Evidently, the diffusion of the water molecules inside the capillary system is restricted by the capillary walls. Using the kurtosis model an adjusted diffusion coefficient of $D_K = 1.34 \pm 0.01 \times 10^{-3}\ \mathrm{mm}^2/s$ and a kurtosis of $K = 0.49 \pm 0.04$ was determined, in line with the notion of restricted diffusion. Inferring from panel A, the monoexponential model may appear to fit the data well and the deviation from a monoexponential decay are small, however, by using the kurtosis model the residual sum of squares RSS was reduced approximately tenfold from 31.05×10^{-5} to 2.76×10^{-5}.

While the use of the kurtosis model in the no-flow case is reasonable and the improvement of the goodness of fit apparent, for the analysis of the DW-MRI experiments with flow (chapter 7) the kurtosis was not taken into account to reduce the number of model parameters. Since the non-Gaussianity of the particle displacement PDF depends on the diffusion duration, the kurtosis can only be determined with respect to the timing of the applied diffusion gradients. For the experiments in chapter 7, multiple sequences with varying diffusion-gradient timings were employed and

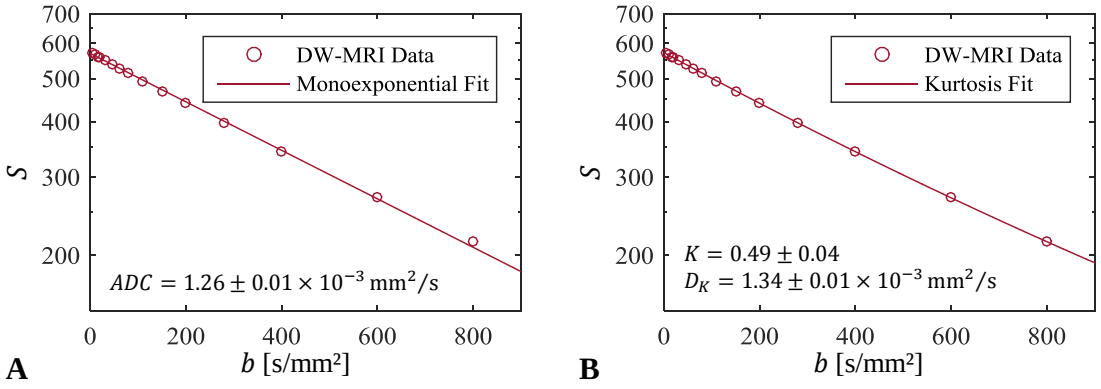

Figure 6.11: Measured signal intensities and diffusion model fits. **A:** While the monoexponential ADC model appears to describe the measured data well, the reduced ADC of $1.26 \pm 0.01 \times 10^{-3}$ mm²/s indicates restriction of the thermal diffusion by the capillary walls. **B:** The kurtosis model, accounting for the non-Gaussianity of the particle displacement PDF, reduces the residual sum of squares RSS approximately tenfold, yielding $D_K = 1.34 \pm 0.01 \times 10^{-3}$ mm²/s and $K = 0.49 \pm 0.04$.

analyzed using a joint model. Incorporating the kurtosis into the model thereby inflates the amount of model parameters significantly, leading to possible overfitting and overall parameter estimation instability[90]. Furthermore, the effect of the non-Gaussianity of the thermal diffusion on the signal decay is small within the measured b-value range compared to the effects of the applied flow. As will be shown in chapter 7, flow within the capillary system leads to a rapid loss of signal as a function of the diffusion weighting even at moderate flow velocities, so that the non-Gaussianity of the thermal diffusion is secondary.

To probe the isotropy of the capillary orientations alongside optical microscopy, a diffusion tensor imaging (DTI, section 4.2) experiment was performed. In the previous paragraph, it was concluded from the ADC measurement that the thermal diffusion within the capillary system is measurably restricted by the matrix material. Due to the cylindrical geometry of the capillaries with $l \gg d$, one may hypothesize that the restriction mainly occurs along the direction perpendicular to the respective capillary orientation. A highly anisotropic distribution of the capillary orientation should therefore be recognizable by yielding a large FA. For the DTI measurement, a single-shot EPI sequence with 12 diffusion gradient directions at $b = 1$ s/mm² and $b = 1600$ s/mm² (3 averages each), $TR/TE = 4000$ ms/71 ms and voxel size $5 \times 5 \times 8$ mm³ was used. The fractional aniso-tropy was determined in each voxel (see Figure 6.12) and averaged within the imaged cross section yielding $FA = 0.110 \pm 0.028$ (mean ± standard deviation). It should be noted that the presence of image noise generates an upward FA bias in systems with low anisotropy[91–93]. While the determined fraction anisotropy does not equate 0, it is therefore small enough to support the notion that the overall capillary orientation can be considered isotropic, as inferred from optical microscopy. For comparison, FA values in healthy white matter, where diffusion is highly anisotropic, range typically from 0.4 up to 0.7, while in gray matter, where diffusion is considered to be largely isotropic, FA values between 0.1 and 0.2 are reported[94–96].

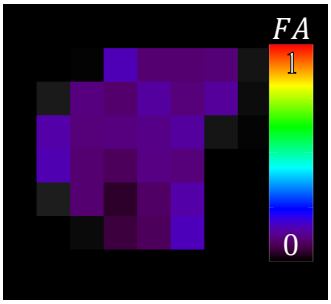

Figure 6.12: Fractional anisotropy map within the capillary phantom yielding $FA = 0.110 \pm 0.028$ (mean $\pm$ standard deviation within cross section).

7 Experimental Assessment of Flow-Dependent IVIM-MRI

As stated in chapter 6, the constructed capillary phantom was equipped with Luer-Lock connectors to allow for the application of controlled flow through the network while performing IVIM-MRI experiments. A detailed description of the experimental setup and procedure of the flow-dependent measurements is given in section 7.1, followed by a detailed analysis and discussion of the obtained results in section 7.2 with respect to the following hypothesis:

- If present, the relative volumes of multiple compartments are independent of the applied flow rate (subsection 7.2.1).
- The thermal diffusion coefficient D is independent of the applied flow rate (subsection 7.2.1).
- The measured data complies with the phase-distribution (PD) model using the deduced particle speed distribution $\rho_{\mathrm{CN}}(v)$ (subsection 7.2.2).
- The determined average particle speed $\langle v \rangle$ is linearly proportional to the applied flow rate (subsection 7.2.3).
- Linear regression of the determined particle speed $\langle v \rangle$ and the applied flow rate yields a y-axis intercept of 0, i.e. there is no constant bias (subsection 7.2.3).
- The determined capillary length l is independent of the applied flow rate, i.e. the characteristic time τ until a directional change occurs is inversely proportional to the applied flow rate (subsection 7.2.3).
- The determined capillary length l is in accordance with the average capillary length obtained using optical microscopy (subsection 7.2.3).
- A comparison with results obtained by using the IVIM model yields results in accordance with the simulations in section 5.5 (subsection 7.2.4).

For the sake of notational simplicity, the estimated average particle speed $\langle v \rangle$ will be denoted as v in the remainder of this chapter.

7.1 Methods

Subsection 7.1.1 describes the experimental setup outside of the scanner bore, facilitating the application of controlled flow through the capillary network, followed by details about the used MRI parameters and settings in subsection 7.1.2. Deviations between the nominal and actual b-values, taking image-formation gradients into account, were corrected for as depicted in subsection 7.1.3, prior to the analysis of the acquired images, described in subsection 7.1.4.

7.1.1 Experimental Setup

In addition to the MRI setup details given in section 6.4, for the following experiments the capillary phantom was connected to a syringe, filled with the determined sodium chloride solution (see section 6.3), via the Luer-Lock adapters before positioning it inside the wrist coil (see Figure 7.1). A syringe pump (Standard Infuse/Withdraw PHD 2000 Syringe Pump, Harvard Apparatus, Cambridge, Massachusetts, USA) was then used to generate precise (accuracy $\pm 0.35\%$, stated by the vendor) flow at varying rates through the capillary network during MRI. Note that instead of a single extension, as depicted schematically in Figure 7.1, three MR contrast agent tubes (Spectris Solaris MRI Integral "T" with Check Valve, Medrad, Warrendale, Pennsylvania, USA) were connected in series to provide the length needed to reach the MRI bore center with the pump stationed outside the scanner room (extensions placed through wall outlet). A large nearby reservoir of the NaCl solution allowed for a seamless refilling of the syringe in between measurements using a feed line connected to the system via t-valve. Before each measurement, the entire system was visually inspected for air bubbles and vented if necessary.

According to the manufacturer specifications, the syringe pump can generate a pressure of approximately 60 psi (4.14 bar) with regard to the syringes used for the experiments (BD Perfusion 50 ml Syringe with Luer-Lock tip, Becton Dickinson, Franklin Lakes, New Jersey, USA). The syringe pump does not offer a pressure measurement during application; however, the available clinical MR contrast agent injector (Medrad, Bayer AG, Leverkusen, Germany) provides this feature. In a preparatory experiment, the phantom was connected to this injector in the same fashion as described above. Subsequently, the maximum flow rate of 2.4 ml/s used for the IVIM experiments was applied while logging the pumping pressure. Initially increasing, a constant pressure of

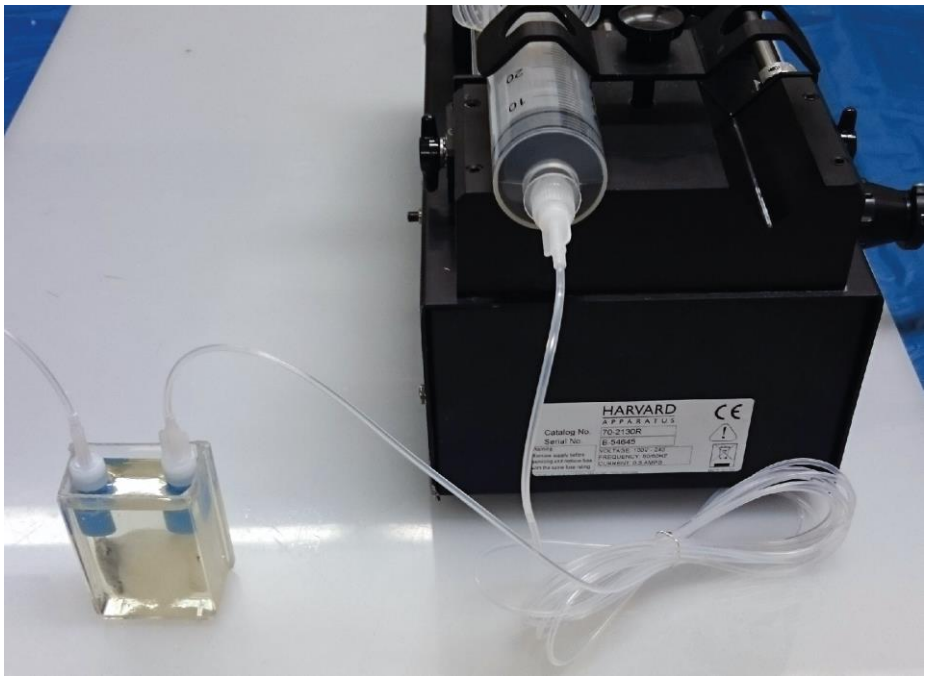

Figure 7.1: Schematic picture of the capillary phantom connected to a syringe. The syringe is placed inside the pumping mechanism of a Harvard Apparatus syringe pump to generate precise flow through the phantom at varying rates during DW-MRI.

33 psi was reached after approximately 5 minutes of constant pumping. This is well below the pressure that can be generated by the syringe pump as well as the approved pressure for the contrast agent tubes (350 psi). Consequently, for all flow-dependent experiments, imaging was delayed by at least 5 minutes after starting the pump to ensure constant pressure and flow during the measurement. Note that the MR injector system was not used for the imaging experiments since it only allows for relatively large step sizes of 0.6 ml/s for the flow rates.

7.1.2 MR Imaging

After completing the setup and proper positioning of the phantom inside the scanner, imaging was initiated using a localizer scan. Based on the localizer images, sagittal DW-MRI was planned as described in section 6.4. Additionally, saturation regions were placed on top of the macro channels to avoid inflow effects[97] and unwanted contributions to the measured MRI signal. Flow rates ranging from 0.2 ml/min to 2.4 ml/min, increasing in increments of 0.2 ml/min, were applied while performing the DW-MRI experiments. For each flow rate, all sequences listed in Table 5.1 were employed. The (nominal) b-value sampling scheme followed $b = 0;\ 5;\ 10;\ 15;\ 20;\ 30;\ 45;\ 60;\ 80;\ 110;\ 150;\ 200;\ 280;\ 400;\ 600;\ 800\ \mathrm{s/mm^2}$, however, the FC11 sequence only sampled a reduced b-value interval (see Table 5.1) to achieve shorter diffusion gradient durations. The diffusion-sensitizing gradients were applied in three orthogonal directions, specifically in the read (through-bore), phase (vertical) and slice (right-left) direction. Further sequence parameters were TR = 3000 ms; TE variable (see Table 5.1), voxel size $5 \times 5 \times 7\ \mathrm{mm^3}$; matrix size 64×64, field of view $230 \times 230\ \mathrm{mm^2}$, parallel imaging factor 2 (GRAPPA), 3 signal averages. All flow rates of a series were measured in one session with a total duration of approx. 10 hours.

7.1.3 b-Value Correction

Restating the equation from chapter 4, the diffusion weighting or b-value of an MRI pulse sequence is given by

$$b = \gamma^2 \int_0^{TE} \left(\int_0^t \boldsymbol{g}(t')dt' \right)^2 dt. \tag{7.1}$$

As discussed in chapter 3, image formation in MRI utilizes pulsed magnetic field gradients for slice selective excitation and refocusing as well as in-slice spatial encoding. Consequently, an MRI pulse sequence is inherently attributed with a non-zero b-value. The DW-MRI sequences (provided by Siemens Healthineers, Erlangen, Germany) used for the experiments in this chapter offer the possibility to acquire an image with a b-value of $0\ \mathrm{s/mm^2}$. Upon inquiry, it was confirmed by the pulse sequence authors that the image formation gradients might not be properly factored into the calculation of the diffusion weighting. Furthermore, at nominal $b = 0\ \mathrm{s/mm^2}$, additional crusher gradients are played out during the pulse sequences to prevent the formation of unwanted stimulated echoes. As the size of the diffusion-sensitizing gradients falls below a certain threshold, they are removed and replaced by the crusher gradients as well.

The deviations in the diffusion weighting caused by these issues are usually small and of negligible consequence in a clinical setting. However, the analysis of the diffusion-weighted experi-

ments performed in section 7.2 requires a particularly high accuracy with respect to the b-values. This is especially true for very small b-values, as the initial signal decay is rapid at high flow rates and a precise sampling in this range is essential for robust parameter estimations. Furthermore, diffusion experiments with long durations, such as the MP171 sequence, potentiate the effects on the inaccuracy of the b-values. To address this issue, the nominal b-values were replaced with b-vales obtained through simulation of the MRI pulse sequence and subsequent application of eq. (7.1). For the simulations, a dedicated computer running the IDEA software (Siemens Healthineers, Erlangen, Germany) was set up. Source codes for the pulse sequences were supplied as part of a research agreement. The simulations were run using the exact same sequence settings as used for the actual diffusion experiment (copied via the MRI scanner export tool). The gradients employed throughout the sequences were exported and subsequently used to calculate the b-values according to eq. (7.1) in Matlab (The MathWorks, Natick, Massachusetts, USA). The echo time *TE* was determined at the readout of the k-space center. For the STEAM pulse sequences, the aforementioned introduction of crusher gradients at $b = 0\ \mathrm{s/mm^2}$ leads to significant deviations from the nominal b-value depending on the duration of the specified steam time (interval between 90° STEAM pulses). Thus, the $b = 0\ \mathrm{s/mm^2}$ images of the STEAM pulse sequences were excluded from the analysis.

7.1.4 Data Analysis

All analyses of the acquired DICOM images were done using Matlab (The MathWorks, Natick, Massachusetts, USA). For each image, the signal in the capillary network was (arithmetically) averaged inside regions of interest (ROI) based on thresholding of the least diffusion-weighted image of the respective sequence. Averaging signal intensities inside very heterogeneous ROIs, for example covering different tissue types such as brain matter and cerebral spinal fluid, may affect parameter estimates when models with multiple compartments are fitted[19,98,99]. However, the homogenous structure of the sugar-fiber ball transferred to the molded capillary network, displaying a homogenous signal behavior in the imaged cross section. A threshold of more than 30 times the standard deviation of the background noise ensured that only voxels with strong signal from the capillary network were included in the ROI. The resulting ROIs consisted of approx. 30 voxels. As mentioned in the previous section, the diffusion-weighted gradients were applied in the read, phase and slice directions. Generally, the analysis of non-directional parameters (as opposed to the fractional anisotropy, for example) is done using trace-weighted images, which can be calculated by averaging three orthogonal diffusion directions using the geometric mean. However, the data acquired using diffusion gradients in the slice direction were excluded from the analysis to avoid effects of macroscopic flow as explained in the following paragraph.

The imaged slice is oriented sagittally between the two macro-channels of the phantom; therefore, the slice direction corresponds to the direction of the macroscopic pressure gradient from inlet to outlet. Consequently, there will be a net flow in slice direction and the resulting particle movement will not fully conform to the random walk model established in section 4.4., which serves as basis of the IVIM theory. Over the course of the data analysis it will be shown that the measured signal decay is fitted best by a two-compartment model (subsection 7.2.1), where a second, non-flowing compartment is hypothesized to stem from NaCl solution inside the spherical dilations described in section 6.2. A macroscopic net flow along the diffusion gradient direction

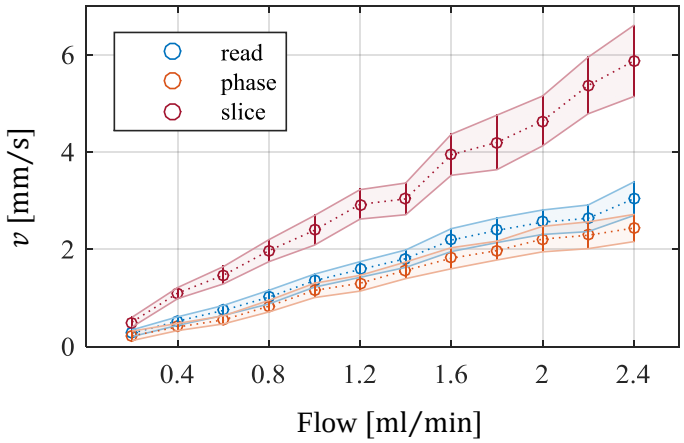

Figure 7.2: Estimated average particle speed v at varying rates of flow. The three diffusion-gradient directions (read, phase and slice) were analyzed separately. Noticeably faster particle speeds in slice direction are apparent compared to the read and phase directions. As the slice direction aligns with the macroscopic pressure gradient from inlet to outlet, this directional dependency is likely caused by a macroscopic net flow in slice direction. Error bars and shaded areas indicate the 95% confidence interval, determined as $\pm 1.96 \cdot$ standard error.

introduces additional dephasing between the flowing and stagnant compartment as well as intra-compartmental dephasing, since the macroscopic flow is likely to be spatially dependent (i.e. not bulk motion). Consequently, the signal decay as a function of the diffusion weighting will be further accelerated when applying the diffusion gradients in the slice direction, compared to the read and phase directions. This can be demonstrated by anticipating some results from the parameter estimation when the individual gradient directions were analyzed separately: At an applied flow rate of 2 ml/min an average particle speed of 4.6 ± 0.3 mm/s was determined using gradients in the slice direction, while the read and phase directions yielded 2.6 ± 0.1 mm/s and 2.2 ± 0.1 mm/s, respectively. Other flow rates show a similar trend as illustrated in Figure 7.2.

In DW-MRI experiments, the signal attenuation is only affected by motion along the diffusion gradient direction. Consequently, experiments using gradients in the read and phase directions are not susceptible to aforementioned adverse effects of the macroscopic net flow. The particle movement pattern in the read-phase plane should entirely be dictated by the randomness of the capillary network. To minimize the effect of the macroscopic pressure gradient and the associated net flow, the measurement data using diffusion gradients in the slice direction was therefore excluded from the following analysis. The measured signal intensities from the read and phase directions were averaged using the geometric mean to improve the SNR, to generate (semi) directionally independent parameter estimates and to allow for a straightforward presentation of the obtained results.

Deviations from the nominal *b*-values were accounted for by calculating the arithmetic average of the determined actual *b*-values from the two remaining gradient directions (see subsection 7.1.3). The estimation of the model parameters follows the description in section 5.3 if not specified otherwise.

7.2 Results and Discussion

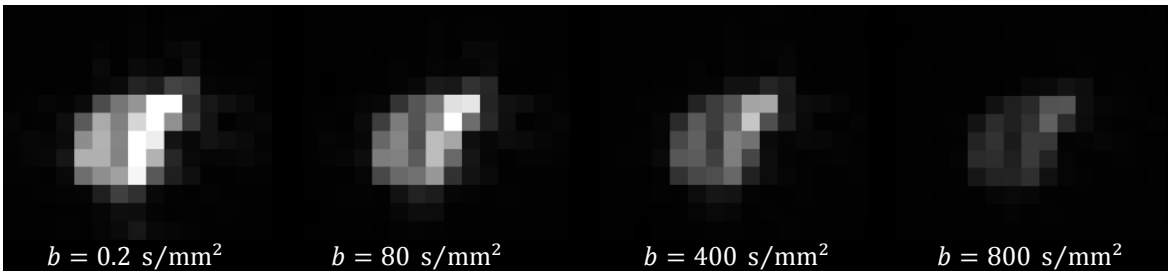

Figure 7.3: Exemplary diffusion-weighted images of the capillary phantom using the MP28 sequence at an applied flow rate of 1.2 ml/min.

Exemplary diffusion-weighted images of the capillary phantom using the MP28 sequence at an applied flow rate of 1.2 ml/min are shown in Figure 7.3 displaying a high SNR. The capillary network appears distorted in the phase-encoding direction (left-right in presented image orientation), an artifact common to single-shot EPI sequences. The large difference in the magnetic susceptibility of the epoxy and the surrounding air leads to an inhomogeneous magnetic field around the boundary, resulting in a "misplacement" of nearby signal in the reconstructed image[72]. The signals of multiple imaging voxels are placed on top of each other, creating localized areas of high signal intensity. However, the distortions are independent of the diffusion weighting and therefore of no consequence to the quantitative analysis of the signal decay.

Figure 7.4 illustrates signal intensities $S(b)$ on a reduced b-value range (up to $200\,\mathrm{s/mm^2}$), measured using the sequences MP28 (monopolar diffusion gradients) and FC11 (flow-compensated diffusion gradients) at varying rates of flow. As the flow rate increases, the initial signal decay at small b-values accelerates, however, the effect is much more pronounced for the monopolar diffusion gradients. Apparently, the flow-compensated diffusion gradients suppress much of the flow-induced signal decay indicating that the particles are mostly performing a linear motion and do not undergo, on average, many directional changes during the diffusion experiment. Indeed, even at the highest flow rate, there is a marked difference between the pictured signal decays.

In the following, a detailed quantitative analysis of the measured data using the phase-distribution (PD) model introduced in section 4.4 and an interpretation of the results is presented. In subsection 7.2.1, the presence of two compartments, one flowing and one static, will be the subject of discussion, followed by the assessment of the derived particle speed distribution $\rho_{\mathrm{CN}}(v)$ in subsection 7.2.2. The effects of the varying flow rates on the signal model fits and the resulting parameter estimates as well as the reproducibility will be discussed in subsection 7.2.3 and lastly a comparison to the results obtained using the biexponential pseudo-diffusion model will be made in subsection 7.2.4.

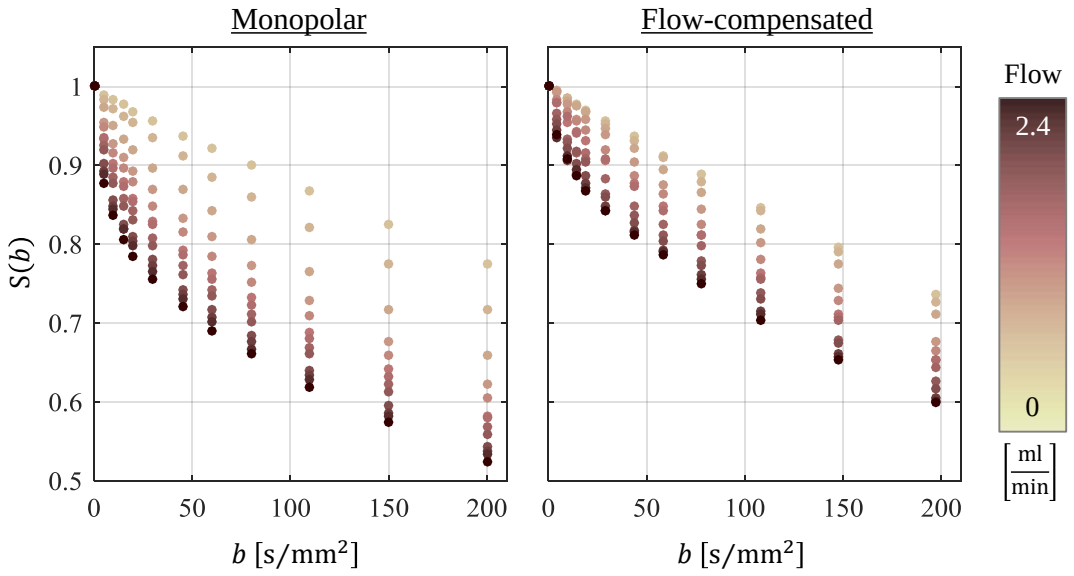

Figure 7.4: Signal intensities $S(b)$ on a reduced b-value range (up to $200\,\mathrm{s/mm^2}$), measured using the sequences MP28 (monopolar diffusion gradients, left) and FC11 (flow-compensated diffusion gradients, right) at varying rates of flow. The signal measured using the monopolar diffusion gradients displays a greatly accelerated decay at small b-values compared to the flow-compensated gradients, indicating that the particles do not undergo many directional changes due to capillary flow during the diffusion experiment.

7.2.1 1-Compartment vs 2-Compartment Model

Initially, the measured signal intensities were analyzed using a model comprising of a single, flowing compartment:

$$S_{1c}(b) = S_0 e^{-bD} \cdot F[\boldsymbol{x}(t), \boldsymbol{g}(t)], \tag{7.2}$$

where F is based on the generated normalized phase distributions ρ_{ϑ_h}.However, as illustrated in Figure 7.5, the model fit is lacking, especially at higher flow rates. The residual sum of squares (RSS) shows a strong dependency on the applied flow rate and the residuals appear to display a systematic pattern. The introduction of a second, static compartment to the model (albeit sharing the molecular diffusion coefficient D with the flowing compartment):

$$S_{2c}(b) = S_0\left(f \cdot e^{-bD} \cdot F + (1-f) \cdot e^{-bD}\right), \tag{7.3}$$

shows a profound improvement of the model fit. Furthermore, the RSS remains largely constant over the whole range of the applied flow rates.

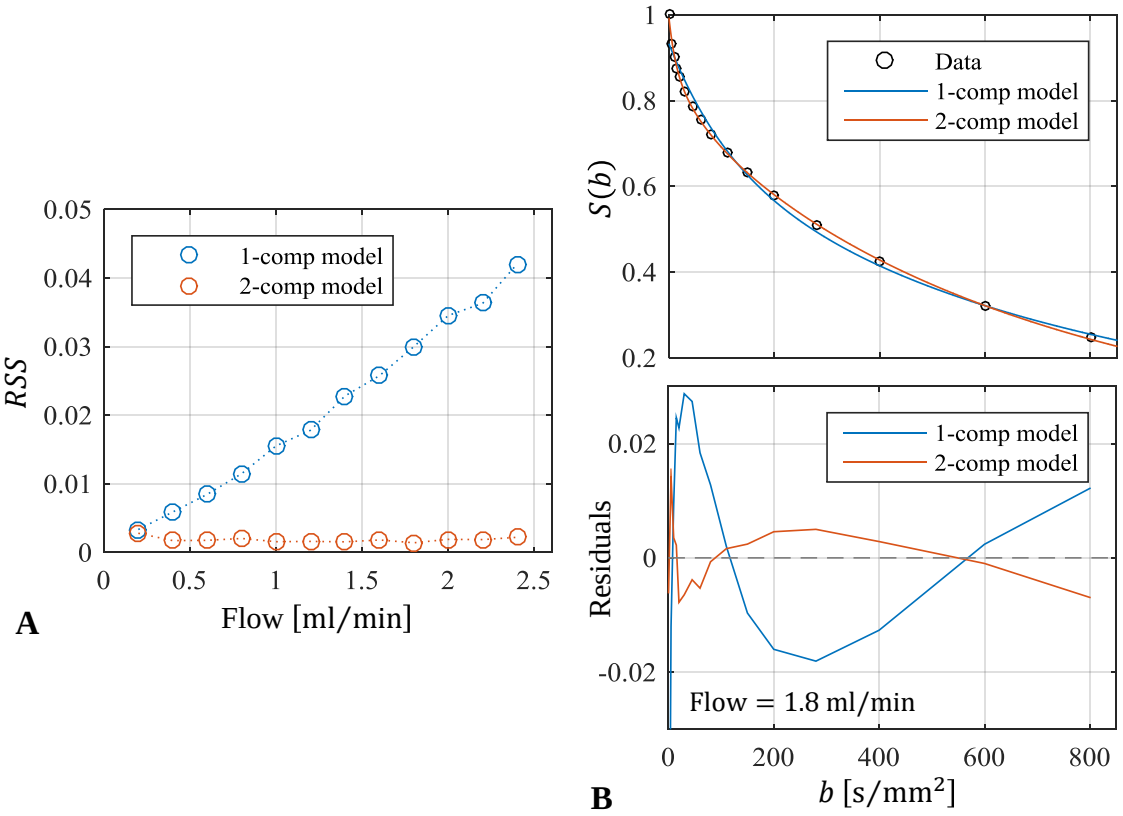

Figure 7.5: Comparison of the model fits using a single, flowing compartment (1-comp model) and a model comprising of a flowing and an additional static compartment. In panel **A**, the residual sum of squares (RSS) is plotted versus the applied flow rate. The RSS of the 1-compartment model displays a strong dependency on the applied flow rate, while the RSS of the 2-compartment model is appreciably smaller and remains largely constant. Panel **B** shows an exemplary model fit at an applied flow of 1.8 ml/min (top) and the residuals between the model fit and the measurement data (bottom, only data for sequence MP28 is displayed). The 2-compartment model fits the measured data closely, whereas the 1-compartment model deviates clearly in a systematic pattern.

Introducing additional parameters to a model almost always results in an improved fit to the measured data. The Akaike information criterion[100] represents a measure to quantify this improvement by considering the RSS_i of model i in relation to the number of model parameters k_i and the number of available measurement points n:

$$AIC_i = 2k_i + n\log\left(\frac{RSS_i}{n}\right) + \frac{2{k_i}^2 + 2k_i}{n - k_i - 1}. \tag{7.4}$$

A smaller AIC indicates a more appropriate model. The calculated AIC_i can also be used to obtain the corresponding weight W_i, yielding a relative probability for the appropriateness of model i [90]. Using this procedure to compare the single-compartment vs two-compartment model at an exemplary applied flow rate of 1.8 ml/min, the respective weights are $W_{1c} = 3.5 \times 10^{-38}$ and $W_{2c} \approx 1$, indicating that the two-compartment model is more appropriate with very high certainty. The AIC clearly favors the two-compartment at all applied flow rates apart from 0.2 ml/min, where

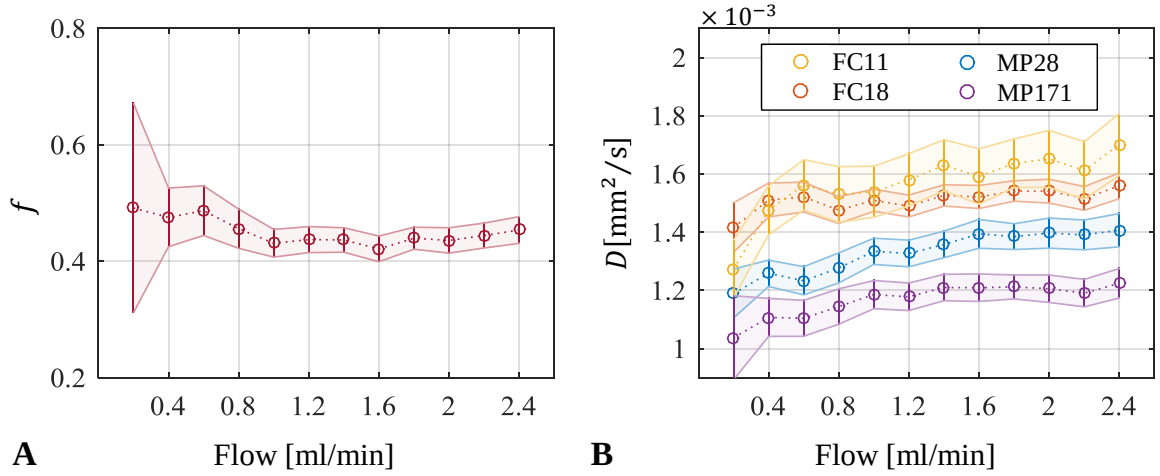

Figure 7.6: Parameter estimates for the signal fraction f attributed to flowing particles and estimates for the molecular diffusion coefficients D. The fraction f initially shows a high degree of inaccuracy but evens out at around 0.451 ± 0.023 (mean ± sd of all flow rates) as the flow rate increases. The diffusion coefficients display a consistent behavior, with an initial increase followed by levelling off at higher flow rates and appear ordered due to restricted-diffusion effects.

flow-induced dephasing is marginal. It should be noted that the residuals using the two-compartment still show a systematic pattern (see subsection 7.2.4). The reason for this is most likely a deviation of the actual statistical distribution of particle speeds from the applied approximation $\rho_{\mathrm{CN}}(v)$.

Figure 7.6 A illustrates the estimated fraction of the signal f attributed to the flowing compartment as well as the molecular diffusion coefficient D versus the applied flow rate. The fraction f initially shows a high degree of inaccuracy, owed to the very slow particle speed, making it difficult to separate flowing from static fraction. As the flow rate increases, the estimates even out at around 0.451 ± 0.023 (mean $\pm$ sd of all flow rates). This value is appreciably close to the ratio of the volume inside the capillaries V_{cap} to the total network volume $V_{cap} + V_{dil}$, estimated using the data obtained from optical microscopy (see section 6.2) to be 0.454 ± 0.002. It thus stands to reason that the non-flowing compartment can be ascribed to liquid inside the spherical dilations (as well as eventual dead-end capillaries, to a smaller extend). Furthermore, given the constant behavior of f at larger flow rates is in line with the anticipation that the relative volumes of multiple compartments are independent of the applied flow rate.

As is evident from optical microscopy, the spherical dilations are connected to the capillary network; however, applying flow through the phantom seems to have limited effect on the particle motion inside the dilations (Figure 7.6 B). Note that the varying diffusion times of the different sequences mandate the inclusion of sequence-respective molecular diffusion coefficients D_i into the model to accommodate for the varying degrees of restricted-diffusion effects. Hence, each model fit yields four diffusion coefficients.

The estimated molecular diffusion coefficient D_{MP28} increases to some extend with the flow rate and levels off around $1.4 \times 10^{-3}\,\mathrm{mm^2/s}$. The increase of D_{MP28} at the highest flow rate compared to the measurement without flow, where the ADC was estimated to be $1.26 \times 10^{-3}\,\mathrm{mm^2/s}$ (measured using the MP28 Sequence as well, see subsection 6.4.2), is about 11%.

Furthermore, the fastest estimated D_{MP28} of $1.407 \times 10^{-3}\,\mathrm{mm^2/s}$ is still decidedly slower than the determined ADC of the freely diffusing NaCl solution of $1.68 \times 10^{-3}\,\mathrm{mm^2/s}$. The remaining diffusion coefficients show a similar trend; however, the effects of restricted diffusion come into display: The MP171 sequence, with its long diffusion preparation time, is most susceptible to the restriction of the water molecules' Brownian motion in the capillary phantom and yields the smallest diffusion coefficients, followed by the MP28 sequence. FC11 has the shortest diffusion time, resulting in the largest diffusion coefficients, above the estimated coefficients of FC18. Due to the reduced b-value sampling interval, D_{FC11} displays rather large errors compared to the other sequences.

Concluding from the presented results, the hypothesis that the molecular diffusion coefficient D is independent of the applied flow rate is not readily confirmed. Two processes are likely to cause the observed behavior of D:

- **Reduced restriction in the static compartment.** As was reasoned above, the flowing compartment consists of a network of cylindrical channels, while the static compartment consists of spherical dilations with comparatively large diameters. The effects of restriction of the measured diffusion coefficient using DW-MRI is mainly dependent on the surface-to-volume ratio of the enclosing structure[101], which is given by $S_\mathrm{c}/V_\mathrm{c} = (2r + 2h)/(rh) \approx 2/r$ for (long) cylinders and by $S_\mathrm{s}/V_\mathrm{s} = 3/r$ for spheres. A larger ratio leads to lower measured diffusion coefficients. The average dimensions determined using optical microscopy (see section 6.2) yield surface-to-volume ratios of $364\,\mathrm{mm^{-1}}$ and $96\,\mathrm{mm^{-1}}$ for the cylinders and the spheres, respectively, indicating reduced restriction effects in the spherical dilations. As the applied flow rate increases, the flowing compartment is growingly dominated by dephasing effects due to capillary flow. The resulting signal decay is exceedingly fast compared to the decay attributed to molecular diffusion. Consequently, the slowly decaying, static compartment will have a stronger weight on the determined value of D and the reduced restriction effect in the spherical dilations thus leads to higher estimates. Note that fitting separate diffusion coefficients for the flowing and static compartment was not practicable due to the resulting excessive amount of model parameters.
- **Turbulences and drifts inside the static compartment.** While there is an absence of directional flow, adjoining capillaries may still evoke turbulences and drifts in the spherical dilations, which will reflect on the estimated diffusion coefficients.

7.2.2 Comparison of Speed Distributions

In section 5.1, the L-shaped statistical distribution $\rho_{\mathrm{CN}}(v)$ of particle speeds in the capillary-network was motivated. In this section, the signal model fits to the data using $\rho_{\mathrm{CN}}(v)$, delta-distributed, and uniformly distributed particle speeds will be compared. In Figure 7.7 A, the resulting RSS values are plotted versus the applied flow rate. At slow flow rates, where the dephasing due to flow is not as prominent, all speed distributions result in small RSS values, however, a distinct improvement by using $\rho_{\mathrm{CN}}(v)$ over uniformly and especially delta-distributed speeds is already apparent. This is further accentuated as the flow rate increases, with the RSS of both delta and uniformly distributed particle speeds showing a strong dependency on the applied flow rate. In

contrast, using $\rho_{\mathrm{CN}}(v)$ the RSS is approximately constant over the entire flow rate spectrum at an appreciatively small level. The boxplot, summarizing the RSS values of all applied flow rates for each particle speed distribution, highlights the low variability and the superiority of the model fits using $\rho_{\mathrm{CN}}(v)$. Panel B shows exemplary model fits at an applied flow rate of $1.2\ \mathrm{ml/min}$. Note that only the signal and respective fitted models for the MP28 sequence are illustrated; however, all data of the four sequences were used for the model fits. Furthermore, a limited b-value range is displayed ($\leq 300\ \mathrm{s/mm^2}$) to highlight the fast signal decay due to flow. The model fit using delta-distributed particle speeds deviates clearly from the measured data and shows the characteristic sinc-like decay (see section 5.2), which was not observed in any of the performed experiments. The model fit using uniformly distributed particle speeds greatly improves upon this, however, upon close examination, there are still obvious deviations between measured data and model fit, which show a systematic pattern and can therefore not be explained by signal noise alone. Using $\rho_{\mathrm{CN}}(v)$, those deviations are visibly reduced and the model fit follows the measured data more closely. While it is apparent that $\rho_{\mathrm{CN}}(v)$ offers a distinct improvement over uniformly and delta-distributed particle speeds, the resulting residuals still show a systematic pattern (see subsection 7.2.4 for further illustrations), albeit to a greatly reduced extent. The reason for this is likely a remaining discrepancy between $\rho_{\mathrm{CN}}(v)$ and the true underlying particle speed distribution, which may follow a more complex and irregular shape. However, the appreciably close fit of the data as well as the fact, that the RSS does not show a dependence on the applied flow rate, indicates that $\rho_{\mathrm{CN}}(v)$ is indeed a reasonable approximation of the true particle speed distribution.

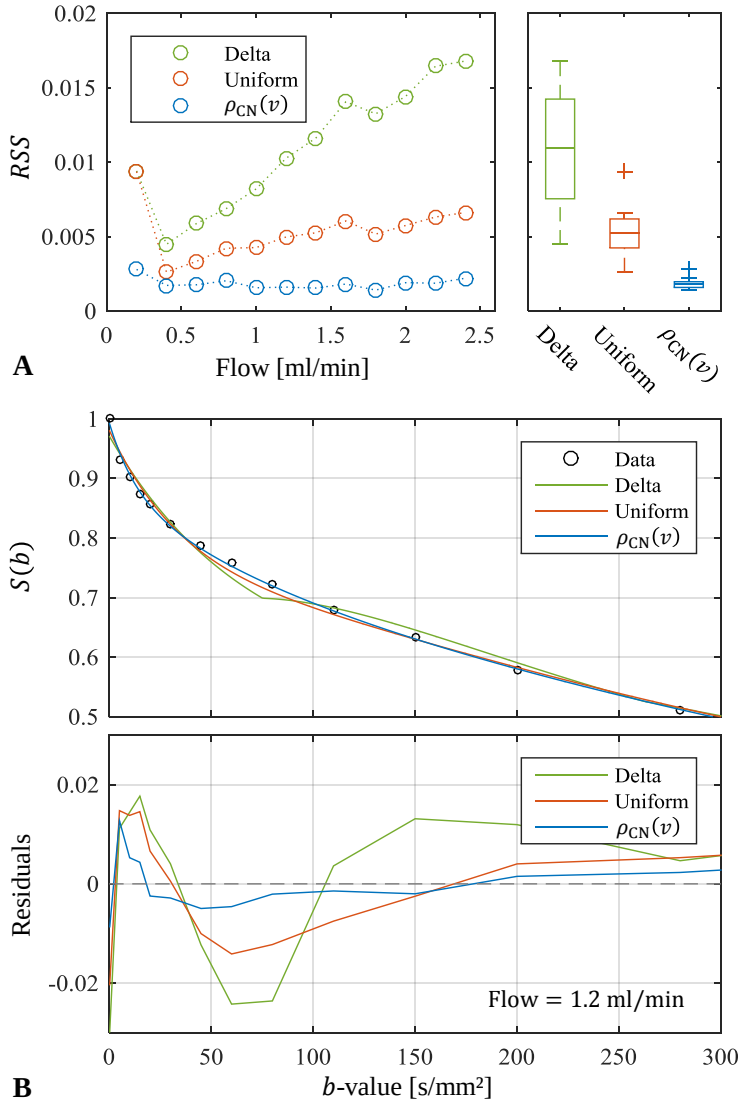

Figure 7.7: Comparison of the goodness of the signal model fit using a delta-shaped particle speed distribution, a uniform distribution, and $\rho_{CN}(v)$. Panel **A** shows the *RSS* for each distribution versus the applied flow rate. The delta-distribution exhibits the largest *RSS* with an obvious correlation to the flow rate. The uniform distribution improves upon this; however, using $\rho_{CN}(v)$ provides a further distinct reduction of the *RSS* values and eliminates the flow rate dependency. Panel **B** shows an exemplary model fit (top) and the residuals between model fit and measurement data (bottom) at a flow rate of 1.2 ml/min (only data of sequence MP28 shown on a reduced *b*-value range: $b \leq 300$ s/mm^2). Using the delta distribution results in the characteristic sinc-like decay, which is not reflected by the measured data and thus results in a poor model fit. Both the uniform distribution and $\rho_{CN}(v)$ represent the data much better with $\rho_{CN}(v)$ yielding the closest model fit.

7.2.3 Analysis of Flow Dependency

In this section, a more detailed analysis of the effects of the varying flow rates on the signal model fits and the resulting parameter estimates is presented. Furthermore, two measurement series performed on different days will be compared to assess the reproducibility of the estimates.

Figure 7.8 illustrates measured signal intensities and the respective model fits at exemplary flow rates. Note that even though the sequences are colored individually, at each flow rate only a single model fit was performed, incorporating the data of all four sequences. In general, the phase-distribution model fits the measured data well as the fitted curves closely follow the measurement points. At an applied flow rate of 0.6 ml/min, the data measured using non-flow-compensated diffusion gradients (MP28 and MP171) already exhibit a fast signal decay at low b-values compared to the sequences FC18 and FC11, which still follow an approximately mono-exponential

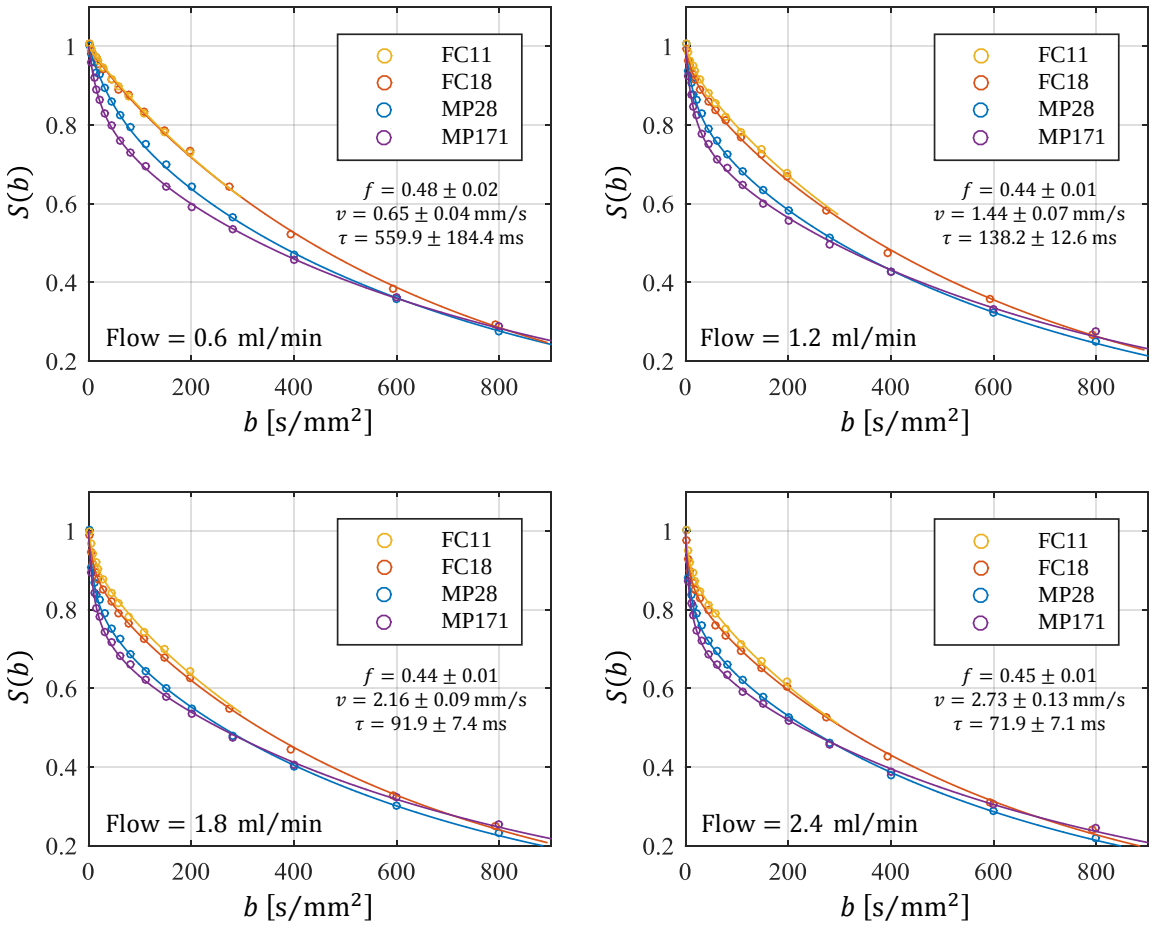

Figure 7.8: Measured signal intensities and the respective model fits at exemplary flow rates. In general, the signal model fits the measured data well as the fitted curves closely follow the measurement points. At an applied flow rate of 0.6 ml/min the sequences FC18 and FC11 compensate the flow-induced dephasing almost completely. Accordingly, the estimated τ (the average flow duration within a single cylindrical segment) is very long, albeit with a high degree of uncertainty. The initial decay at low b-values steepens with increasing flow rate and the dephasing effect becomes clearly visible in the flow-compensated data as well.

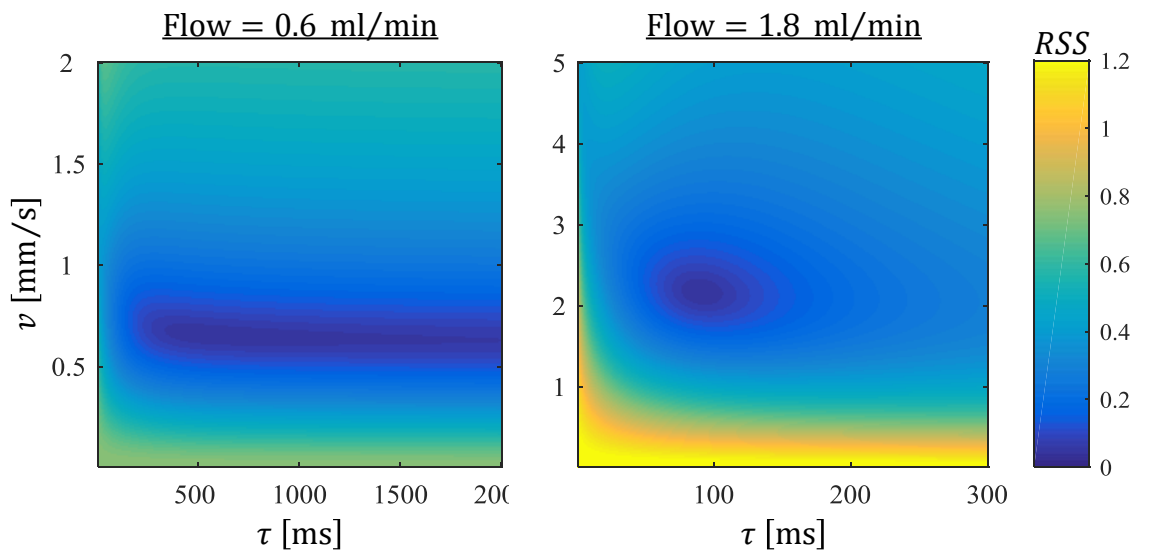

Figure 7.9: RSS as a function of v and τ for flow rates of 0.6 ml/min and 1.8 ml/min. At 0.6 ml/min the RSS takes on the shape of an elongated trench parallel to the τ-axis, indicating a large uncertainty in the estimated value. At 1.8 ml/min the RSS demonstrates a convex shape with a distinct global minimum, yielding appreciably small relative errors of 4.2% and 8.1% for v and τ, respectively.

decay curve. Thus, at this flow rate the particles do not seem to change their movement direction often during the diffusion experiment due to capillary flow and, accordingly, the estimated τ (the average dwell duration within a single cylindrical segment) is rather long with 560 ± 184 ms. In this case, the estimated error for τ is large, owed to the fact that τ is much longer than the duration of the diffusion gradients of all four sequences, thereby limiting the estimation accuracy (see section 5.4). As the applied flow rate increases, the initial decay at low b-values steepens and the dephasing effect becomes clearly visible in the flow-compensated data as well. Accordingly, the estimated average particle speed v increases, while τ decreases and f stays approximately constant.

The difficulty of accurately estimating τ at small flow rates is further exemplified in Figure 7.9. At an applied flow rate of 0.6 ml/min the residual sum of squares RSS as a function of v and τ takes on the shape of an elongated trench parallel to the τ-axis. Accordingly, the RSS remains close to minimal for a wide range of τ, resulting in a large relative error of 32.9%. In contrast, the RSS function at an applied flow rate of 1.8 ml/min demonstrates a distinct convex shape with an obvious global minimum at $v = 2.2$ mm/s and $\tau = 92$ ms and estimated relative errors of 4.2% and 8.1%, repectively.

A comprehensive illustration of the obtained results is presented in Figure 7.10, where each estimated parameter and its respective 95% confidence interval (calculated as $\pm 1.96 \times se$) is plotted versus the applied rate of flow for the two measurement series A and B, performed on different dates. All parameter estimates and errors are listed in Table 7.1 as well.

As anticipated above, the fraction of the signal f attributed to flowing particles shows large uncertainties at low flow rates, especially noticeable in series A, due to the difficulty of separating flowing from static fraction at slow particle speeds.

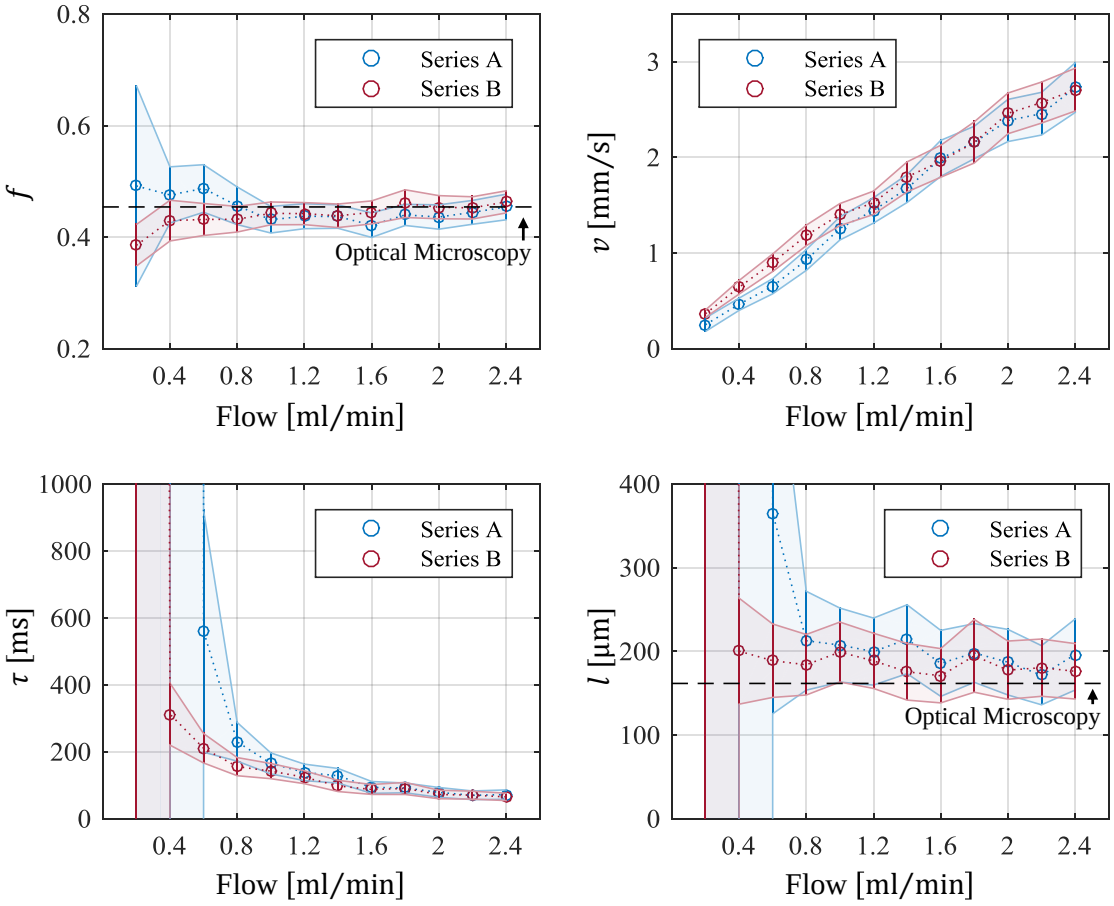

Figure 7.10: Estimated parameters and respective 95% confidence intervals (calculated as $\pm 1.96 \times se$) versus the applied rate of flow for two measurement series A and B (performed on different dates). The estimates for f and τ show large uncertainties and variability at slow flow rates, however, for flow rates of ≥ 1 ml/min the confidence intervals are appreciably small, with f remaining largely constant and τ showing an inverse proportionality to the applied flow rate. The estimates for f closely match the ratio of the volume inside the capillaries to the total network volume of $V_{\text{cap}}/(V_{\text{cap}} + V_{\text{dil}}) = 0.454$ determined using optical microscopy (dashed line). The estimated average particle speed v shows a linear proportionality to the applied rate of flow with narrow confidence intervals. The average capillary segment length calculated via $l = v \times \tau$ remains approximately constant at flow rates of ≥ 1 ml/min and is close to the average segment length of 162 µm determined using optical microscopy (dashed line).

For flow rates of ≥ 1 ml/min the confidence interval is appreciably small and the estimates show little variability with an average of 0.438 ± 0.009 and 0.449 ± 0.009 ($mean \pm sd$, flow rates ≥ 1 ml/min) for measurement series A and B, respectively. The estimated average particle speed v shows a linear proportionality to the applied rate of flow and increases from 0.25 ± 0.03 to 2.73 ± 0.13 mm/s, respectively 0.36 ± 0.02 to 2.71 ± 0.11 mm/s, over the course of the measurement series. The characteristic duration τ suffers from poor accuracy at slow flow rates and is the parameter that is most difficult to estimate accurately, as the average relative standard errors for flow rates ≥ 1 ml/min are 9.3% and 8.8% for measurement series A and B, respectively. Nonetheless, the confidence intervals and the estimated parameters appear reasonable, allowing

one to calculate the average capillary segment length via $l = v \times \tau$. With v showing a linear proportionality and τ being inverse proportional to the applied rate of flow, the resulting l remains approximately constant at flow rates of ≥ 1 ml/min with an average estimated length of 195 ± 13 µm and 183 ± 10 µm ($mean \pm sd$, flow rate ≥ 1 ml/min) for measurement series A and B, respectively. In comparison, the average capillary length determined using optical microscopy (see section 6.2) is 162 ± 78 µm and is therefore 14 % shorter than average length estimated using DW-MRI. A possible source of this bias is the missing depth-information using optical microscopy. The measured segment lengths are not taking any possible propagation of the capillaries in and out of the image plane into consideration, leading to a bias towards smaller values. Nonetheless, the length of 162 µm estimated using microscopy is still within the 95% confidence interval of the length obtained by DW-MRI for the majority of flow rates.

The average number of directional changes M due to flow during the diffusion experiment differs between the employed gradient profiles (as they also differ in duration T). With regard to the gradient profile MP28 ($T = 50.4$ ms), which is most comparable to commonly performed in vivo IVIM measurements, M increases from less than 0.01 to 0.70, respectively less than 0.01 to 0.78, for the two measurement series. Considering that the particle speeds are actually following a distribution and that the maximum speed is six time the average speed (see subsection 5.1.2), the fastest flowing particles change their movement directions up to 4.2 times, respectively 4.7 times during the MP28 diffusion experiment.

As can be appreciated in Figure 7.10, the results from the two measurement series are in good agreement, excluding flow rates of < 1 ml/min. To quantify the agreement, the coefficient of variation[102,103] (CV) was calculated via

$$CV(\%) = 100 \times \frac{SD}{\text{Mean}}, \tag{7.5}$$

with the standard deviation $SD = \sqrt{\left(\sum_{i=1}^{n}(x_{A,i} - x_{B,i})^2\right)/2n}$, $\text{Mean} = \sum_{i=1}^{n}(x_{A,i} + x_{B,i})/2n$, and the number n of estimate pairs x_1 and x_2. Including all applied flow rates, the CVs are 6.3%, 6.2%, 345% and 358% for f, v, τ and l, respectively. The poor CVs for τ and l originate from the large uncertainties at small flow rates. Excluding flow rates of < 1 ml/min yields CVs of 2.7%, 3.8%, 13.1% and 8.1%, respectively.

The linear proportionality of the estimated average particle speed v to the applied flow rate is an important feature to substantiate the plausibility of the estimated parameters. Figure 7.11 illustrates the linear regression of v (measurement series A) versus the applied flow rate. The estimated coefficient of determination is $R^2 = 0.993$ with a p-value of 2.5×10^{-12}, indicating that practically all variation in v is predictable from the applied flow rate. Furthermore, the estimated intercept at 0.034 mm/s is very close to 0 mm/s, showing that there is negligible constant bias.

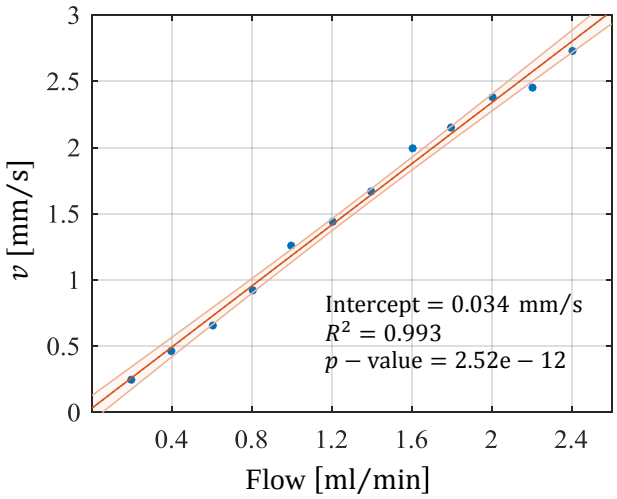

Figure 7.11: Regression analysis of v (measurement series A) versus the applied flow showing a highly significant linear proportionality with $R^2 = 0.993$ and a p-value of 2.5×10^{-12}. The estimated intercept at 0.034 mm/s indicates that there is negligible constant bias.

Table 7.1: Parameter estimates for measurement series A and B and the resulting coefficients of variation (CV) between the measurement series.

	Flow [**ml/min**]	f	v [mm/s]	τ [ms]	l [μm]	D [10^{-3}mm^2/s] (range)
Series A	0.2	0.492 ± 0.092	0.250 ± 0.036	$7.3 \times 10^6 \pm 1.2 \times 10^{11}$	$1.8 \times 10^6 \pm 2.9 \times 10^{10}$	1.038 … 1.416
	0.4	0.476 ± 0.026	0.463 ± 0.033	$7.1 \times 10^6 \pm 4.3 \times 10^{10}$	$3.3 \times 10^6 \pm 2.0 \times 10^{10}$	1.108 … 1.511
	0.6	0.487 ± 0.022	0.652 ± 0.041	559.9 ± 184.4	365.2 ± 122.4	1.104 … 1.562
	0.8	0.456 ± 0.017	0.926 ± 0.055	229.6 ± 29.5	212.6 ± 30.1	1.145 … 1.530
	1.0	0.431 ± 0.012	1.257 ± 0.062	165.1 ± 16.0	207.4 ± 22.6	1.186 … 1.539
	1.2	0.437 ± 0.014	1.445 ± 0.068	138.2 ± 12.6	199.7 ± 20.4	1.178 … 1.580
	1.4	0.437 ± 0.011	1.674 ± 0.074	128.1 ± 11.2	214.4 ± 21.0	1.210 … 1.630
	1.6	0.421 ± 0.011	1.989 ± 0.096	93.3 ± 9.1	185.6 ± 20.1	1.209 … 1.592
	1.8	0.440 ± 0.010	2.156 ± 0.087	91.9 ± 7.4	198.0 ± 17.9	1.212 … 1.637
	2.0	0.436 ± 0.011	2.385 ± 0.112	78.4 ± 7.5	187.0 ± 20.0	1.206 … 1.652
	2.2	0.444 ± 0.011	2.457 ± 0.114	69.8 ± 6.6	171.4 ± 18.0	1.191 … 1.612
	2.4	0.454 ± 0.012	2.729 ± 0.132	71.9 ± 7.1	196.1 ± 21.7	1.225 … 1.701
Series B	0.2	0.385 ± 0.019	0.365 ± 0.020	$3.7 \times 10^4 \pm 1.0 \times 10^6$	$1.3 \times 10^4 \pm 3.7 \times 10^5$	1.091 … 1.610
	0.4	0.430 ± 0.019	0.641 ± 0.036	312.3 ± 47.2	200.2 ± 32.3	1.143 … 1.633
	0.6	0.432 ± 0.015	0.898 ± 0.047	210.3 ± 22.4	188.8 ± 22.4	1.165 … 1.760
	0.8	0.432 ± 0.012	1.184 ± 0.055	155.4 ± 13.8	183.9 ± 18.5	1.198 … 1.738
	1.0	0.442 ± 0.010	1.401 ± 0.059	142.1 ± 11.6	199.1 ± 18.3	1.205 … 1.764
	1.2	0.442 ± 0.010	1.525 ± 0.062	123.7 ± 9.8	188.6 ± 16.8	1.220 … 1.734
	1.4	0.438 ± 0.011	1.796 ± 0.080	97.7 ± 8.7	175.5 ± 17.3	1.225 … 1.599
	1.6	0.444 ± 0.011	1.959 ± 0.085	87.2 ± 7.5	170.8 ± 16.5	1.216 … 1.723
	1.8	0.460 ± 0.013	2.156 ± 0.110	90.2 ± 9.2	194.6 ± 22.2	1.241 … 1.732
	2.0	0.454 ± 0.011	2.460 ± 0.109	72.1 ± 6.5	177.5 ± 17.8	1.253 … 1.724
	2.2	0.452 ± 0.010	2.573 ± 0.110	70.1 ± 6.1	180.5 ± 17.5	1.242 … 1.751
	2.4	0.463 ± 0.010	2.708 ± 0.114	65.0 ± 5.6	176.1 ± 16.9	1.240 … 1.737
	CV	6.26 %	6.22 %	344.6 %	358.2 %	
	CV (Flow ≥ 1)	2.71 %	3.75 %	13.06 %	8.13 %	

Combined Model

In theory, the fraction of the signal f attributed to flowing particles as well as the capillary segment length l are characteristic features of the capillary network and should not show any dependency on the applied flow rate. So far, for each flow rate, a separate model fit was performed and indeed, f as well as l remained largely constant once the applied flow rate is high enough to allow for accurate parameter estimations. Alternatively, one may formulate a combined minimization problem that incorporates the measurement points of all flow rates, effectively forcing f and l to be constant across flow rates. Figure 7.12 A illustrates the results of this combined model compared to the average estimates and standard errors of the separate model fits using the data from measurement series A. For the separate model fits, flow rates < 1 ml/min have been excluded due to the large standard errors. The separate fits yield an average capillary length of 195 µm with an average error of ± 20 µm. The combined model yields a similar estimated length of 202 µm, however, with a significantly smaller error of ± 13 µm. The signal fraction f shows a likewise trend with average $f = 0.438 \pm 0.022$ obtained from the separate fits and $f = 0.444 \pm 0.004$ from the combined model, with an even more pronounced reduction of the standard error. Figure 7.12 B shows the regression analysis of the particle speeds v obtained using the combined model versus the applied flow rate. While the separate fits already yielded a highly linear proportionality of v and the flow rate (Figure 7.11), the combined model enhances this relationship even further with an estimated coefficient of determination of $R^2 = 0.999$ and a p-value of 1.7×10^{-17}. The estimated diffusion coefficients D using the combined model (not shown) behave very similar compared to the separate fits with a range of $D = 1.07 \ldots 1.39 \times 10^{-3}$ mm^2/s at a flow rate of 0.2 ml/min, up to a range of $D = 1.26 \ldots 1.72 \times 10^{-3}$ mm^2/s at a flow rate of 2.4 ml/min.

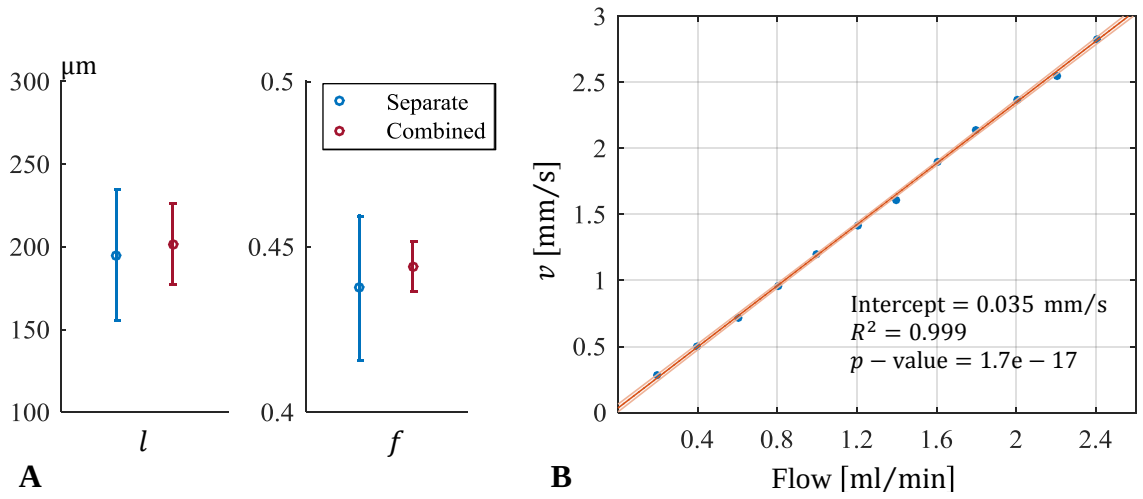

Figure 7.12: Results of a combined model, incorporating the measurement points of all flow rates into a single fit. Panel **A:** Comparison of the average estimates and errors for l and f of the separate model fits (excluding flow rates < 1 ml/min due to the large standard errors) with the combined model results. The separate fits yield $l = 195 \pm 20$ µm and $f = 0.438 \pm 0.022$, the combined model yields $l = 202 \pm 13$ µm and $f = 0.444 \pm 0.004$, greatly reducing the standard errors for both parameters. Panel **B:** Regression analysis of the particle speeds v obtained using the combined model versus the applied flow rate.

7.2.4 Comparison to Pseudo-Diffusion Model

The biexponential pseudo-diffusion model with its four parameters, the perfusion fraction f, the pseudo-diffusivity D^*, the tissue diffusivity D and the unweighted signal intensity S_0, is the preferred choice in the literature to investigate effects due to capillary flow in DW-MRI. In this section, an analysis of biexponential model fits based on the MP28 measurement data is presented and compared to the results obtained using the phase-distribution (PD) model. The MP28 sequence was chosen, since it closely reflects the sequence designs commonly used for IVIM measurements for example in the kidneys[14,16].

Figure 7.13 illustrates the estimated parameters and their respective 95% confidence interval (calculated as $\pm 1.96 \times se$) using the biexponential model, plotted versus the applied rate of flow. In line with the PD model results and the simulations performed in section 5.5, the biexponential model fails to separate the flowing from the static compartment at the lowest flow rate, reflected by a large estimated error for f. Subsequently, f increases with the applied flow rate from $f(0.4\ \mathrm{ml/min}) = 0.131$ to $f(2.4\ \mathrm{ml/min}) = 0.234$. The pseudo-diffusion coefficient D^* exhibits a strong linear relationship to the applied flow rate and increases from $D^*(0.4\ \mathrm{ml/min}) = 10.6 \times 10^{-3}\ \mathrm{mm^2/s}$ to $D^*(2.4\ \mathrm{ml/min}) = 80.7 \times 10^{-3}\ \mathrm{mm^2/s}$. The diffusion coefficient D of the static compartment shows a distinct dependency of the applied flow rate as well, increasing from $D(0.4\ \mathrm{ml/min}) = 1.41 \times 10^{-3}\ \mathrm{mm^2/s}$ to $D(2.4\ \mathrm{ml/min}) = 1.68 \times 10^{-3}\ \mathrm{mm^2/s}$. Close examination of the biexponential model fit at an exemplary flow rate of $1.6\ \mathrm{ml/min}$ reveals systematic deviations between the measured data and the fitted curve (further analyzed in Figure 7.15).

A direct comparison of the signal fractions f, the particle speeds v and the molecular diffusion coefficients D estimated using the different models is shown in Figure 7.14. For the biexponential model, the particle speed was calculated via $v = 6D^*/l$, whereby a capillary length of $l = 202\ \mu\mathrm{m}$ was used (as determined in the previous section using the combined PD model). Both f and v illustrate similar behaviors to the results obtained in section 5.5: The biexponential estimates for f are much lower than the estimates obtained using the PD model, however, the estimates for v show a reasonable agreement between the two models. In line with the simulation results, it appears that applying an inadequate signal model has the most negative effect on the signal fraction f. The estimates for v are associated with comparatively large errors, which is partly due to the reduced number of measurement points but likely also originates from the inadequacy of the biexponential model function and the resulting poor model fit. The molecular diffusion D is estimated consistently higher when using the biexponential model compared to the PD model. This is likely due to the interaction between f and D: As the biexponential model underestimates the fraction of flowing particles f, the rapid signal decay is not fully accounted for by the pseudo-diffusion D^*, and is in turn compensated by overestimating the molecular diffusion coefficient D.

A detailed analysis of the residuals and goodness of fits is presented in Figure 7.15. Note that only the residuals from sequence MP28 are discussed here, even though the PD model fits are based on all four sequences. Panel A illustrates the fit residuals as line-plots color-coded according to the applied flow rate. In general, the PD model fit results in decidedly smaller absolute values of the residuals, which is most prominent at high flow rates. Furthermore, the residuals of both models show contributions that are clearly not normally distributed and exhibit a systematic pattern. Notably, the residuals of the biexponential model in Figure 7.15 appear very much alike the residuals displayed in Figure 5.11, which were obtained by fitting the biexponential model to data

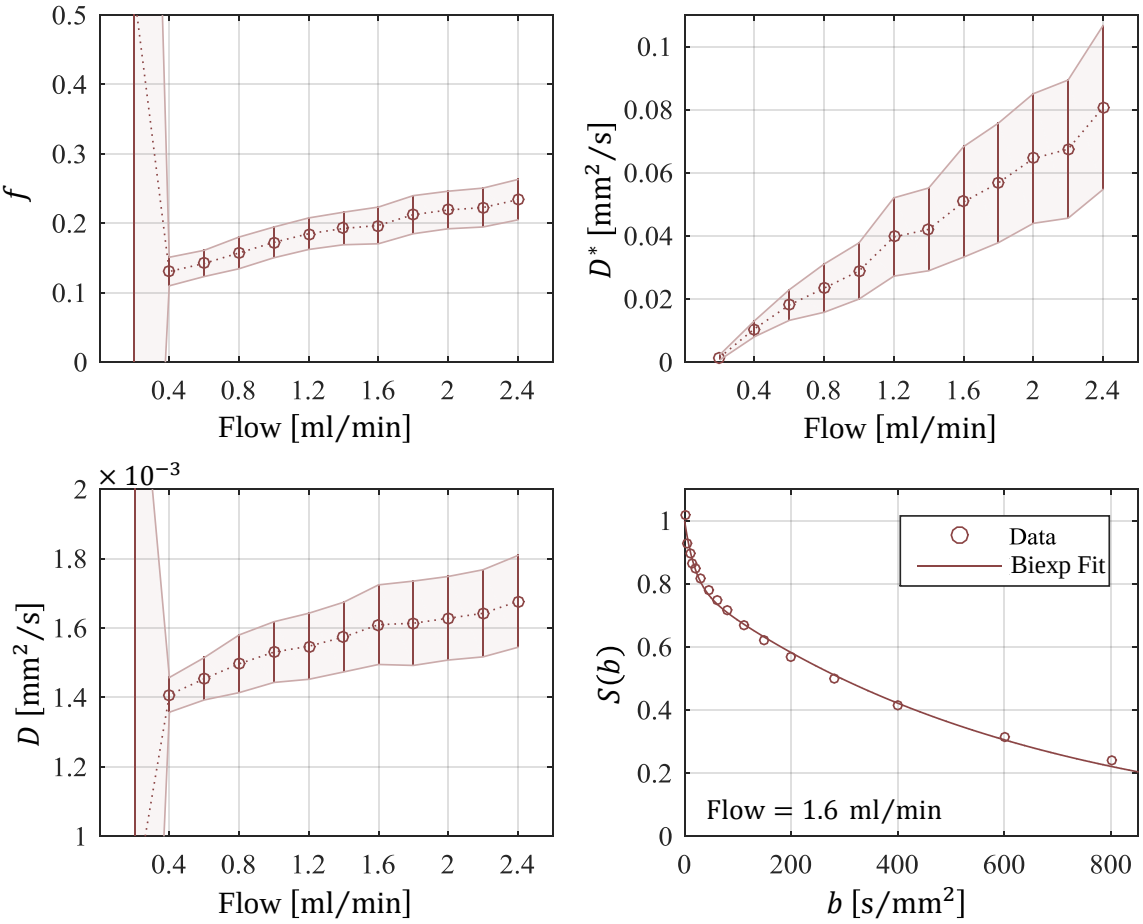

Figure 7.13: Estimated parameters and their respective 95% confidence intervals (calculated as $\pm 1.96 \times se$) using the biexponential model, plotted versus the applied rate of flow and an exemplary model fit. The biexponential model fails to separate flowing from static compartment at the lowest flow rate, reflected by a large estimated error for f. For the subsequent measurements, all parameters display a dependency on the applied flow rate. Close examination of the model fit reveals systematic deviations between the measured data and the fitted curve (further analyzed in Figure 7.15).

simulated using the PD model with the particle speed distribution $\rho_{\mathrm{CN}}(v)$. The strong resemblance of the residual pattern further indicates that $\rho_{\mathrm{CN}}(v)$ is indeed a reasonable approximation of the actual particle speed distribution inside the capillary network. However, as previously mentioned, the residuals of the PD model do show non-normally distributed contributions as well, albeit to a greatly reduced extend, indicating that there are some remaining dephasing effects, which are not properly reflected by the PD model. Panel B shows the sum of the squared fit residuals of the respective models versus the applied flow rate, highlighting the superiority of the PD model, especially at high flow rates.

Previously introduced (see subsection 7.2.1), the Akaike information criterion (AIC) and the resultant weights may be used to quantify the appropriateness of each model by relating the RSS to the number of measurement points and model parameters. While the biexponential model has four parameters, S_0, f, D^* and D, the situation is not as obvious for the PD model when only considering a single sequence, in this case MP28. Instead of D^*, the PD model has two parameters, v and

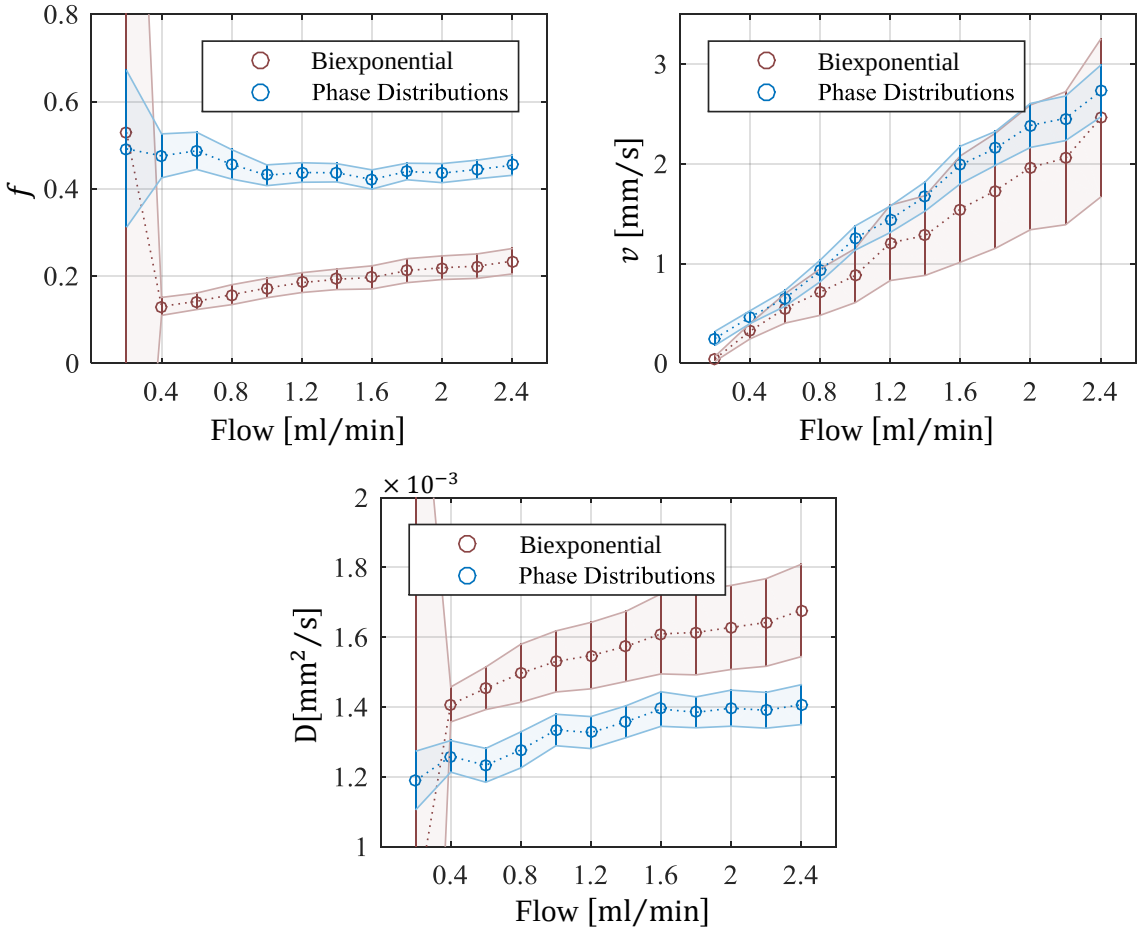

Figure 7.14: Comparison of the signal fractions f and the particle speeds v estimated using the biexponential and PD model. For the biexponential model, the particle speed was calculated via $v = 6D^*/l$, whereby a capillary length of $l = 202$ µm was used. The biexponential estimate for f is much lower than the estimate obtained using the PD model, however, the estimates for v show a reasonable agreement between the two models. The biexponential estimates for v are associated with comparatively large errors due to the reduced number of measurement points and the poor model fit. The molecular diffusion D is estimated consistently higher when using the biexponential model compared to the PD model.

τ. Although these are not truly free parameters with respect to the MP28 data fit (as they are determined with respect to the best model fit to all four sequences), they have been regarded as such for the AIC calculation. It is important to realize that the parameters S_0 and D are sequence respective in the PD model, i.e. only the S_0 and D of MP28 contribute to the number of model parameters with regard to the AIC. This is easily understandable by considering the following: The PD model can in theory solely be fit to the MP28 data, resulting in a reduced number of total model parameters and a smaller or at worst equal RSS (since v and τ are now truly free parameters with respect to the MP28 data). Furthermore, $\rho_{\mathrm{CN}}(v)$ was semi-empirically determined and depends on the shape parameter $\alpha = 0.5$. To err on the side of caution, the PD model was therefore assumed to have six parameters: α, S_0, D, f, v and τ. Figure 7.15 C shows the calculated weights at each flow rate. Since both models result in similar RSS values at small flow rates, the biexponential

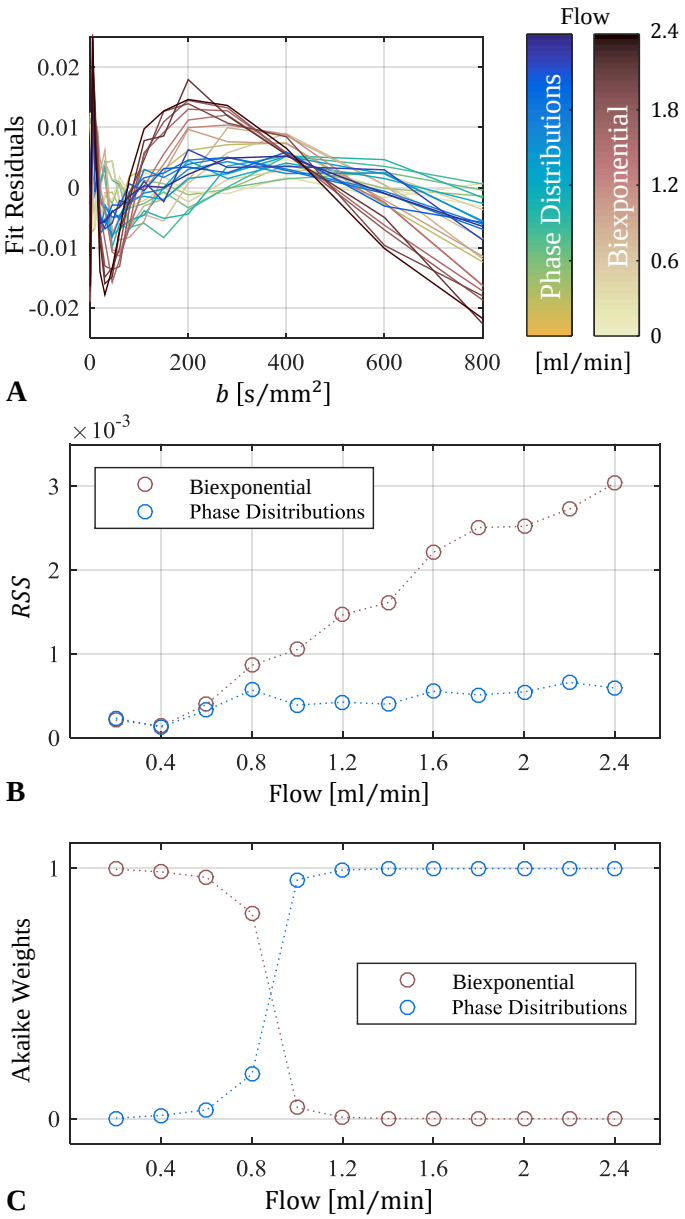

Figure 7.15: Analysis of the residuals and goodness of fits using the biexponential and PD model. **A**: The PD model results in decidedly smaller absolute values of the residuals, which is most prominent at high flow rates. Both models show contributions that are clearly not normally distributed and show a characteristic pattern. **B:** *RSS* (sum of squared fit residuals) values of the respective models versus the applied flow rate, highlighting the superiority of the PD model, especially at high flow rates. **C**: Akaike weights at each flow rate using $k = 4$ and $k = 6$ model parameters for the biexponential and PD model, respectively. Since both model fits result in similar *RSS* values at low flow rates, the biexponential model is preferred by the AIC due the smaller set of parameters. However, as the flow rate increases, the decidedly reduced *RSS* values obtained using the PD model outweighs the larger parameter set.

model is preferred by the AIC due to the smaller set of parameters. However, as the flow rate increases, the decidedly reduced *RSS* values obtained using the PD model outweighs the larger parameter set and a strong preference of the PD model becomes apparent.

8 Discussion & Outlook

In the course of this work, the capability of conventional pseudo-diffusion (biexponential) IVIM MRI and phase-distribution IVIM MRI to characterize capillary flow was investigated and compared. To this end, a phantom, facilitating flow in a capillary bed at adjustable rates, was constructed and subsequently analyzed using optical microscopy. Based on extensive DW-MRI measurement series, the potential of phase-distribution IVIM MRI to accurately estimate flow properties such as the flow speed as well as information about the capillary geometry was assessed while demonstrating the limitations of the conventional pseudo-diffusion model. Furthermore, detailed numerical simulations were performed to consolidate the experimental findings and to advance the understanding of the effects of flow characteristics on data measured using DW-MRI.

Characterizing capillary flow using IVIM MRI

The diffusion-weighted images of the capillary network acquired at different rates of flow displayed a high SNR and, paired with the ROI-based evaluation, the measured signal decay curves appeared smooth with barely any visible noise-associated jitter. Notably, there was a stark difference in the slope of the curves between the different employed gradient schemes at all applied flow rates. Having previously established that the signal decay is indifferent to the applied gradient scheme in the pseudo-diffusion limit, it can already be anticipated that the underlying particle movement does not conform to this limiting case.

Utilizing the Akaike Information Criterion (AIC), the acquired data was shown to be best described by a two-compartment model consisting of a static and a flowing compartment, where the static compartment is hypothesized to be ascribed to liquid inside the spherical dilations. The flowing compartment was fit using the phase-distribution model. In accordance with the expectation that the relative volumes of multiple compartments should be independent of the applied flow rate, the determined signal fraction f attributed to the flowing compartment stayed approximately constant over the course of the measurement series. The average signal fraction $f = 0.451 \pm 0.023$ of all flow rates from the measurement series A is appreciably close to the ratio of the volume inside the capillaries V_{cap} to the total network volume $V_{cap} + V_{dil}$, estimated at 0.454 ± 0.002 using the data from optical microscopy. This further supports the notion that the static compartment consists of the liquid inside the spherical dilations. Having a flowing and static compartment of roughly the same size benefits the detailed analysis of flow effects using DW-MRI; however, with respect to in vivo measurements, a perfusion fraction of $f = 0.451$ can be considered rather large. Values close to that have only been reported in the best-perfused organs such as the kidneys[104] or the liver[27].

In a closed system, the average particle speed due to flow must be linearly proportional to the applied rate of flow. The estimated average particle speed $\langle v \rangle$ inside the capillary phantom fully met this expectation. The calculated coefficient of determination between the applied rate of flow and $\langle v \rangle$ is $R^2 = 0.99$, indicating that practically all variation in $\langle v \rangle$ is predictable from the applied flow rate. Furthermore, there is negligible constant bias, as the estimated y-axis intercept of $0.034\ \mathrm{mm/s}$ is close to zero. The estimated average flow speeds, ranging from $\langle v \rangle = 0.25\ \mathrm{mm/s}$

up to 2.7 mm/s cover reported values from various studies. Ivanov et al.[105] measured the red cell velocity in the brain and the temporalis muscle of rats to be 0.8 mm/s and 1.1 mm/s, respectively. Pawlik et al.[71] investigated the cerebral cortex of cats and determined the median flow velocity of red cells to be 1.5 mm/s. Both of these studies used highly invasive methods where the examined tissue layers were first exposed and subsequently imaged using optical microscopy. Using a more recent and less invasive method, laser Doppler anemometry, the velocity of capillary blood cells in the cutaneous microvasculature was reported to range between 0.2 mm/s to 1.4 mm/s in patients with venous leg ulcers in a study by Stücker at al.[106]. Due to the associated difficulties, measured values of the blood flow speed in internal organs have never been reported to our knowledge. However, using their proposed phase-distribution IVIM method, Wetscherek et al.[26] estimated the speed of flow to be 4.6 mm/s and 3.9 mm/s for the liver and pancreas, respectively. In the presented work, it was not possible to reach velocities of that magnitude since the utilized pump did not provide enough pumping pressure.

At very slow flow rates, the characteristic duration τ until a particle changes its movement direction (due to the traversing of capillary segments) could not be determined with satisfactory accuracy resulting in large standard errors. At flow rates greater than 0.8 ml/min, τ showed an inverse proportionality to the applied flow rate. Consequently, the hypothesis that the capillary segment length, calculated as $l = \langle v \rangle \cdot \tau$, is independent of the applied flow rate is confirmed in this domain, serving as further basis for the validity of the applied signal model. Optical microscopy yielded an average capillary length of 162 ± 78 µm which is slightly below the values determined using DW-MRI ranging from 171 µm to 214 µm for flow rates larger than 0.8 ml/min. A possible source of this bias is the missing depth-information in optical microscopy.

Naturally, the average number of directional changes M is not only subject to the speed of flow and capillary length, but also to the duration of respective diffusion experiment. With regard to the employed sequence MP28, the average M was estimated to range between 0.01 to 0.78 in the performed experiments, which is well below the pseudo-diffusion limit. The reported range of in vivo blood flow velocities in the literature is broad, however, considering a speed of 1 mm/s and a capillary length[70] of 63 µm, a directional change can be expected to occur every 63 ms. The diffusion gradients in the MP28 sequence have a total duration of $T = 50.4$ ms, accordingly, these in vivo values would translate to $M = 0.8$, also well below the pseudo-diffusion limit. Especially at the higher applied flow rates, the estimated values of M correspond very well to this approximation and the performed phantom measurements can therefore be considered a reasonable representation of this aspect.

The measured data was analyzed using the biexponential pseudo-diffusion IVIM model as well; however, the RSS values vastly increased in comparison to the phase-distribution model at flow rates larger than 0.8 ml/min indicating that the pseudo-diffusion limit was not reached even at the highest flow rate. At slow flow rates, the reduced parameter set of the biexponential model outweighs the reduction in RSS, yet, as the flow rate increases the perfusion effects become more dominant and the AIC clearly favors the phase-distribution model. Using the biexponential model, the signal fraction f was estimated to be much smaller (ranging from 0.13 to 0.23) but displayed a strong increase with the applied flow rate compared to the phase-distribution model estimate. Yet,

translating the pseudo-diffusion D^* to the particle speed v_{biexp}, the estimates from both models display a good agreement. These findings are in accordance with the results of the simulation study; they highlight the intricate interplay of the model parameters and show that the accuracy of the estimated signal fraction f is highly susceptible to correct model assumptions. This is especially interesting with regard to the common notion that D^* is most difficult to estimate accurately, suffering heavily in the presence of signal noise and insufficient b-value sampling[59].

IVIM-MRI phantom studies

To our knowledge, this work represents the first time IVIM-MRI experiments were performed using a perfusable phantom consisting of a three-dimensional microchannel network similar to in vivo capillary beds, and it was the first time that the phase-distribution model was investigated using phantom measurements. As the most important property, an IVIM-MRI phantom must facilitate incoherent particle motion within the scale of a single imaging voxel. This can be achieved in a number of ways, for example using sponges or columns packed with microspheres. However, these approaches create mostly turbulent flow and lack the capillary structure needed to assess phase-distribution IVIM. Creating a three dimensional network on the scale of in vivo capillaries is challenging. Modern 3D printing may become a viable option in the future; however, this technique is just now approaching a resolution of $0.01\,\mathrm{mm}$ (vendor specification, N2 Plus FFF 3D, Raise3D, Irvine, CA), which can still be considered too coarse to adequately recreate a capillary bed with smooth surfaces. In this work a more unconventional yet approachable method was chosen using sacrificial sugar structures as initially proposed by Bellan et al[65]. The constructed phantom allowed for the controlled application of fluid flow at adjustable rates and optical microscopy revealed a capillary structure with comparable dimensions to in vivo capillary beds. It was therefore possible to generate true incoherent capillary flow within a single imaging voxel enabling the detailed assessment of the phase-distribution model. However, there are previously published studies based on IVIM measurements in various otherwise constructed phantoms using the straight-flow (sinc) or the pseudo-diffusion (biexponential) model.

Early experiments performed in 1987 by Ahn et al.[44] investigated the effects of water flow in a "*ball made by winding a long (33 m) flexible tube with a small diameter (1 mm) in a random fashion*", using gravity to generate flow. The authors found a good agreement between the measured signal decay and their signal model, which corresponds to the straight flow limit while considering a laminar flow profile within the tube. The authors justify their methodology by concluding from previously published data[107,108] that in vivo blood flow in capillaries is *"almost linear with constant velocities"* within their experiment duration of $100\,\mathrm{ms}$. However, the assumed capillary length of $0.75\,\mathrm{mm}$ and flow velocity of 0.3 to $0.5\,\mathrm{mm/s}$ are not in good agreement with more recently reported values, as detailed above.

Within one of their initial studies on IVIM MRI, Le Bihan et al.[42] constructed a phantom consisting of a column packed with porous microspheres. Flow through the phantom was maintained by gravity. They assumed that the water inside the microspheres was diffusing only, while the water in the interstitial volume was flowing in random orientations. On this basis, a theoretical perfusion fraction of $f = 0.32$ was expected, however, the analysis of the measured data using the biexponential IVIM model yielded a significantly lower perfusion fraction of only $f = 0.09$. The authors attribute this discrepancy to *"a too-low water flow"*. This is very much in line with the

results in the presented work, as it was shown by simulation and experiment that the signal fraction f estimated using the biexponential model can suffer from a significant negative bias and is dependent on the flow velocity. Furthermore, it is plausible that the implicit model assumption in the study of Le Bihan et al. of delta-distributed particle speeds did not reflect the actual particle speed distribution inside the constructed phantom.

In 2012 Cho et al.[61] presented IVIM measurements in a very sophisticated phantom using encapsulated sponges allowing them to apply varying degrees of pressure. They analyzed the data using the biexponential model and, in accordance with the presented work, the authors found that aligning the gradient direction with the direction of the macroscopic flow results in a greatly accelerated signal decay and results in higher estimates for the pseudo-diffusion coefficient D^* compared to the transverse directions. The estimates for D^* displayed a positive correlation to the applied pressure; however, the authors also state that the signal decay using flow-compensated diffusion gradients remains largely unaffected by the applied pressure. This suggests that the flowing particles were performing a largely linear motion (straight-flow limit) within the duration of the diffusion experiment. The applicability of the biexponential IVIM model is therefore questionable, which might explain why the estimated signal fraction f was increasing with the applied pressure in some of their measurements.

In a recently published study, Lee et al.[64] performed IVIM measurements in columns filled with sephadex gel beads of different sizes at varying rates of flow. Following Le Bihan et al., water inside the beads was considered stagnant, while water in the interstitial volume was considered to be flowing. With this in mind, a flowing water content fraction FWC was estimated for each bead size by analyzing micro-CT images of the respective column. The comparison between the estimated signal fraction f, using the biexponential model, and the FWC followed a familiar pattern: The signal fraction f mostly underestimated FWC, especially at low flow rates and f displayed a strong positive correlation to the applied flow rate. Furthermore, the estimated D^* displayed a counterintuitive behavior by initially decreasing as the applied rate flow was increased. In light of the presented work, these occurrences can be explained a) by too-slow flow and therefore not reaching the pseudo-diffusion limit, b) by causing little flow-induced signal decay and c) by ignoring that the particle flow speeds might follow a complex distribution. The authors also analyzed the measured data using a segmented fitting approach[15], designed to allow for a more robust estimation of the model parameters at the expense of a possible bias[109]. This helped to alleviate the counterintuitive behavior of D^*, however, resulting in even smaller estimates for f.

Limitations

The performed simulation study demonstrated that inappropriate model assumptions can lead to a significant bias in the estimated parameters. Notably, the particle speed distribution was found to have a significant impact on the resulting signal decay and, vice versa, properly accounting for the particle speed distribution when analyzing IVIM MRI data was proven to be pivotal to generate meaningful parameter estimates. For example considering a wide speed distribution with a non-negligible fraction of slowly flowing particles, many more (average) directional changes are necessary to result in an approximately exponential signal decay compared to delta-distributed particle speed distributions (with only a single speed). In the presented work, the speed distribution for the constructed capillary network was approximated by adapting previously published results on the related topic of fluid flow in fracture networks. Having further established that the flow can be

expected to be laminar within a given capillary, the resulting speed distribution $\rho_{\mathrm{CN}}(v)$ was found to be highly asymmetric and L-shaped. A comparison of the signal model fits of the experimental data indicated that the determined particle speed distribution in the capillary network $\rho_{\mathrm{CN}}(v)$ is indeed a reasonable approximation of the true speed distribution. Compared to a uniform distribution and to a delta distribution, the signal model using $\rho_{\mathrm{CN}}(v)$ resulted in greatly reduced RSS values, especially at higher flow rates. Obvious patterns in the residuals are a sign of applying an inappropriate speed distribution. The speed distribution $\rho_{\mathrm{CN}}(v)$ improves upon this; however, upon close examination the residuals still show a visible pattern indicating that the true underlying particle speed distribution may follow a more complex and irregular shape. Considering possible in vivo measurements, such subtle systematic deviations between measured data and model fits are likely to be obscured by image noise making it challenging to assess the correct speed distribution based on the model fits. To approximate the speed distribution for in vivo microperfusion, further considerations will be necessary. While the assumption of laminar flow is reasonable under the experimental conditions in the constructed capillary phantom, blood flow in very small capillaries is unlikely to be strictly laminar. The diameters of smaller capillaries can easily be surpassed by the size of human red blood cells (6.2 – 8.2 µm[110]), which are then "squeezed" through the capillaries separated by segments of plasma, creating a plug-flow effect[111,112]. Naturally, the heterogeneous composition of blood also influences the flow in larger capillaries and microvessels[113]. Flowing blood acts therefore as a non-Newtonian fluid and the velocity profile of laminar flow likely needs to be re-evaluated for in vivo experiments. Furthermore, the distribution of average flow speeds across differently sized capillaries must be considered.

Unfortunately, there is no ground truth for the average particle speed inside the capillary network and the estimates had to be validated indirectly by performing a regression analysis. As mentioned above, the highly significant linear correlation with the applied flow rate indicates that practically all variation in v is predictable from the applied flow rate and the small y-axis intercept shows that there negligible constant bias. This does leave the estimated average particle speed open to a proportional bias, meaning that the true value could be over- or underestimated by a certain fixed percentage. While this is certainly not ideal, it can be argued that a proportional bias is less critical in a clinical question once reference values for healthy tissue or baseline values for progress monitoring of a disease have been established.

A Monte Carlo simulation study revealed that the duration of the diffusion-sensitizing period of the employed gradient schemes has a significant impact on the accuracy of the estimated parameters. Regarding the flow-compensated gradient scheme, the accuracy generally benefits from a very short diffusion-sensitizing duration. However, at the same time the maximum b-value needs to be large enough to facilitate a proper separation of the flowing and solely diffusing signal fractions. Since the diffusion-sensitizing duration and the maximum obtainable b-value are closely related, this poses a significant challenge to the MRI systems hardware. Within this work, this issue was addressed by employing multiple flow-compensated gradient schemes, one of which used a reduced b-value set to achieve a shorter gradient duration.

It should be noted that the construction process of the capillary phantom creates a random network of channels, which precludes the manufacturing of identical standardized phantoms. By keeping variables such as the humidity and the pressure that is applied to compress the sugar fibers con-

stant, it is possible to construct phantoms with similar properties, however, the exact structure of the capillary network will ultimately be unique. Accordingly, each constructed phantom will have to be characterized individually. While the formed capillary network closely resembles in vivo capillary beds, the curved nature of blood vessels could only be emulated to a certain degree and the rigid matrix material does not allow for expansion or contraction of the microchannels.

Conclusion & Outlook

The constructed phantom facilitated the detailed investigation of incoherent-flow-induced spin dephasing in DW-MRI in a controllable fashion. To our knowledge, it is the first phantom to mimic the key feature of fluid flow inside a highly interconnected network of randomly oriented channels at the scale of in vivo capillary beds serving as a basis for the applicability of IVIM MRI methods. The systematic analysis of the acquired data has greatly improved the understanding of the interplay of capillary flow characteristics and the resulting signal decay measured using DW-MRI. The results showed that advanced methods are capable of accurately characterizing fluid flow inside a capillary network in a reproducible manner, yielding meaningful and intuitive parameter estimates. At the same time, the phantom experiments confirmed the results from the initial simulation study, where the importance of appropriate model assumptions emerged. Specifically, the particle speed distribution was shown to have a significant impact on the resulting signal decay and, if not properly accounted for, can lead to significant systematic errors in parameter estimates.

The findings of this study indicate that the use of the biexponential IVIM model should be treated with caution since the estimated parameters are at risk to be subject to a significant bias. Future studies examining perfusory effects using DW-MRI should be aware of this potential issue and are advised to verify that the model assumptions reflect the nature of the blood flow in the investigated tissue. Compared to the commonly used biexponential model, the more advanced phase-distribution model features the consideration of arbitrary particle speed distributions while having the additional benefit of obtaining information about the capillary morphology, which may be of diagnostic value in cancerous diseases [114–118] for example.

However, the current methodology of this advanced technique limits its applicability. Generating the phase distributions needed for the data analysis requires significant computing power as well as the a priori knowledge about the employed gradient profiles and the particle speed distribution (if accounted for). Moreover, the long measurement procedure involving multiple DW-MRI sequences with varying gradient profiles is likely to prove prohibitive in a clinical setting. With this regard, in this work a first step was taken by relating the parameter estimation accuracy to the duration of the employed diffusion gradients with the goal of devising optimized measurement settings. Future endeavors should place a focus on making this technique more approachable and time efficient, for example by incorporating compressed sensing techniques[119], to allow for applications in clinical studies and to unveil its diagnostic potential.

The usage of the constructed phantom is not limited to DW-MRI. In a previous publication[120] the capillary network was demonstrated to facilitate the assessment of dynamic contrast-enhanced[121] MRI yielding highly reproducible results. As a possible next step, further imaging techniques aiming to provide information about tissue perfusion, such arterial spin labeling[122] may be investigat-

ed. Additionally, the phantom design may be further improved, for example by experimenting with flexible matrix materials to reflect the elastic nature of in vivo capillaries more accurately.

9 Summary/Zusammenfassung

Diffusion-weighted magnetic resonance imaging (DW-MRI)[7,41] offers the unique possibility to assess non-invasively the microscopic displacement of water molecules inside biological tissue. For free thermal molecular diffusion, the measured DW-MRI signal intensity as a function of the applied diffusion weighting follows an exponential decay. However, DW-MRI is not only sensitive to thermal molecular diffusion, but also to incoherent motion of water molecules in general, coining the term *intravoxel incoherent motion* (IVIM) MRI[42]. A primary source of such motion in vivo (in addition to thermal molecular diffusion) is capillary blood flow, leading to an additional superimposed decay attributed to the signal of blood in perfused capillaries. This effect can be utilized to assess tissue hemodynamics non-invasively, which is a highly desirable prospect for the diagnosis of many diseases making IVIM MRI a topic of current research. However, the exact shape of the signal decay in IVIM MRI depends not only on the speed of blood flow, but also on the time until a flowing particle changes its movement direction (due to capillary curvature or branching). Two limiting cases lead to analytical solutions: Straight particle movement, i.e. no changes of movement direction during the diffusion-sensitizing period, results in a sinc-like signal decay. In contrast, the signal decay of many directional changes during the diffusion experiment, called pseudo-diffusion limit, can be approximated by an exponential function, which results (after including thermal diffusion) in a biexponential signal decay.

This biexponential pseudo-diffusion model enjoys great popularity since it is elegant and seemingly fits measured data from a great variety of organs very well. However, it is often unclear or ignored if the preconditions for the pseudo-diffusion model are met. This issue was recently addressed by Wetscherek et al.[26,27] by introducing a method that does not assume a limiting case but is based on phase distributions of the NMR spin ensemble generated by the simulation of particle pathways. With this approach, it was not only shown that the pseudo-diffusion limit was not reached in common DW-MRI experiments in the liver and pancreas, but the new method also allowed to estimate the average speed $\langle v \rangle$ of the blood flow as well as the characteristic duration τ until a particle changes its movement direction. In contrast, the conventional pseudo-diffusion model combines these measures into the pseudo-diffusion coefficient $D^* = \langle v \rangle^2 \tau / 6$. Furthermore, picturing the microvasculature as a successive network of straight segments, the average length of a single segment can be calculated via $l = \langle v \rangle \cdot \tau$. Unlike the pseudo-diffusion model, the phase-distribution method also allows for the explicit consideration of a particle speed distribution. However, the validation of IVIM MRI methods in vivo is inherently difficult. Quantities such as the blood flow velocity and the capillary length are extremely challenging, if not impossible, to determine in vivo without the use of highly invasive methods and can hardly be regulated.

The purpose of this thesis was to approach this problem by assessing and comparing conventional pseudo-diffusion IVIM MRI and phase-distribution IVIM MRI experimentally using a perfusable capillary phantom. As a secondary goal, detailed numerical simulations aimed to consolidate the experimental findings and to advance the understanding of the effects of flow characteristics on data measured using DW-MRI.

A capillary phantom was constructed to assess fluid flow at systematically variable rates inside a highly interconnected network of randomly oriented channels at the scale of in vivo capillary beds. Adapting a method proposed by Bellan et al.[65] the capillary network was formed using sacrificial sugar fibers embedded into synthetic resin. The phantom was customized to allow for the controlled application of fluid flow at variable rates while performing DW-MRI. Optical microscopy revealed a dense and highly interconnected network of randomly oriented capillaries strewn with spherical dilations. The measured average capillary length of $162 + 78$ µm and the average capillary diameter of 11.4 ± 4.4 µm are within the range of in vivo capillary dimensions, enabling incoherent particle motion within the scale of a single imaging voxel.

As was demonstrated by an initial simulation study, accounting for the particle speed distribution inside the constructed phantom is critical to facilitate accurate assessment of the capillary flow characteristics using IVIM MRI. Based on previously published results[50,51] on the related topic of fluid flow in fracture networks, the speed distribution inside the constructed capillary network was approximated by a highly asymmetric and L-shaped speed distribution $\rho_{\mathrm{CN}}(v) \propto \sqrt{6\langle v\rangle}/\sqrt{v} - 1$ with average flow speed $\langle v\rangle$.

Flow-dependent IVIM MRI experiments were carried out by connecting the capillary phantom to a syringe pump and increasing the applied flow rate from $0.2\ \mathrm{ml/min}$ to $2.4\ \mathrm{ml/min}$ in increments of $0.2\ \mathrm{ml/min}$. For each flow rate, data was acquired using four different DW-MRI sequences, two with monopolar diffusion gradient schemes and two with flow-compensated schemes. The respective duration of the diffusion preparation was optimized with the aim of improving the parameter estimation accuracy based on the results of a Monte Carlo simulation.

Utilizing the Akaike information criterion (AIC), the acquired data was shown to be best described by a two-compartment model consisting of a static and a flowing compartment, where the static compartment is hypothesized to be ascribed to liquid inside the spherical dilations. The phase-distribution model allowed for an excellent fit to the acquired data with a small residual sum of squares (RSS) independent of the applied flow rate. A comparison of the respective model fits demonstrated greatly reduced RSS values using $\rho_{\mathrm{CN}}(v)$ compared to uniformly or delta-distributed particle speeds, highlighting the importance of considering an appropriate underlying particle speed distribution.

Using the phase-distribution model, the estimated signal fraction f of the flowing compartment stayed approximately constant over the applied flow rates. The average of $f = 0.451 \pm 0.023$ agrees very well with the ratio of the volume inside the capillaries to the total (capillaries plus dilations) network volume, estimated at 0.454 ± 0.002 using the data from optical microscopy.

The estimated average particle flow speeds, ranging from $v = 0.25\ \mathrm{mm/s}$ up to $2.7\ \mathrm{mm/s}$, cover various reported in vivo flow speed values of red blood cells[71,105,106]. A regression analysis revealed a highly significant linear proportionality to the applied flow rate with a coefficient of determination of $R^2 = 0.99$, indicating that practically all variation in v is predictable from the applied flow rate. Furthermore, there seems to be negligible constant bias as the estimated y-axis intercept of $0.034\ \mathrm{mm/s}$ was close to zero.

At very small flow rates, the characteristic duration τ until a directional change occurs could not be determined with satisfactory accuracy resulting in large standard errors. At flow rates greater than $0.8\ \mathrm{ml/min}$, τ showed an inverse proportionality to the applied flow rate. Consequently,

the estimated capillary segment length stayed approximately constant in this domain with an average of 195 ± 13 µm close to the average length determined using optical microscopy of $162 + 78$ µm.

Analyzing the measured data using the biexponential pseudo-diffusion IVIM model resulted in substantially increased RSS values compared to the phase-distribution model at flow rates greater than $0.8\ \mathrm{ml/min}$. This indicates that even at the highest flow rate, the pseudo-diffusion limit was not reached and the signal decay was not properly fit by the biexponential model. In line with the simulation study, the discrepancy between data and model resulted in a significant bias of the estimated parameters. Most notably, the signal fraction f was heavily underestimated (with values between 0.12 and 0.24) and displayed a clear dependence on the applied flow rate. Yet, the estimated particle speed $v_{\mathrm{biexp}} = 6D^*/l$ closely followed the particle speed determined using the phase-distribution model. These findings highlight the intricate interplay of the model parameters and show that the accuracy and validity of the estimates are highly susceptible to the chosen model assumptions.

In conclusion, the constructed phantom enabled the detailed investigation of incoherent-flow-induced spin dephasing in DW-MRI in a controllable fashion. To our knowledge, it is the first phantom to mimic the key feature of fluid flow inside a highly interconnected network of randomly oriented channels at the scale of in vivo capillary beds serving as a basis for the applicability of IVIM MRI methods. The systematic analysis of the acquired data has substantially improved the understanding of the interplay of capillary flow characteristics and the resulting signal decay measured using DW-MRI. The results showed that advanced methods are capable of accurately characterizing fluid flow inside a capillary network. At the same time, the phantom experiments confirmed the results from the initial simulation study, where the importance of appropriate model assumptions emerged. Specifically, the statistical distribution of particle speeds was shown to have significant impact on the resulting signal decay and, if not properly accounted for, can lead to significant systematic errors in parameter estimates such as the perfusion fraction.

Die diffusionsgewichtete Magnetresonanztomographie (DW-MRT)[7,41] bietet die einzigartige Möglichkeit, die mikroskopische Bewegung von Wassermolekülen innerhalb von biologischem Gewebe nicht-invasiv zu untersuchen. Für freie thermische Diffusion folgt der gemessene Signalverlauf als Funktion der angewandten Diffusionsgewichtung einem exponentiellen Zerfall. Die DW-MRT ist jedoch nicht nur sensitiv gegenüber der thermischen Diffusion, sondern grundsätzlich gegenüber jeglicher inkohärenten Bewegung der Wassermoleküle. Diese Tatsache prägte den Begriff der „*intravoxel incoherent motion*"-(IVIM-)MRT[42]. Eine Hauptquelle solch inkohärenter Bewegung im Gewebe (zusätzlich zur thermischen Diffusion) stellt der Blutfluss in Mikrokapillaren dar. Bei einer Untersuchung mittels DW-MRT führt dies zu einem überlagerten Zerfall des Signalanteils der Wassermoleküle im Blut, dem Perfusionsanteil. Dieser Effekt kann für die nicht-invasive Evaluierung der Hämodynamik im Gewebe genutzt werden, die für die Diagnose vieler Krankheitsbilder sehr hilfreich ist; die IVIM-MRT ist daher ein Gebiet aktueller Forschung. Die genaue Form des mittels IVIM-MRT gemessenen Signalverlaufs hängt allerdings nicht nur von der Fließgeschwindigkeit des Blutes ab, sondern insbesondere auch von der Dauer, bis ein fließendes Molekül seine Bewegungsrichtung ändert (aufgrund von gekrümmten oder verzweigenden Kapillaren). Zwei Grenzfälle führen dabei zu analytischen Lösungen: Geradlinige (jedoch zufällig gerichtete) Bewegung der Moleküle, also keine Änderung der Bewegungsrichtung während der Diffusionspräparation, führt zu einem sinc-förmigen Signalzerfall. Im Gegensatz dazu lässt sich der Signalzerfall bei sehr vielen Richtungsänderungen während der Diffusionspräparation, als Pseudo-Diffusions-Grenzfall bezeichnet, durch eine exponentielle Funktion annähern. Zusammen mit den Auswirkungen der thermischen Diffusion ergibt sich so ein biexponentieller Signalverlauf.

Dieses biexponentielle Pseudo-Diffusionsmodell erfreut sich großer Beliebtheit, da es elegant ist und sehr gut die Messdaten aus einer Vielzahl von Organen beschreibt. Es ist jedoch oft unklar oder wird vernachlässigt, ob die Voraussetzungen für die Anwendbarkeit des Pseudo-Diffusionsmodells erfüllt sind. Diese Problematik wurde kürzlich von Wetscherek et al.[26,27] durch die Einführung einer Methode, die keinen Grenzfall voraussetzt, adressiert. Die vorgestellte Methode basiert auf Phasenverteilungen des NMR-Spinensembles, welche durch die Simulation von Teilchenpfaden erzeugt werden. Mit diesem Ansatz ließ sich nicht nur nachweisen, dass das Pseudo-Diffusionslimit bei gängigen DW-MRT Experimenten in Leber und Pankreas nicht erreicht wurde, sondern er ermöglichte es auch, die Durchschnittsgeschwindigkeit $\langle v \rangle$ des Blutflusses sowie die Dauer τ, bis ein fließendes Teilchen seine Bewegungsrichtung ändert, zu bestimmen. Im Gegensatz dazu kombiniert das herkömmliche Pseudo-Diffusionsmodell diese Messgrößen zu dem Pseudo-Diffusionskoeffizienten $D^* = \langle v \rangle^2 \tau / 6$. Betrachtet man die Mikrovaskulatur als ein aufeinanderfolgendes Netzwerk von geraden Segmenten, kann zudem die durchschnittliche Länge eines einzelnen Segments über $l = \langle v \rangle \cdot \tau$ berechnet werden. Anders als das Pseudo-Diffusionsmodell, erlaubt das Phasenverteilungsmodell auch die explizite Berücksichtigung von Geschwindigkeitsverteilungen der fließenden Teilchen. Die Validierung von IVIM-MRT-Verfahren in vivo gestaltet sich jedoch inhärent problematisch. Größen wie die Fließgeschwindigkeit des Blutes und die Kapillarlänge sind extrem schwierig, wenn nicht sogar unmöglich, in vivo ohne den Einsatz von hochinvasiven Methoden zu bestimmen und können kaum reguliert werden.

Das Hauptziel dieser Arbeit war es deshalb, konventionelle Pseudo-Diffusions-IVIM-MRT und Phasenverteilungs-IVIM-MRT experimentell unter Verwendung eines perfundierbaren Kapillarphantoms zu überprüfen und zu vergleichen. Als sekundäres Ziel sollten mithilfe von detaillierten

numerischen Simulationen die experimentellen Ergebnisse konsolidiert und das Verständnis des Zusammenhangs zwischen Flusseigenschaften und DW-MRT-Daten verbessert werden.

Um Fluss mit systematisch variierbaren Geschwindigkeiten innerhalb eines Kapillarnetzwerks in der Größenordnung von In-vivo-Kapillarbetten zu analysieren, wurde ein entsprechendes Messphantom hergestellt. Nach einem von Bellan et al.[65] vorgeschlagenen Verfahren wurde das Kapillarnetzwerk unter Verwendung von in Kunstharz eingebetteten und anschließend herausgelösten Zuckerfasern gebildet. Das Messphantom wurde mit einem Zu- und Ablauf versehen, um während der DW-MRT-Untersuchung einen kontrollierbaren Fluss mit variablen Geschwindigkeiten zu ermöglichen. Die optische Mikroskopie zeigte ein dichtes und stark verzweigtes Netzwerk aus zufällig orientierten Kapillaren, durchsetzt mit kugelförmigen Dilatationen. Die gemessene durchschnittliche Kapillarlänge von $162 + 78\ \mu\text{m}$ und der durchschnittliche Kapillardurchmesser von $11{,}4 \pm 4{,}4\ \mu\text{m}$ liegen im Bereich der In-vivo-Kapillardimensionen und ermöglichen damit die inkohärente Teilchenbewegung innerhalb eines einzelnen Bildgebungsvoxels.

Wie eine initiale Simulationsstudie gezeigt hat, ist die Berücksichtigung der Geschwindigkeitsverteilung der Teilchen innerhalb des konstruierten Messphantoms von entscheidender Bedeutung, um eine akkurate Quantifizierung des Kapillarflusses mittels IVIM-MRT zu ermöglichen. Basierend auf bereits veröffentlichten Ergebnissen[50,51] zum verwandten Thema der Flüssigkeitsströme in Kluftnetzwerken, wurde die Fließgeschwindigkeitsverteilung innerhalb des hergestellten Kapillarnetzwerks durch eine stark asymmetrische und L-förmige Geschwindigkeitsverteilung $\rho_{\mathrm{CN}}(v) \propto \sqrt{6\langle v\rangle}/\sqrt{v} - 1$, mit der durchschnittlichen Fließgeschwindigkeit $\langle v\rangle$, approximiert.

Flussabhängige IVIM-MRT-Experimente wurden durchgeführt, indem das Kapillarphantom an eine Injektionspumpe angeschlossen und der eingestellte Volumenstrom von $0{,}2\ \mathrm{ml/min}$ auf $2{,}4\ \mathrm{ml/min}$ in Schritten von $0{,}2\ \mathrm{ml/min}$ erhöht wurde. Bei jedem Volumenstrom wurden Daten mit vier verschiedenen DW-MRT-Sequenzen aufgenommen, zwei mit monopolaren Diffusionsgradientenschemata und zwei mit flusskompensierten Schemata. Basierend auf den Ergebnissen einer Monte-Carlo-Simulation, wurde die jeweilige Dauer der Diffusionspräparation hinsichtlich der Genauigkeit der zu bestimmenden Parameter optimiert.

Die Berechnung des Akaike-Informationskriteriums (AIC) hat gezeigt, dass die erfassten Daten am besten durch ein Zwei-Kompartiment-Modell beschrieben werden, welches aus einem statischen und einem fließenden Kompartiment besteht. Es ist davon auszugehen, dass das statische Kompartiment der Flüssigkeit innerhalb der kugelförmigen Dilatationen zuzuschreiben ist. Das Phasenverteilungsmodell ermöglichte einen hervorragenden Modellfit an die Messdaten mit einer niedrigen Residuenquadratsumme (RSS) unabhängig vom angelegten Volumenstrom. Die RSS-Werte zeigten sich deutlich reduziert unter Verwendung der Geschwindigkeitsverteilung $\rho_{\mathrm{CN}}(v)$ im Vergleich zu gleichverteilten oder Dirac-verteilten Geschwindigkeiten. Diese Ergebnisse unterstreichen, dass die Berücksichtigung der zugrundeliegenden Teilchengeschwindigkeitsverteilung maßgeblich die Flusscharakterisierung mittels IVIM-MRT beeinflusst.

Unter Verwendung des Phasenverteilungsmodells blieb der bestimmte Signalanteil f des fließenden Kompartiments über die angelegten Volumenströme näherungsweise konstant. Der Durchschnittswert von $f = 0{,}451 \pm 0{,}023$ liegt nahe bei dem Verhältnis des Volumens innerhalb der Kapillaren zum Gesamtvolumen (Kapillaren plus Dilatationen), welches anhand der optischen Mikroskopie auf $0{,}454 \pm 0{,}002$ geschätzt wurde.

Die ermittelten durchschnittlichen Teilchengeschwindigkeiten reichen von $v = 0{,}25$ bis $2{,}7\ \mathrm{mm/s}$ und umfassen damit diverse in der Literatur berichtete In-vivo-Fließgeschwindigkeiten von roten Blutkörperchen[71,105,106]. Eine Regressionsanalyse ergab eine hoch signifikante lineare Proportionalität von v zu dem angelegten Volumenstrom mit einem Bestimmtheitsmaß von $R^2 = 0{,}99$, was darauf hinweist, dass praktisch alle Variationen in v aus dem angelegten Volumenstrom vorhersagbar sind. Darüber hinaus scheint eine etwaige systematische Abweichung vernachlässigbar zu sein, da der bestimmte y-Achsenabschnitt von $0{,}034\ \mathrm{mm/s}$ nahe bei Null lag.

Bei sehr niedrigen Volumenströmen konnte die Dauer τ, bis ein fließendes Teilchen seine Bewegungsrichtung ändert, nicht mit zufriedenstellender Genauigkeit bestimmt werden. Bei Volumenströmen über $0{,}8\ \mathrm{ml/min}$ verhielt sich das ermittelte τ reziprok proportional zum angelegten Volumenstrom. Dementsprechend blieb die berechnete Kapillarsegmentlänge in dieser Domäne annähernd konstant mit einem Durchschnittswert von $195 \pm 13\ \mu\mathrm{m}$, welcher nahe dem mittels optischer Mikroskopie ermittelten Wert von $162 + 78\ \mu\mathrm{m}$ liegt.

Die Analyse der gemessenen Daten mit dem biexponentiellen Pseudo-Diffusions-IVIM-Modell zeigte deutlich erhöhte RSS-Werten im Vergleich zum Phasenverteilungsmodell bei Volumenströmen über $0{,}8\ \mathrm{ml/min}$. Das bedeutet, dass selbst beim höchsten Volumenstrom der Pseudo-Diffusion-Grenzfall nicht erreicht wurde und der Signalzerfall nicht adäquat durch das biexponentielle Modell beschrieben werden konnte. In Übereinstimmung mit der Simulationsstudie führte die Diskrepanz zwischen Daten und Modell zu einer erheblichen Abweichung der ermittelten Parameter. Vor allem der Signalanteil f wurde (mit Werten zwischen $0{,}12$ und $0{,}24$) stark unterschätzt und zeigte zudem eine deutliche Abhängigkeit vom angelegten Volumenstrom. Die ermittelte Teilchengeschwindigkeit $v_{\mathrm{biexp}} = 6D^*/l$ stimmte jedoch gut mit der Teilchengeschwindigkeit, welche unter Verwendung des Phasenverteilungsmodells bestimmt wurde, überein. Diese Ergebnisse unterstreichen das komplizierte Zusammenspiel der Modellparameter und zeigen, dass die Genauigkeit und Aussagekraft der ermittelten Parameter sehr anfällig gegenüber den gewählten Modellannahmen sind.

Zusammenfassend ermöglichte das hergestellte Messphantom, Effekte von inkohärentem Fluss in der DW-MRT auf kontrollierbare und systematische Art und Weise detailliert zu analysieren. Unseres Wissens handelt es sich dabei um das erste Phantom, welches die wesentlichen Schlüsselmerkmale für die Anwendbarkeit von IVIM-MRT-Verfahren aufweist, nämlich Fluidströmung in einem stark miteinander verbundenen Netzwerk von zufällig orientierten Kanälen in der Größenordnung von In-vivo-Kapillarbetten. Die systematische Analyse der erfassten Daten hat das Verständnis des Zusammenspiels von Strömungseigenschaften und dem daraus resultierenden DW-MRT-Signalabfall wesentlich verbessert. Die Ergebnisse zeigen, dass der Flüssigkeitsstrom in einem Kapillarnetzwerk mit den verwendeten komplexen Methoden akkurat charakterisiert werden kann. Gleichzeitig bestätigten die Phantomexperimente die Ergebnisse der Simulationsstudie, in der sich die Signifikanz adäquater Modellannahmen herauskristallisierte. Insbesondere zeigte sich, dass die statistische Verteilung der Fließgeschwindigkeiten einen wesentlichen Einfluss auf den resultierenden Signalzerfall hat und bei nicht ordnungsgemäßer Berücksichtigung zu erheblichen systematischen Fehlern bei der Parameterbestimmung (insbesondere beim Perfusionsanteil) führen kann.

Bibliography

1. Reiser MF, Semmler W, Hricak H. *Magnetic Resonance Tomography*. Berlin Heidelberg: Springer-Verlag; 2008. //www.springer.com/de/book/9783540293545. Accessed September 26, 2018.

2. van Zijl PCM, Yadav NN. Chemical Exchange Saturation Transfer (CEST): what is in a name and what isn't? *Magn Reson Med Off J Soc Magn Reson Med Soc Magn Reson Med*. 2011;65(4):927-948. doi:10.1002/mrm.22761

3. Rosen BR, Belliveau JW, Vevea JM, Brady TJ. Perfusion imaging with NMR contrast agents. *Magn Reson Med*. 1990;14(2):249-265.

4. Powers WJ. Cerebral hemodynamics in ischemic cerebrovascular disease. *Ann Neurol*. 1991;29(3):231-240. doi:10.1002/ana.410290302

5. Hamm B, Laniado M, Saini S. Contrast-enhanced magnetic resonance imaging of the abdomen and pelvis. *Magn Reson Q*. 1990;6(2):108-135.

6. Choyke PL, Dwyer AJ, Knopp MV. Functional tumor imaging with dynamic contrast-enhanced magnetic resonance imaging. *J Magn Reson Imaging JMRI*. 2003;17(5):509-520. doi:10.1002/jmri.10304

7. Torrey HC. Bloch Equations with Diffusion Terms. *Phys Rev*. 1956;104(3):563-565. doi:10.1103/PhysRev.104.563

8. Brown R. A brief account of microscopical observations made in the months of June, July and August 1827, on the particles contained in the pollen of plants; and on the general existence of active molecules in organic and inorganic bodies. *Philos Mag*. 1828;4(21):161-173. doi:10.1080/14786442808674769

9. Moseley ME, Cohen Y, Mintorovitch J, et al. Early detection of regional cerebral ischemia in cats: comparison of diffusion- and T2-weighted MRI and spectroscopy. *Magn Reson Med*. 1990;14(2):330-346.

10. Chenevert TL, Brunberg JA, Pipe JG. Anisotropic diffusion in human white matter: demonstration with MR techniques in vivo. *Radiology*. 1990;177(2):401-405. doi:10.1148/radiology.177.2.2217776

11. Christidi F, Karavasilis E, Samiotis K, Bisdas S, Papanikolaou N. Fiber tracking: A qualitative and quantitative comparison between four different software tools on the reconstruction of major white matter tracts. *Eur J Radiol Open*. 2016;3:153-161. doi:10.1016/j.ejro.2016.06.002

12. Koh D-M, Collins DJ. Diffusion-weighted MRI in the body: applications and challenges in oncology. *AJR Am J Roentgenol*. 2007;188(6):1622-1635. doi:10.2214/AJR.06.1403

13. Le Bihan D, Breton E, Lallemand D, Grenier P, Cabanis E, Laval-Jeantet M. MR imaging of intravoxel incoherent motions: application to diffusion and perfusion in neurologic disorders. *Radiology*. 1986;161(2):401-407. doi:10.1148/radiology.161.2.3763909

14. Le Bihan D, Lima M, Federau C, Sigmund E. *Intravoxel Incoherent Motion (IVIM) MRI - Principles and Applications*. First Edition. Pan Stanford Publishing Pte Ltd.; 2018. http://www.panstanford.com/books/9789814800198.html. Accessed November 20, 2018.

15. Schneider MJ, Dietrich O, Ingrisch M, et al. Intravoxel Incoherent Motion Magnetic Resonance Imaging in Partially Nephrectomized Kidneys. *Invest Radiol*. 2016;51(5):323-330. doi:10.1097/RLI.0000000000000244

16. Caroli A, Schneider M, Friedli I, et al. Diffusion-weighted magnetic resonance imaging to assess diffuse renal pathology: a systematic review and statement paper. *Nephrol Dial Transplant*. 2018;33(suppl_2):ii29-ii40. doi:10.1093/ndt/gfy163

17. Luciani A, Vignaud A, Cavet M, et al. Liver cirrhosis: intravoxel incoherent motion MR imaging--pilot study. *Radiology*. 2008;249(3):891-899. doi:10.1148/radiol.2493080080

18. Kim B, Lee SS, Sung YS, et al. Intravoxel incoherent motion diffusion-weighted imaging of the pancreas: Characterization of benign and malignant pancreatic pathologies. *J Magn Reson Imaging JMRI*. 2017;45(1):260-269. doi:10.1002/jmri.25334

19. Le Bihan D. What can we see with IVIM MRI? *NeuroImage*. December 2017. doi:10.1016/j.neuroimage.2017.12.062

20. Noij DP, Martens RM, Marcus JT, et al. Intravoxel incoherent motion magnetic resonance imaging in head and neck cancer: A systematic review of the diagnostic and prognostic value. *Oral Oncol*. 2017;68:81-91. doi:10.1016/j.oraloncology.2017.03.016

21. Klauß M, Maier-Hein K, Tjaden C, Hackert T, Grenacher L, Stieltjes B. IVIM DW-MRI of autoimmune pancreatitis: therapy monitoring and differentiation from pancreatic cancer. *Eur Radiol*. October 2015. doi:10.1007/s00330-015-4041-4

22. Hauser T, Essig M, Jensen A, et al. Characterization and therapy monitoring of head and neck carcinomas using diffusion-imaging-based intravoxel incoherent motion parameters-preliminary results. *Neuroradiology*. 2013;55(5):527-536. doi:10.1007/s00234-013-1154-9

23. Reischauer C, Patzwahl R, Koh D-M, Froehlich JM, Gutzeit A. Non-Mono-Exponential Analysis of Diffusion-Weighted Imaging for Treatment Monitoring in Prostate Cancer Bone Metastases. *Sci Rep*. 2017;7(1):5809. doi:10.1038/s41598-017-06246-4

24. Shi C, Liu D, Xiao Z, et al. Monitoring Tumor Response to Antivascular Therapy Using Non-Contrast Intravoxel Incoherent Motion Diffusion-Weighted MRI. *Cancer Res*. 2017;77(13):3491-3501. doi:10.1158/0008-5472.CAN-16-2499

25. Ahlgren A, Knutsson L, Wirestam R, et al. Quantification of microcirculatory parameters by joint analysis of flow-compensated and non-flow-compensated intravoxel incoherent motion (IVIM) data. *NMR Biomed*. 2016;29(5):640-649. doi:10.1002/nbm.3505

26. Wetscherek A. Magnetic Resonance Diffusion Weighted Imaging: Flow Compensated Intravoxel Incoherent Motion Imaging as a Tool to Probe Microvasculature. 2013.

27. Wetscherek A, Stieltjes B, Laun FB. Flow-compensated intravoxel incoherent motion diffusion imaging. *Magn Reson Med*. 2015;74(2):410-419. doi:10.1002/mrm.25410

28. Abragam A. *The Principles of Nuclear Magnetism*. Clarendon Press; 1983.

29. Arnol'd VI. *Mathematical Methods of Classical Mechanics*. 2nd ed. New York: Springer-Verlag; 1989. //www.springer.com/de/book/9780387968902. Accessed August 7, 2018.

30. Bottomley PA, Foster TH, Argersinger RE, Pfeifer LM. A review of normal tissue hydrogen NMR relaxation times and relaxation mechanisms from 1-100 MHz: dependence on tissue type, NMR frequency, temperature, species, excision, and age. *Med Phys*. 1984;11(4):425-448. doi:10.1118/1.595535

31. Traficante DD. Relaxation. Can T2, be longer than T1? *Concepts Magn Reson*. 1991;3(3):171-177. doi:10.1002/cmr.1820030305

32. Balchandani P, Naidich TP. Ultra-High-Field MR Neuroimaging. *AJNR Am J Neuroradiol*. 2015;36(7):1204-1215. doi:10.3174/ajnr.A4180

33. Bloch F. Nuclear Induction. *Phys Rev*. 1946;70(7-8):460-474. doi:10.1103/PhysRev.70.460

34. Hahn EL. Spin Echoes. *Phys Rev*. 1950;80(4):580-594. doi:10.1103/PhysRev.80.580

35. Burstein D. Stimulated echoes: Description, applications, practical hints. *Concepts Magn Reson*. 1996;8(4):269-278. doi:10.1002/(SICI)1099-0534(1996)8:4<269::AID-CMR3>3.0.CO;2-X

36. Haase A, Frahm J, Matthaei D, et al. MR imaging using stimulated echoes (STEAM). *Radiology*. 1986;160(3):787-790. doi:10.1148/radiology.160.3.3737918

37. Bernstein MA, King KF, Zhou XJ. *Handbook of MRI Pulse Sequences*. Elsevier; 2004.

38. Fick A. Ueber Diffusion. *Ann Phys*. 1855;170(1):59-86. doi:10.1002/andp.18551700105

39. Basser PJ. Inferring microstructural features and the physiological state of tissues from diffusion-weighted images. *NMR Biomed*. 1995;8(7-8):333-344.

40. Mansfield P. Multi-planar image formation using NMR spin echoes. *J Phys C Solid State Phys*. 1977;10(3):L55. doi:10.1088/0022-3719/10/3/004

41. Stejskal EO, Tanner JE. Spin Diffusion Measurements: Spin Echoes in the Presence of a Time-Dependent Field Gradient. *J Chem Phys*. 1965;42(1):288-292. doi:10.1063/1.1695690

42. Le Bihan D, Breton E, Lallemand D, Aubin ML, Vignaud J, Laval-Jeantet M. Separation of diffusion and perfusion in intravoxel incoherent motion MR imaging. *Radiology*. 1988;168(2):497-505. doi:10.1148/radiology.168.2.3393671

43. Bihan DL, Turner R. The capillary network: a link between ivim and classical perfusion. *Magn Reson Med*. 1992;27(1):171-178. doi:10.1002/mrm.1910270116

44. Ahn CB, Lee SY, Nalcioglu O, Cho ZH. The effects of random directional distributed flow in nuclear magnetic resonance imaging. *Med Phys*. 1987;14(1):43-48.

45. Billingsley P. *Probability and Measure*. Wiley; 1995.

46. Munson B, Rothmayer A, Okiishi T, Huebsch W. *Fundamentals of Fluid Mechanics, 7th Edition*. Wiley http://www.wiley.com/WileyCDA/WileyTitle/productCd-EHEP002022.html. Accessed March 8, 2017.

47. Kestin J, Khalifa HE, Correia RJ. Tables of the dynamic and kinematic viscosity of aqueous NaCl solutions in the temperature range 20–150 °C and the pressure range 0.1–35 MPa. *J Phys Chem Ref Data*. 1981;10(1):71-88. doi:10.1063/1.555641

48. Painter S, Cvetkovic V, Selroos J-O. Power-law velocity distributions in fracture networks: Numerical evidence and implications for tracer transport. *Geophys Res Lett*. 2002;29(14):20-21. doi:10.1029/2002GL014960

49. Sir Horace L. *Hydrodynamics*. 6th ed.; 1994. http://www.cambridge.org/de/academic/subjects/mathematics/fluid-dynamics-and-solid-mechanics/hydrodynamics-6th-edition. Accessed July 15, 2018.

50. Frampton A, Cvetkovic V. Upscaling particle transport in discrete fracture networks: 1. Nonreactive tracers. *Water Resour Res*. 2007;43(10):W10428. doi:10.1029/2006WR005334

51. Frampton A, Cvetkovic V. Upscaling particle transport in discrete fracture networks: 2. Reactive tracers. *Water Resour Res*. 2007;43(10):W10429. doi:10.1029/2006WR005336

52. Arnold BC. Pareto and Generalized Pareto Distributions. In: *Modeling Income Distributions and Lorenz Curves*. Economic Studies in Equality, Social Exclusion and Well-Being. Springer, New York, NY; 2008:119-145. doi:10.1007/978-0-387-72796-7_7

53. Šimůnek J, Jarvis NJ, van Genuchten MT, Gärdenäs A. Review and comparison of models for describing non-equilibrium and preferential flow and transport in the vadose zone. *J Hydrol*. 2003;272(1):14-35. doi:10.1016/S0022-1694(02)00252-4

54. Shanno DF. Conditioning of Quasi-Newton Methods for Function Minimization. *Math Comput*. 1970;24(111):647-656. doi:10.2307/2004840

55. Gallant AR. *Nonlinear Statistical Models*. 1 edition. New York: Wiley; 1987.

56. Bates DM, Watts DG. *Nonlinear Regression Analysis and Its Applications*. 1 edition. New York: Wiley; 1988.

57. Rice SO. Mathematical analysis of random noise. *Bell Syst Tech J*. 1944;23(3):282-332. doi:10.1002/j.1538-7305.1944.tb00874.x

58. Gudbjartsson H, Patz S. The Rician Distribution of Noisy MRI Data. *Magn Reson Med*. 1995;34(6):910-914.

59. Bretthorst GL. How accurately can parameters from exponential models be estimated? A Bayesian view. *Concepts Magn Reson Part A*. 2005;27A(2):73-83. doi:10.1002/cmr.a.20044

60. Kiselev VG, Il'yasov KA. Is the "biexponential diffusion" biexponential? *Magn Reson Med*. 2007;57(3):464-469. doi:10.1002/mrm.21164

61. Cho GY, Kim S, Jensen JH, Storey P, Sodickson DK, Sigmund EE. A versatile flow phantom for intravoxel incoherent motion MRI. *Magn Reson Med*. 2012;67(6):1710-1720. doi:10.1002/mrm.23193

62. Gao J-H, Holland SK, Gore JC. Nuclear magnetic resonance signal from flowing nuclei in rapid imaging using gradient echoes. *Med Phys*. 1988;15(6):809-814. doi:10.1118/1.596197

63. Lorenz CH, Pickens DR, Puffer DB, Price RR. Magnetic resonance diffusion/perfusion phantom experiments. *Magn Reson Med*. 1991;19(2):254-260. doi:10.1002/mrm.1910190211

64. Lee JH, Cheong H, Lee SS, et al. Perfusion Assessment Using Intravoxel Incoherent Motion-Based Analysis of Diffusion-Weighted Magnetic Resonance Imaging: Validation Through Phantom Experiments. *Invest Radiol*. 2016;51(8):520-528. doi:10.1097/RLI.0000000000000262

65. Bellan LM, Singh SP, Henderson PW, Porri TJ, Craighead HG, Spector JA. Fabrication of an artificial 3-dimensional vascular network using sacrificial sugar structures. *Soft Matter*. 2009;5(7):1354. doi:10.1039/b819905a

66. Potter RF, Groom AC. Capillary diameter and geometry in cardiac and skeletal muscle studied by means of corrosion casts. *Microvasc Res*. 1983;25(1):68-84.

67. Rasband WS. *ImageJ*. Bethesda, Maryland, USA: U. S. National Institutes of Health; 1997. https://imagej.nih.gov/ij/. Accessed March 17, 2017.

68. R Development Core Team. *R: A Language and Environment for Statistical Computing*. R Foundation for Statistical Computing http://www.R-project.org.

69. Delignette-Muller M-L, Dutang C, Pouillot R, Denis J-B, Siberchicot A. *Fitdistrplus: An R Package for Fitting Distributions*.; 2017. https://cran.r-project.org/web/packages/fitdistrplus/index.html. Accessed October 25, 2017.

70. Cassot F, Lauwers F, Fouard C, Prohaska S, Lauwers-Cances V. A novel three-dimensional computer-assisted method for a quantitative study of microvascular networks of the human cerebral cortex. *Microcirc N Y N 1994*. 2006;13(1):1-18. doi:10.1080/10739680500383407

71. Pawlik G, Rackl A, Bing RJ. Quantitative capillary topography and blood flow in the cerebral cortex of cats: an in vivo microscopic study. *Brain Res*. 1981;208(1):35-58.

72. Schenck JF. The role of magnetic susceptibility in magnetic resonance imaging: MRI magnetic compatibility of the first and second kinds. *Med Phys*. 1996;23(6):815-850. doi:10.1118/1.597854

73. Stradiotti P, Curti A, Castellazzi G, Zerbi A. Metal-related artifacts in instrumented spine. Techniques for reducing artifacts in CT and MRI: state of the art. *Eur Spine J*. 2009;18(Suppl 1):102-108. doi:10.1007/s00586-009-0998-5

74. Laun FB, Huff S, Stieltjes B. On the effects of dephasing due to local gradients in diffusion tensor imaging experiments: relevance for diffusion tensor imaging fiber phantoms. *Magn Reson Imaging*. 2009;27(4):541-548. doi:10.1016/j.mri.2008.08.011

75. Arrighini GP, Maestro M, Moccia R. Magnetic Properties of Polyatomic Molecules. I. Magnetic Susceptibility of H2O, NH3, CH4, H2O2. *J Chem Phys*. 1968;49:882-889. doi:10.1063/1.1670155

76. Keyser PT, Jefferts S. Magnetic susceptibility of some materials used for apparatus construction (at 295 K). *Rev Sci Instrum*. 1989;60(8):2711-2714. doi:10.1063/1.1140646

77. Wapler MC, Leupold J, Dragonu I, von Elverfeld D, Zaitsev M, Wallrabe U. Magnetic properties of materials for MR engineering, micro-MR and beyond. *J Magn Reson San Diego Calif 1997*. 2014;242:233-242. doi:10.1016/j.jmr.2014.02.005

78. Young IR, Bydder GM. Phase imaging. *Magn Reson Imaging*. 1992;1:219-232.

79. Haase A. Snapshot FLASH MRI. Applications to T1, T2, and chemical-shift imaging. *Magn Reson Med*. 1990;13(1):77-89.

80. Müller KJ, Hertz HG. A Parameter as an Indicator for Water−Water Association in Solutions of Strong Electrolytes. *J Phys Chem*. 1996;100(4):1256-1265. doi:10.1021/jp951303w

81. Rohrer M, Bauer H, Mintorovitch J, Requardt M, Weinmann H-J. Comparison of magnetic properties of MRI contrast media solutions at different magnetic field strengths. *Invest Radiol*. 2005;40(11):715-724.

82. Tofts P s., Lloyd D, Clark C a., et al. Test liquids for quantitative MRI measurements of self-diffusion coefficient in vivo. *Magn Reson Med*. 2000;43(3):368-374. doi:10.1002/(SICI)1522-2594(200003)43:3<368::AID-MRM8>3.0.CO;2-B

83. Harris KR, Mills R, Back PJ, Webster DS. An improved NMR spin-echo apparatus for the measurement of self-diffusion coefficients: The diffusion of water in aqueous electrolyte solutions. *J Magn Reson 1969*. 1978;29(3):473-482. doi:10.1016/0022-2364(78)90005-7

84. McCall DW, Douglass DC. The Effect of Ions on the Self-Diffusion of Water. I. Concentration Dependence. *J Phys Chem*. 1965;69(6):2001-2011. doi:10.1021/j100890a034

85. Kim JS, Wu Z, Morrow AR, Yethiraj A, Yethiraj A. Self-Diffusion and Viscosity in Electrolyte Solutions. *J Phys Chem B*. 2012;116(39):12007-12013. doi:10.1021/jp306847t

86. Frahm J, Haase A, Matthaei D. Rapid NMR imaging of dynamic processes using the FLASH technique. *Magn Reson Med*. 1986;3(2):321-327.

87. Balaban RS, Ceckler TL. Magnetization transfer contrast in magnetic resonance imaging. *Magn Reson Q*. 1992;8(2):116-137.

88. Edzes HT, Samulski ET. Cross relaxation and spin diffusion in the proton NMR or hydrated collagen. *Nature*. 1977;265(5594):521-523.

89. Decarlo LT. On the meaning and use of kurtosis. *Psychol Methods*. 1997:292–307.

90. Burnham KP, Anderson DR. *Model Selection and Multimodel Inference: A Practical Information-Theoretic Approach*. Springer Science & Business Media; 2003.

91. Farrell JAD, Landman BA, Jones CK, et al. Effects of SNR on the Accuracy and Reproducibility of DTI-derived Fractional Anisotropy, Mean Diffusivity, and Principal Eigenvector Measurements at 1.5T. *J Magn Reson Imaging JMRI*. 2007;26(3):756-767. doi:10.1002/jmri.21053

92. Anderson AW. Theoretical analysis of the effects of noise on diffusion tensor imaging. *Magn Reson Med*. 2001;46(6):1174-1188.

93. Bastin ME, Armitage PA, Marshall I. A theoretical study of the effect of experimental noise on the measurement of anisotropy in diffusion imaging. *Magn Reson Imaging*. 1998;16(7):773-785.

94. Raja R, Sinha N, Saini J. Characterization of White and Gray Matters in healthy brain: An in-vivo Diffusion Kurtosis Imaging study. In: *2014 IEEE International Conference on Electronics, Computing and Communication Technologies (CONECCT)*. ; 2014:1-6. doi:10.1109/CONECCT.2014.6740324

95. Szczepankiewicz F, Lasič S, van Westen D, et al. Quantification of microscopic diffusion anisotropy disentangles effects of orientation dispersion from microstructure: Applications in healthy volunteers and in brain tumors. *NeuroImage*. 2015;104:241-252. doi:10.1016/j.neuroimage.2014.09.057

96. Hasan KM, Moeller FG, Narayana PA. DTI-based Segmentation and Quantification of Human Brain Lateral Ventricular CSF Volumetry and Mean Diffusivity: Validation, Age, Gender effects and Biophysical Implications. *Magn Reson Imaging*. 2014;32(5):405-412. doi:10.1016/j.mri.2014.01.014

97. Gao J-H, Liu H-L. Inflow effects on functional MRI. *NeuroImage*. 2012;62(2):1035-1039. doi:10.1016/j.neuroimage.2011.09.088

98. Bisdas S, Klose U. IVIM analysis of brain tumors: an investigation of the relaxation effects of CSF, blood, and tumor tissue on the estimated perfusion fraction. *Magma N Y N*. 2015;28(4):377-383. doi:10.1007/s10334-014-0474-z

99. Chiaradia M, Baranes L, Van Nhieu JT, et al. Intravoxel incoherent motion (IVIM) MR imaging of colorectal liver metastases: Are we only looking at tumor necrosis? *J Magn Reson Imaging*. 2014;39(2):317-325. doi:10.1002/jmri.24172

100. Akaike H. Information Theory and an Extension of the Maximum Likelihood Principle. In: *Selected Papers of Hirotugu Akaike*. Springer Series in Statistics. Springer, New York, NY; 1998:199-213. doi:10.1007/978-1-4612-1694-0_15

101. Mitra P, Sen P, Schwartz L, Le Doussal P. Diffusion propagator as a probe of the structure of porous media. *Phys Rev Lett*. 1992;68(24):3555-3558. doi:10.1103/PhysRevLett.68.3555

102. Synek V. Evaluation of the standard deviation from duplicate results. *Accreditation Qual Assur*. 2008;13(6):335-337. doi:10.1007/s00769-008-0390-x

103. Hooper J. Clinical Investigation and Statistics in Laboratory Medicine. *J R Soc Med*. 1997;90(12):706-707.

104. Barbieri S, Donati OF, Froehlich JM, Thoeny HC. Comparison of Intravoxel Incoherent Motion Parameters across MR Imagers and Field Strengths: Evaluation in Upper Abdominal Organs. *Radiology*. 2016;279(3):784-794. doi:10.1148/radiol.2015151244

105. Ivanov KP, Kalinina MK, Levkovich YI. Blood flow velocity in capillaries of brain and muscles and its physiological significance. *Microvasc Res*. 1981;22(2):143-155. doi:10.1016/0026-2862(81)90084-4

106. Stücker M, Huntermann C, Bechara FG, Hoffmann K, Altmeyer P. Capillary blood cell velocity in periulcerous regions of the lower leg measured by laser Doppler anemometry. *Skin Res Technol Off J Int Soc Bioeng Skin ISBS Int Soc Digit Imaging Skin ISDIS Int Soc Skin Imaging ISSI*. 2004;10(3):174-177. doi:10.1111/j.1600-0846.2004.00064.x

107. Keele CA, Neil E. *Samson Wright's Applied Physiology*. Oxford University Press; 1992.

108. Folkow B, Neil E. *Circulation*. Oxford University Press; 1971.

109. Cho GY, Moy L, Zhang JL, et al. Comparison of fitting methods and b-value sampling strategies for intravoxel incoherent motion in breast cancer. *Magn Reson Med*. 2015;74(4):1077-1085. doi:10.1002/mrm.25484

110. Turgeon ML. *Clinical Hematology: Theory and Procedures*. Lippincott Williams & Wilkins; 2005.

111. Lew HS, Fung YC. Plug Effect of Erythrocytes in Capillary Blood Vessels. *Biophys J*. 1970;10(1):80-99.

112. Prothero J, Burton AC. The Physics of Blood Flow in Capillaries. *Biophys J*. 1961;1(7):565-579.

113. Bagchi P. Mesoscale Simulation of Blood Flow in Small Vessels. *Biophys J*. 2007;92(6):1858-1877. doi:10.1529/biophysj.106.095042

114. Kiessling F, Jugold M, Woenne EC, Brix G. Non-invasive assessment of vessel morphology and function in tumors by magnetic resonance imaging. *Eur Radiol*. 2007;17(8):2136-2148. doi:10.1007/s00330-006-0566-x

115. Dvorak HF. How Tumors Make Bad Blood Vessels and Stroma. *Am J Pathol*. 2003;162(6):1747-1757.

116. Folberg R, Maniotis AJ. Vasculogenic mimicry. *APMIS Acta Pathol Microbiol Immunol Scand*. 2004;112(7-8):508-525. doi:10.1111/j.1600-0463.2004.apm11207-0810.x

117. Folberg R, Rummelt V, Parys-Van Ginderdeuren R, et al. The prognostic value of tumor blood vessel morphology in primary uveal melanoma. *Ophthalmology*. 1993;100(9):1389-1398.

118. Nagy JA, Chang S-H, Dvorak AM, Dvorak HF. Why are tumour blood vessels abnormal and why is it important to know? *Br J Cancer*. 2009;100(6):865-869. doi:10.1038/sj.bjc.6604929

119. Lustig M, Donoho D, Pauly JM. Sparse MRI: The application of compressed sensing for rapid MR imaging. *Magn Reson Med*. 2007;58(6):1182-1195. doi:10.1002/mrm.21391

120. Gaass T, Schneider MJ, Dietrich O, Ingrisch M, Dinkel J. Technical Note: Quantitative dynamic contrast-enhanced MRI of a 3-dimensional artificial capillary network. *Med Phys*. 2017;44(4):1462-1469. doi:10.1002/mp.12162

121. Ingrisch M, Sourbron S. Tracer-kinetic modeling of dynamic contrast-enhanced MRI and CT: a primer. *J Pharmacokinet Pharmacodyn*. 2013;40(3):281-300. doi:10.1007/s10928-013-9315-3

122. Detre JA, Zhang W, Roberts DA, et al. Tissue specific perfusion imaging using arterial spin labeling. *NMR Biomed*. 1994;7(1-2):75-82.

Danksagung

An dieser Stelle möchte ich mich bei all jenen bedanken, die zum Gelingen dieser Arbeit beigetragen und mich über die letzten Jahre hinweg unterstützt haben.

Ich bedanke mich bei Prof. Dr. med. Jens Ricke sowie bei dem ehemaligen Direktor Prof. Dr. med. Dr. h.c. Maximilian Reiser für die Möglichkeit an der Klinik und Poliklinik für Radiologie zu promovieren.
Ein besonderer Dank gilt meinem Betreuer Prof. Dr. rer. nat. Olaf Dietrich für seine fachliche Unterstützung, seine wissenschaftliche Kompetenz und sein immer offenes Ohr.
Ich danke Dr. rer. nat. Michael Ingrisch und Dr. rer. biol. hum. Michael Peller für wertvolle Diskussionen und deren Hilfe bei zahlreichen schwierigen Sachverhalten.
Meinen Arbeitsgruppenkollegen über die Jahre hinweg (Andi, Lukas, Linus, Konstantin, Thomas, David, Balthasar, Caro, Astrid, …) danke ich für viele kurzweilige Unterhaltungen und die lockere Atmosphäre.
Ich bedanke mich bei Prof. Dr. med. Julien Dinkel für die Möglichkeit meine fachlichen Kompetenzen im Bereich der radiologischen Bildgebung weiter zu vertiefen und möchte weiterhin auf medizinischer Seite Prof. Dr. med. Clemens Cyran und Prof. Dr. Med. Mike Notohamiprodjo für die interdisziplinäre Zusammenarbeit danken.

Abschließend bedanke ich mich herzlich bei meinen Eltern, meinen Geschwistern und meiner Freundin Yasmin für deren ausdauernden Rückhalt.

LMU LUDWIG-MAXIMILIANS-UNIVERSITÄT MÜNCHEN

Promotionsbüro
Medizinische Fakultät

MMRS MUNICH MEDICAL RESEARCH SCHOOL

Eidesstattliche Versicherung

Schneider, Moritz Jörg

Name, Vorname

Ich erkläre hiermit an Eides statt,

dass ich die vorliegende Dissertation mit dem Titel

Incoherent-Flow-Induced Signal Decay in Diffusion-Weighted Magnetic Resonance Imaging

selbständig verfasst, mich außer der angegebenen keiner weiteren Hilfsmittel bedient und alle Erkenntnisse, die aus dem Schrifttum ganz oder annähernd übernommen sind, als solche kenntlich gemacht und nach ihrer Herkunft unter Bezeichnung der Fundstelle einzeln nachgewiesen habe.

Ich erkläre des Weiteren, dass die hier vorgelegte Dissertation nicht in gleicher oder in ähnlicher Form bei einer anderen Stelle zur Erlangung eines akademischen Grades eingereicht wurde.

München, 28.06.2019

Ort, Datum

M. Schneider

Unterschrift Doktorandin bzw. Doktorand